Reduce wheel-rail impacts at insulated rail joints by optimizing sleeper spans

Amirhossein BarzegarSedigh

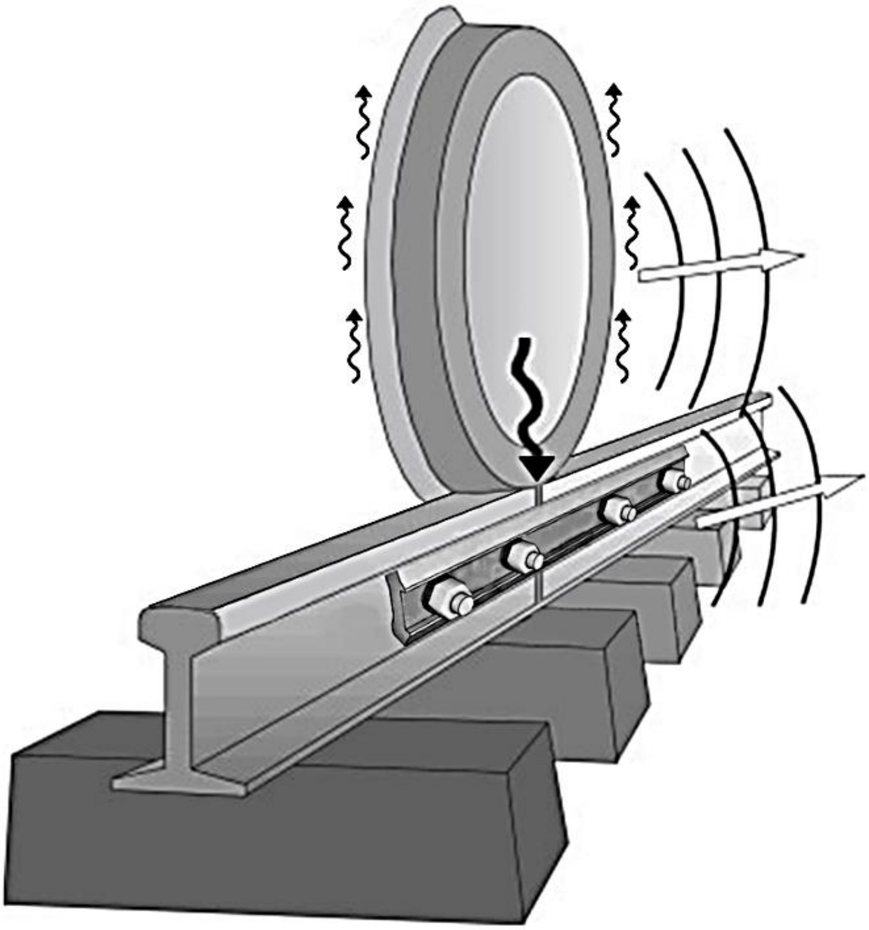

TU Delft

Reduce wheel-rail impacts at insulated rail joints by optimizing sleeper spans

by

Amirhossein BarzegarSedigh

in partial fulfilment of the requirements for the degree of

Master of Science
in Civil Engineering

at the Delft University of Technology,
to be defended publicly on 28.05.2020

Student number:	4744683	
Project duration:	October 1, 2019 – May 28, 2020	
Thesis committee:	Prof. Dr. Ir. R.P.B.J Dollevoet	Chair of the Committee
	Dr. Zhen Yang	Daily Supervisor
	Dr. Yuguang Yang	Supervisor

TU Delft

Preface

This M.Sc. thesis study is the pinnacle of my experience in the Master's degree at Delft University of Technology which has been a memorable journey. This involvement has been a prominent academic reward in helping me to learn coping with self-doubt and feelings of overwhelm as well as prevailing the challenges and pushing my potential.

I would like to express my sincere gratitude towards the chair of my thesis committee, Professor Rolf Dollevoet for his critical remarks and invaluable feedbacks during our discussion meetings. To say that his precious advices have been academically rewarding would be half the statement, since I noticed profound effects on my abilities in presenting my findings throughout the graduation project.

I would like to extend my gratitude to Dr. Yuguang Yang for his valuable contribution during my graduation project. His intellectual inputs and appreciative comments have helped me to discover more possibilities in amending my graduation project. My immense gratitude towards my daily supervisor, Dr. Zhen Yang, since this graduation project wouldn't be accomplished without his impressible contribution. I would like to thank him for introducing me to the application of explicit finite element analysis and inspiring my interest in this field as well as being available for consultation and providing constructive feedback which created an enriching learning experience in every step of the way.

Indeed, the family is the oldest of all our institution and stand at the very foundation of our lives. Thus, I would also like to thank my family for their unconditional love and continuous support throughout this period. My deep appreciation towards my parents who endured all difficulties to lay my path to success. Last, but not the least, I would like to thank my friends and peers that have made this experience worth the while.

Amirhossein BarzegarSedigh
Delft, May 2020

Abstract

In recent decades, rail transport has become a popular mean of transportation due to its efficiency and environmental friendliness technology which lead to increasing the axle loads, speed and recurrence of the trains. These enhanced service provisions resulted in new challenges to the sustainability of the railway systems. Insulated rail joint (IRJ) is one of the crucial structural components of the railway track with the function of serving the signaling control by securing the occupancy of the track with one and only train in each divided block. An IRJ includes the application of two joint bars being bolted with the purpose of connecting two adjoining rails. In addition to the insulation layers between the joint bars and the rail, the end post which is positioned between the end-to-end rails, assure the disruptions of current flow between two blocks. The emerge of discontinuity in the stiffness and geometry at IRJs influence the service life of this component due to the introduced high dynamic forces. Subsequently, the IRJ is considered as one of the weak spots of the railway tracks which requires the allocation of great concern in their maintenance. In order to attain understanding of the wheel-rail dynamic interaction at IRJs, various analytical, experimental and numerical studies have been conducted in the past few years. The application of the finite element method (FEM), as a flexible numerical tool, reveals distinct advantages for understanding the behavior of the track structure under the pass-by wheel.

This M.Sc. thesis utilizes an explicit finite element analysis to investigate the influence of the sleeper spacing and traffic speed on the impact force and vibration of the track. The FE model includes the detailed demonstration of the rail, joint bars and sleepers while simulated spring and damper elements are preferred to the rail pads and ballast to reduce the complexity of the model. Besides, the detailed illustration of the wheel and axle as well as the effects of the carbody and bogie are considered in the FE model. Based on the parametric studies conducted in this thesis, the impact force as well as the low (0–3kHz) and high (3-10kHz) -frequency vibrations are prominently influenced by the application of non-uniform sleeper spacing and various traffic speed. With considering the two factors; sleeper spacing and traffic speed, a typical statistical approach -Design of Experiment- is implemented to attain an optimized track model with the aim of reducing the impact force and the impact vibration of the track, and thus to reduce the maintenance necessity and noise generation as well as to increase the passenger comfort. The performance of the nominated optimized model has been observed under the application of two typical trains operated on the Dutch railway network. Finally, the conclusions are presented and recommendations for future research are proposed.

Contents

List of Figures

List of Tables

1

Introduction

This chapter provides a brief information about the insulated rail joints (IRJs), outlines the main objectives of the research, and explains the procedure adapted to answer the research questions.

1.1 General Information

Transportation is defined as any means of conveyance between two locations. Transportation enables trade between people which is known to be an essential tool for civilization development. There are various modes of transportation including air, land, rail and road as well as water. All modes of transportation consist of infrastructure, vehicles and procedures of operation. Besides, each mode includes benefits and drawbacks that are selected by users based on the comparison between cost, capability and availability.

1.1.1 Rail Transport

Nowadays, rail transport is considered as one of the quickest and most reliable modes of transportation. The railways consist of rolling stock, also known as train, which is directionally guided by the track through a desired route. The application of rail transport began in the 6th century BC in Greece. In the 16th century, wooden rails were implemented and operated by treadwheel pulled by human or animal power (*Funiculars, Funiculaires, Funicolare, DFB (Michel Azéma) reszug01*, n.d.). The modern type of this mode of transportation consists of steel rails installed on sleepers laid on ballast providing a smooth contact for the metal wheel which moves on it. Besides, other variations including slab track are implemented nowadays.

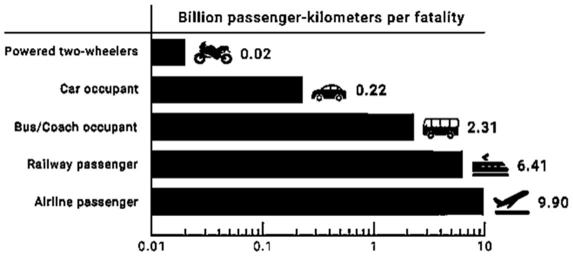

*Figure 1-1 Passenger Transport Safety (*Road-way vs. railway safety- Wikipedia*, n.d.)*

The rail transport has the ability of carrying a huge number of individuals as well as extensive cargoes at high speed. The advantages of the railway have made it one of the most popular modes of transportation. Besides, the investments in transportation using railways are interesting for authorities due to the low emission of CO_2 in the context of concerns related to global warming (*Rail transport - Wikipedia*, n.d.).

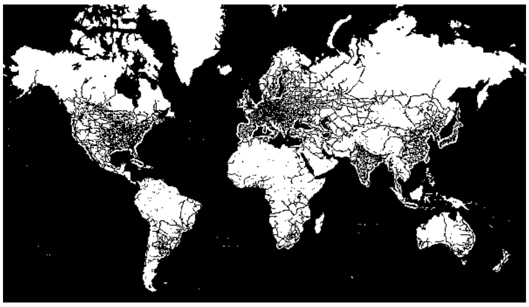

*Figure 1-2 World Railway Network (*World railway network - Wikipedia*, n.d.)*

Rail transport in the Netherlands has one of the densest railway networks in Europe. This network with 3223 route km is implemented to connect various towns and cities (*Rail transport in the Netherlands - Wikipedia*, n.d.). The infrastructure managing task of Dutch railways is assigned to the ProRail and the operators who won the concessions can operate their train on the track. The focus of the Dutch well-developed network is on the passenger rails which provides frequent trains that link nearly all major cities. Besides, freight trains share the tracks with passenger trains and mostly run in the east-west part of the country.

*Figure 1-3 Railway map in the Netherlands (*Railway Map The Netherlands - Wikipedia*, n.d.)*

1.1.2 Railway Track Structure

In general, the track consists of two rails anchored perpendicular to the beneath materials. Ballasted and non-ballasted tracks are two typical types of railroads which are widely implemented nowadays. Ballasted tracks are the traditional railroads which include the subgrade below a layer of crushed stones, called ballast. The ballast is laid beneath the concrete or wooden sleepers and the rails with certain lengths and distance from each other, called gauge distance, are anchored to the sleepers using the fastening system. The gaps between the sleepers are filled and tamped to reach the design level of the track. Non-ballasted or ballastless tracks consist of a concrete slab where rails are anchored using fastening materials.

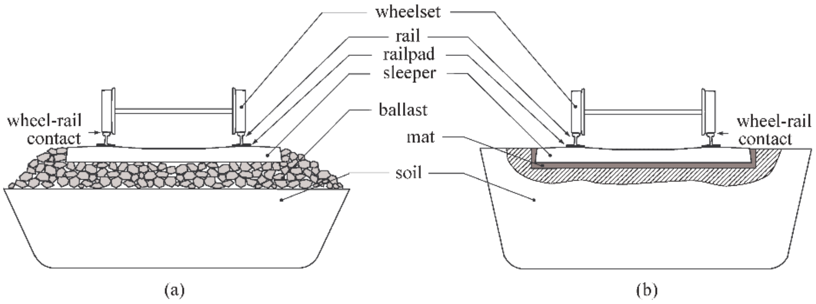

*Figure 1-4 Track components (a) Ballasted track; (b) Ballastless track (*Review of Trackside Monitoring Solutions*, n.d.)*

Although the non-ballast tracks are believed to be the advanced track technology, the decision on implementation of each method depends on various factors which include advantage and disadvantages of each type. These factors include investment cost, maintenance and life expectation as well as noise level and drainage performance.

1.2 Insulated Rail Joint (IRJ)

1.2.1 Function of IRJ

With regard to the manufacturing and transportation limitations, rails are produced in certain finite lengths. Therefore, various methods are used to join end-to-end rails to provide a continuous surface for the wheel to travel on it. These methods are described briefly as follow:

- Continuous Welded Rail: Nowadays, the modern railways implement this method where rails are welded together utilizing various welding methods and materials. CWR requires less maintenance and ensures a smooth ride which allows the trains to travel at a higher speed (*Rail transport - Wikipedia*, n.d.).
- Jointed Track: The method to join two rails in these tracks implement a pair of joint bars on either side which are bolted together with alternating orientation. There is a small gap which is deliberately considered to allow for variation of rail's length due to temperature fluctuation. There are three types of rail joints: standard, compromise and insulated joint

The Insulation rail joints are one of the most crucial parts of the signaling and train detection systems which are implemented to interrupt the current flow in the rails. Therefore, the track can be divided into blocks that are linked to the security systems. The circuit in each block is formed by electric current fed to the rails at one end and a relay is attached to the other side of the rails. As long as the rails are unoccupied the current can run through the relay which allows the track signal to indicate a clear section as shown in figure 1-6.

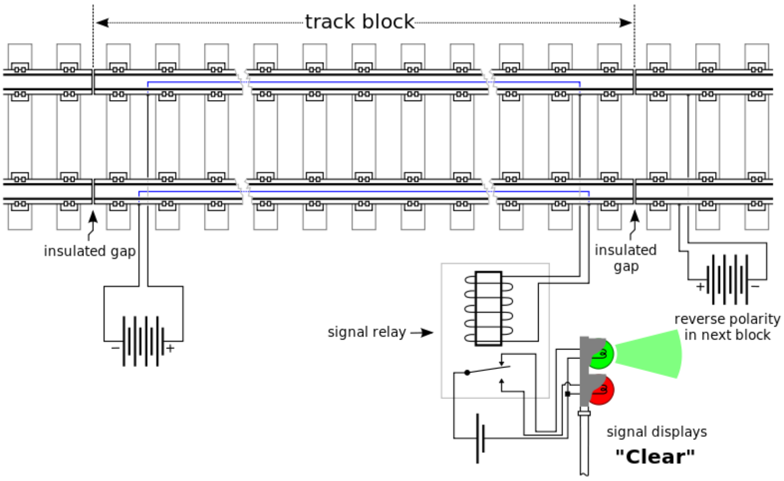

*Figure 1-5 Schematic drawing of track circuit for unoccupied block (*Track circuit - Wikiwand, *n.d.)*

When a train enters the block, the circuit is shortened and divert the current from the relay which causes a track signal to indicate an occupied section as shown in figure 1-7.

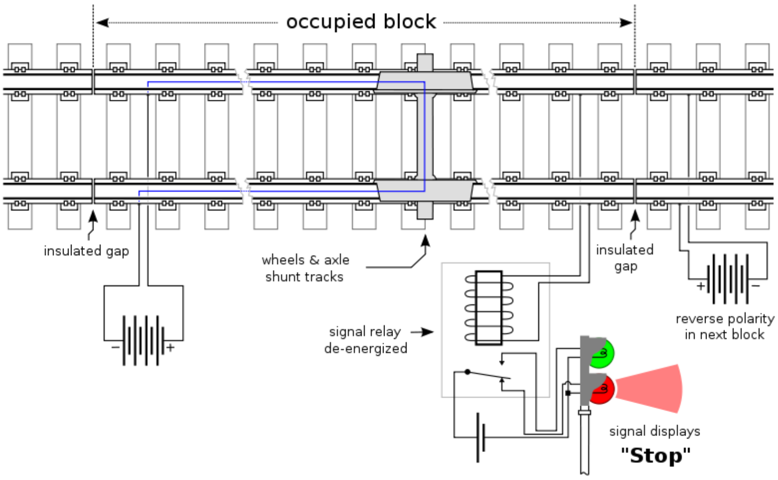

*Figure 1-6 Schematic drawing of track circuit for unoccupied block (*Track circuit - Wikiwand, *n.d.)*

1.2.2 Design of IRJ

Insulated rail joints (IRJ) employs various materials which each contributes to achieve the designation function of IRJ. These materials are shown in figure 1-7 (a) and (b). The isolation is fully achieved by the insulating layer which is placed between the joint bars and the rails using an adhesive material. Moreover, the end post is placed in the gap between two rails with two methods. In the first method, the end post is installed and the joint bars are bolted to the rails while in the other method, to ensure increasing the force and vibrational bearing capacity, the end post is placed by the high strength glue action between the components. (Elshukri, 2016)

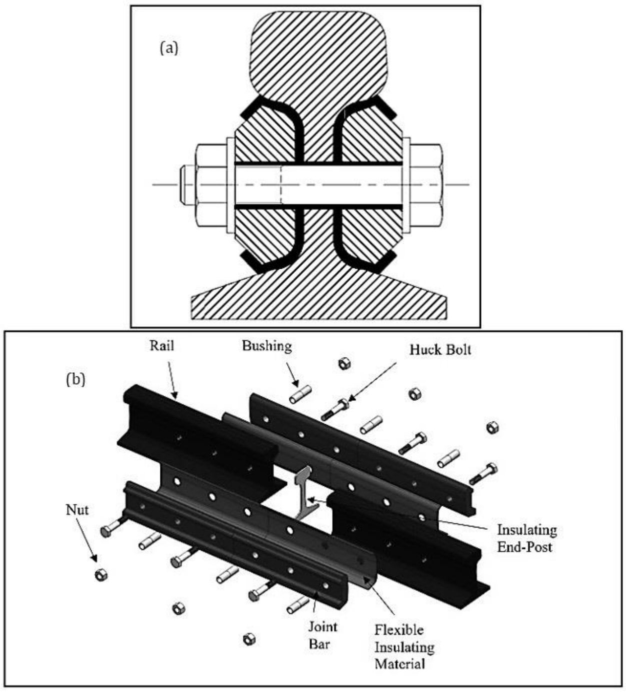

Figure 1-7 Typical insulated joint assembly (a) Cross section; (b) Exploded view (Elshukri, 2016)

Insulated rail joint (IRJ) consists of two joint bars, having insulation material in between, attached to the rails with the bolts. The end post is installed in the gap between the adjoining rails which ensure the insulating function of this type of joint. As shown in figure 1-8, there are two main design methods which depend on the support system; suspended (a) and supported IRJ (b). In the suspended system, no support exists directly beneath the joint while in the support system, a number of components such as sleepers may be implemented under the joint.

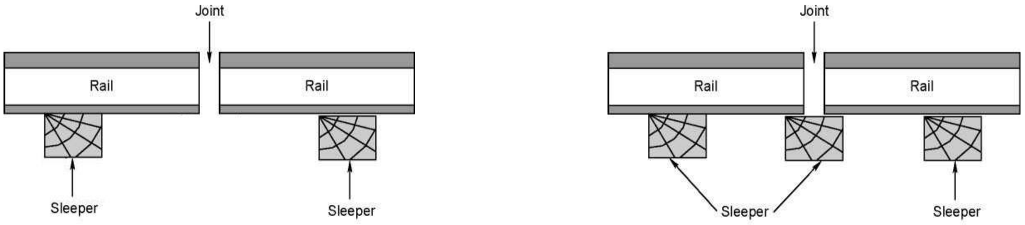

(a) (b)

*Figure 1-8 Support system at IRJ (a) Suspended IRJ; (b) Supported IRJ (*Types of Rail Joints*, n.d.)*

1.2.3 Failures of IRJ

In order to enhance the performance of the railway track, smooth uniform contact between the wheel and the rail is necessary. Therefore, existence of local irregularity in the running surface may cause stimulation of the wheel-rail interaction which results in the generation of the high impact and dynamic forces as well as increment of the dynamic vibrations. These phenomena increase the degradation rate of the track and fluttering of the carbody.

Rail joint is considered as one of the most common discontinuities in the track due to the presence of the gap between adjoining rails (Molodova et al., 2016). In a jointed track, the gap, which may be considered as a local irregularity, results in a high impact force on the forward rail. The difference between the geometry and stiffness due to the existence of the joint bar at the location of the joint has resulted in an additional incrementation of the dynamic forces and vibrations. Although this structural discontinuity is filled with the welded materials in the continuous welded rail (CWR), the variation of the stiffness between the rail as the parent material and the welded material results in various failures in this method as well. Hence, in either methods of rail linkage, the discussion about the acceleration of the rail degradation is the concern.

(a) (b)

Figure 1-9 Failure at the rail joint (a) CWR; (b) Jointed Track

IRJs are served as one of the crucial components to achieve a safe signaling control. Therefore, the failure of IRJ is considered as one of the most serious safety cases which attentions are paid to the issue of their maintenance (Elshukri, 2016). Since IRJs are one types of the jointed tracks, these structures are also regarded as one of the weak sections in the railway track. The service life of IRJs is believed to be as low as half of the other components of the track approximately. Consequently, IRJs are believed to be failed after around 200 million gross tons which significantly increases the maintenance cost of the track (Sheikh et al., 2014).

In order to improve the performance of the track at IRJs, sufficient information about the failure modes need to be collected accordingly. There are two main types of failure modes that correspond to the IRJs; electrical and mechanical failure. The electrical failure occurs when the electrical isolation between the two connected rails is disturbed by various factors. The mechanical failure is considered as the most prevalent cause of failure at IRJs which influences the rails, joint bars and the bolts. As it can be seen in figure 1-10 and 1-11, cracking and breakage of the rails and joint bars are caused due to the excessive load and high impact forces at the IRJs. The high force applied on rail web results in fracture of the bolts consequently. Moreover, debonding of the insulating layer between the joint bars and the rails is considered as the result of high applied loads. The same cause can consequence the debonding and crushing of the end post.

Figure 1-10 Breakage of the Joint bar

Figure 1-11 Breakage of the rail

As shown in figure 1-12 and 1-13, chipping out as well as metal flow of the railhead can occur at these locations. It is also believed that the debonding of the insulating materials and metal flow of the railhead can be the origins of electrical failure.

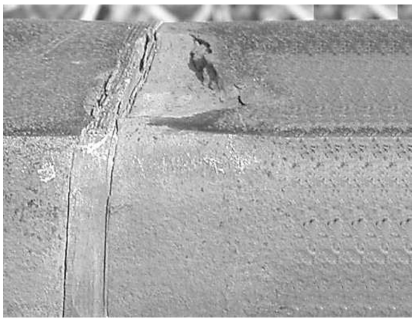

Figure 1-12 Chipping out of the rail

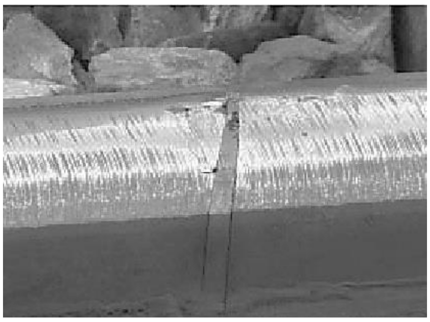

Figure 1-13 Metal flow of the rail

The distribution of the failure modes in the location of the insulating rail joints can be seen in figure 1-14. The involvement of various mechanisms in malfunctioning of the IRJs has made it to be regarded as a high-risk component which requires an expensive maintenance program with high standards. Rail infrastructure managers are obliged to install rail joints due to the early failure or the risk of disturbing the signaling control which in some cases can result in catastrophic costs.

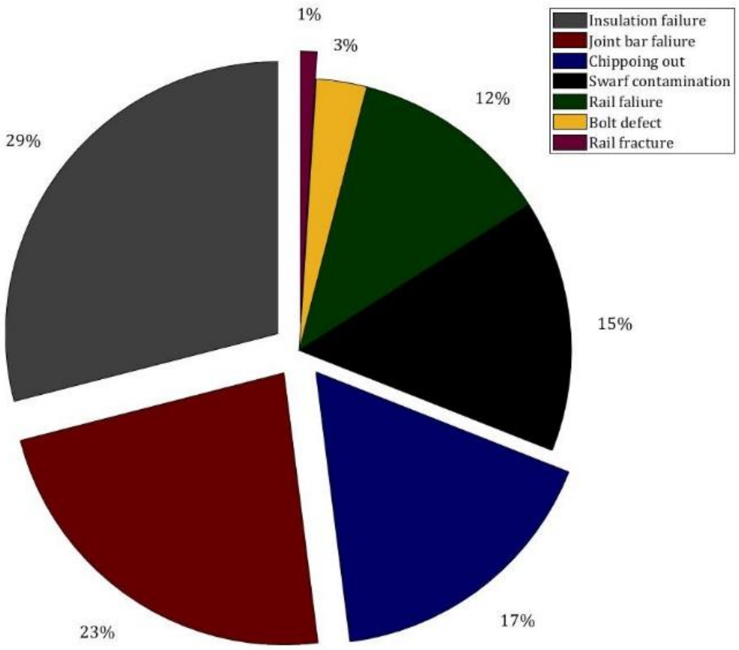

Figure 1-14 Distribution of failure modes

There are some accident cases which are recorded as the consequences of failure of the joints. For instance, on 5 November 1967, the Hither Green rail crash is recorded as the failure of the joint bars and the bolts which resulted in 49 fatalities and 78 injuries (*Hither Green rail crash - Wikipedia*, n.d.). Another case was seen on 25 January 2018 that a derailment occurred as a result of malfunctioning of the IRJ. This accident caused the death of 3 women and the injuries of more than 100 people. (*Pioltello train derailment - Wikipedia*, n.d.).

1.3 Research Objective and Novelty

This M.Sc. thesis aims to utilize an explicit finite element analysis to reduce the impact force as well as the vibration of the track. Moreover, this research provides a parametric study to quantify the effects of the sleeper spacing and traffic speed on the impact force as well as the low (0-3kHz) and high (3-10kHz) -frequency vibrations of the track under different load conditions. Accordingly, a typical statistical approach, Design of Experiment (DOE) is implemented to propose an optimized track model for both intercity and sprinter trains used in the Dutch railway network.

The specific optimization technique, DOE used in this M.Sc. thesis is the main novelty of this research. This technique facilitates the optimization of the system performance by comprehensively considering both the sleeper spacing and traffic speed under different load conditions. Subsequently, this research evaluates and compares the performance of the optimized track model for both intercity and sprinter trains that are operated in the Dutch railway network. It should be mentioned that this has barely been done in previous studies.

Moreover, the explicit finite element analysis that is employed in this research provides the opportunity to reliably model the effects of sleeper arrangements, traffic speed and the load condition on the vibration of the track and the impact force. The explicit FE modeling also enables the correlation analysis of the wheel-rail impact force (input) and the consequent wheel/rail impact vibration (output).

The following research questions indicate some important concerns of this research.

- **Does the variation of sleeper spacing have a noticeable impact on the wheel pass-by vibration of track?**

Prior researches have shown that the magnitude of some specific track resonances (free vibration) at the IRJ section can be reduced by altering the sleeper spacing (Papaioannou, 2018). With respect to the complex train-track interaction this statement is further investigated to evaluate whether the wheel pass-by vibration of track (forced vibration) can also be reduced by optimizing the sleeper spacing.

- **How do the sleeper spacing and traffic speed influence the impact force and track vibration under different load conditions?**

In order to assess the effects of sleeper spacing and traffic speed on the track vibration and impact force under different load conditions, parameter variation is initially conducted with a validated explicit finite element wheel-rail dynamic interaction model developed in ANSYS/LS-DYNA. The simulated results of impact force and track vibration are compared in the time domain and frequency domain.

In order to help passengers to experience minor movements as well as reducing the track maintenance, track vibration and impact force is desired to be decreased accordingly. The statistical approach used in this research provides the opportunity to determine the most optimized combination of sleeper spacing and traffic speed for intercity and sprinter trains operated in the Dutch railway network.

1.4 Overall Approach of the Research

The 3D finite element model implemented in this research is originally created by (Yang et al., 2018) by proposing series of codes using the ANSYS APDL 15. In order to investigate the effects of sleeper spacing on the track vibration, the new models were built in ANSYS APDL 18. However, with regard to the different meshing pattern utilized in the version of ANSYS 18, the codes generating the original model were required to be modified and the new model is essentially validated against the original model by comparing the power spectrum density of the impact vibration and wheel-rail contact force.

Based on the validated explicit FE model, the sleeper spacing and traffic speed were individually altered to assess the effects of these parameters on the vibration of the track and impact force. A specific statistical technique, DOE, was then employed to determine the optimized combination of sleeper spacing and traffic speed for different load conditions that may improve the train-track interaction in terms of track vibration and impact force.

1.5 Outline of this Research

This thesis presents an extensive overview of the prior researches on the analytical, experimental and numerical studies on the IRJ in Chapter 2. In Chapter 3, the 3D FE model is described in detail. In Chapter 4 a parametric study is conducted to quantify the effects of sleeper spacing on impact force and track vibration. In Chapter 5, a parametric study is carried out which discusses the effects of train speed on the vibration of the track as well as the impact force. In chapter 6, a DOE algorithm is implemented to assess an optimized combination of sleeper spacing and traffic speed. In chapter 7, the selected optimized models that are obtained from chapter 6 are utilized to analyse the effects of the load of trains on these models. Accordingly, the loads of the two trains passing by with different loads: intercity and sprinter, used in the Dutch railway network are simulated. Finally, Chapter 8 presents the conclusion and the proposed recommendation in this research.

2

Literature Studies

In this chapter, an extensive review regarding the previous studies on the insulated rail joint (IRJ) is presented. The literature study mainly focuses on the numerical studies, while some findings from experimental and analytical studies are also described.

2.1 Dynamic Railway Track Properties

The dynamic railway track properties are extensively studied by (de man, 2002). It is stated that the track structures contain a series of specific structural vibration modes which cover both vertical and lateral vibration modes. These modes can be divided to three ranges including low, mid and high frequency vibrations. An overview of these frequency ranges with the information about the human perception, structural damage and its origin can be seen in the table 2-1.

Table 2-1 Brief overview of division in frequency ranges (de man, 2002)

frequency range	low	mid	high
thresholds	0-40 Hz	40-400 Hz	400-1500 Hz
part of track	substructure	superstructure excluding rail	rail
human perception and discomfort			
local resident	vibrations and contact noise (buildings)	radiated sound/noise	radiated sound/noise
passenger	vibrations and contact noise (vehicle)	radiated sound/noise	radiated sound/noise
structural damage			
track	damage of substructure and engineering structure	damage of superstructure	damage of rails
vehicle	damage of substructure and engineering structure	damage of wheels	damage of wheels
origin of input load			
wheel	minimum	surface geometry: (short) wavelength	surface geometry and roughness
rail and track	geometry: (long) wavelength	as above, but not necessarily repetitive	as above, but not necessarily repetitive

The low frequency range (0-40 Hz) is determined by the substructure while the middle frequency range (40-400 Hz) is influenced by the sleepers, ballast and baseplate (de man, 2002). The similar statement was given by (Thompson, 2009) that investigated the track vibration by considering the influence of each component of the track. It was claimed that the support structure below the rails introduce a behavior that can be understood in vibration modes at low frequencies. The high frequency range (400-1500 Hz) is affected by the rest of the superstructure components such as fastening, rail pad, baseplate and rail properties (de man, 2002).

In the middle frequency range, the full track resonance (f_t) and sleeper anti-resonance (f_s) represent the two dominant modes which are observed in the frequencies of 40 – 140 Hz and 100

– 400 Hz respectively. The f_t represents the vibration and bending of the whole structure while in f_s the sleepers vibrate vertically and rail is considered as a stationary component.

In the high frequency range, the rail resonance (f_r), first and second order pinned-pinned resonance (f_{pp}) and (f_{pp2}) are the three dominant modes (de man, 2002). The f_r which depends on the rail pad properties occurs at 250 – 1500 Hz (Thompson, 2009). Although the first and second order pinned-pinned resonance cannot be detected in slab tracks, these frequencies can be developed in the ballasted track with discrete supports. The f_{pp} and f_{pp2} occurs in 400 – 1200 Hz and 1400 – 3000 Hz respectively. An overview of the most seen modes of the track can be seen in figure 2-1.

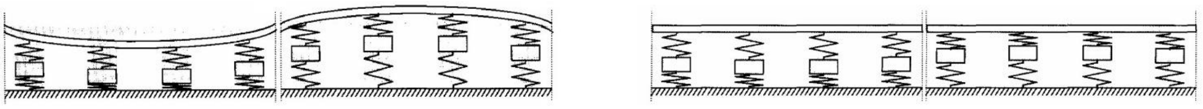

Full track resonance (f_t)

Sleeper anti-resonance (f_s)

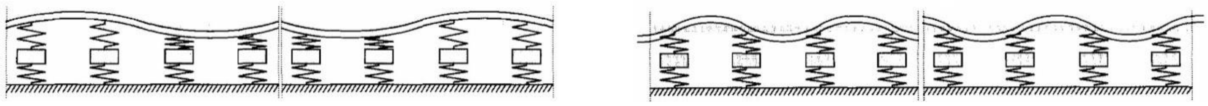

Rail resonance (f_r)

1st order pinned-pinned resonance (f_{pp})

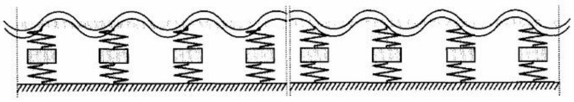

2nd order pinned-pinned resonance (f_{pp2})

Figure 2-1 Overview of the important vibration modes of the track (de man, 2002)

(Thompson, 2009) stated that the dynamic behavior of the track can be understood from frequency response function (FRF). It is claimed that the dynamic behavior of the track for majority at the resonances can be understood by comparing the FRF results of sensors that are placed on above the sleeper except the pinned-pinned resonance.

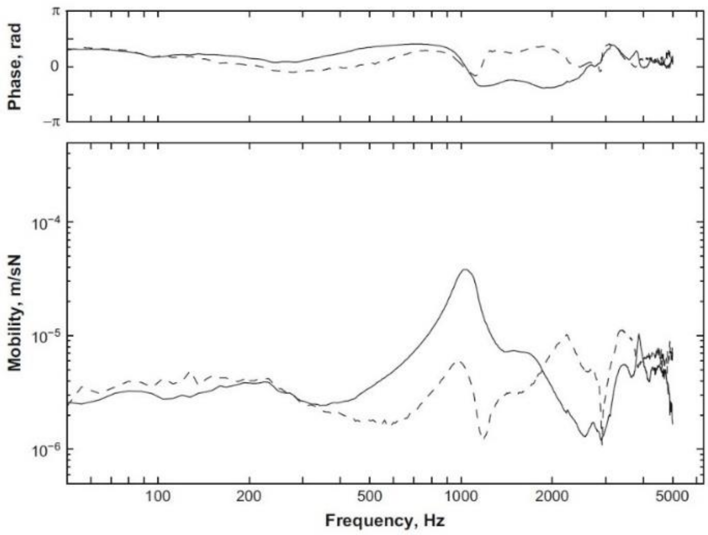

Figure 2-2 Vertical mobility for the track. -, measured at mid-span, - - -, measured above a sleeper (Thompason, 2009)

In order to investigate the frequency where above-mentioned resonances occur more closely, (Oregui et al., 2015) performed the hammer test and implemented the Fast Fourier Transform algorithm to compare the measured receptance functions at different locations. Figure 2-3 shows the peak where pinned-pinned resonance is likely to happen. This resonance is believed to be occurred in 1040 Hz approximately.

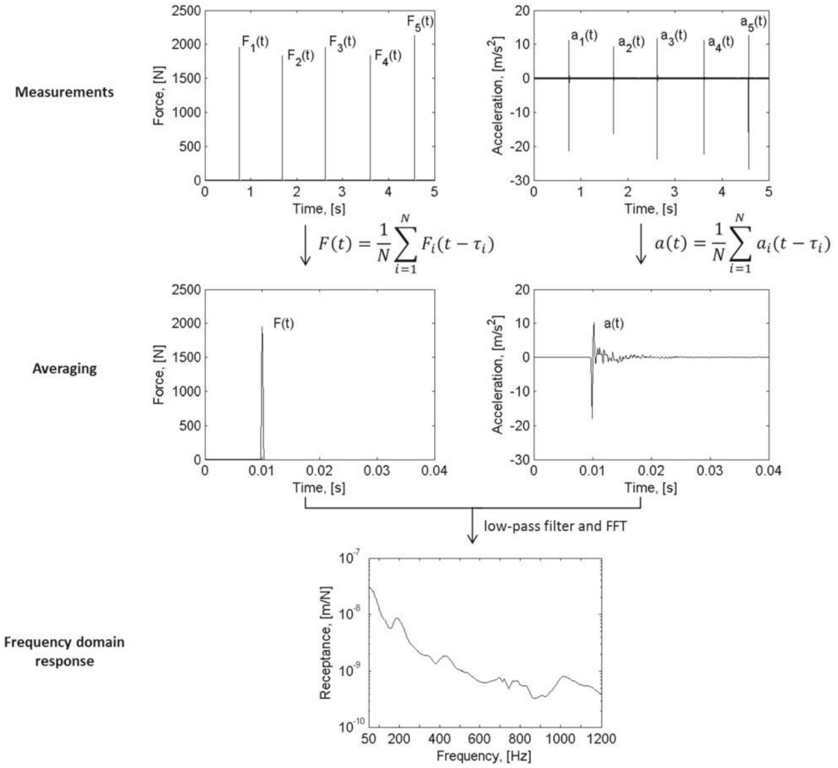

Figure 2-3 Acquiring receptance of the track using FFT algorithm (Oregui et al., 2015)

(Yang et al., 2018) concluded that the sleeper anti-resonance (f_s) occurs around 300 Hz while 1st order pinned-pinned resonance (f_{pp}) was seen at 1 kHz around the insulated rail joints. (Papaioannou, 2018) used the direct frequency response function and obtained similar conclusion. This research represented the frequency of around 450 Hz for rail resonance (f_r). The figure 2-4 illustrates the peaks where rail resonance and pinned-pinned resonance are shown.

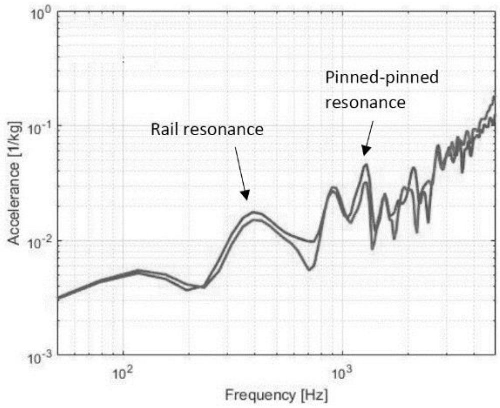

Figure 2-4 Overview of f_r and f_{pp} (Papaioannou, 2018)

2.2 Wheel-Rail Dynamic Interaction at IRJ

The interaction between the wheel and rail have been an important issue which various researches have been conducted in this field. Since there is a complex interaction between the wheel and rail, various methods have been implemented to obtain the best results in terms of obtaining a close agreement with the real situation in the track. These efforts include the analytical, experimental as well as the numerical studies that are increasingly considered since they are believed to be more appropriate in dealing with complex interaction between wheel and rail. The boundary element method and finite element method are two main tools that are used in numerical studies. The computer programs such as FASTSIM and CONTACT implement the BEM solutions which has the ability of analyzing the local interactions. The FEM can perform the global analyses which is based on the general continuum mechanics. The finite element models are considered as flexible tools for modelling arbitrary contact geometries with linear and nonlinear material properties.

In the following parts of this chapter, various analytical, experimental and numerical studies on the IRJ will be presented. These studies are ultimately investigated on the interaction between the wheel and rail by considering the presence of insulated rail joint. The presence of the IRJs showed a significant influence on the dynamic interaction between wheel and rail. This includes the impact force, dynamic contact force and vibration of the track. These researches had performed various parameter studies that showed the importance of track components on improving the behavior of the track.

2.3 Analytical Studies on the IRJ

2.3.1 Analytical IRJ Models

The analytical studies contain various validated mathematic procedures which allow the researchers to predict the behavior of the structure. In order to analyze the behavior of the track in the presence of the IRJ, there were several researches established using analytical studies in line with the experimental studies which enable them to validate their model.

According to (Kerr & Cox, 1999), a static analytical study was performed to calculate the deflection of a bonded IRJ under vertical loads by implementing the three beams connected by vertical Winkler-type springs. This analytical model was used to examine the problem of IRJ which was believed to be a weak spot of the track.

The dynamic behavior of the track near rail joints was measured by (Suzuki et al., n.d.). This study was based on the comparison between the experimental and analytical model of the track dynamic model which can be seen in figure 2-5. The results showed a good agreement on dynamic behavior of wheel loads and rail seat forces. It is believed that the impact and dynamic wheel load at high frequencies are excited by the gap at IRJ.

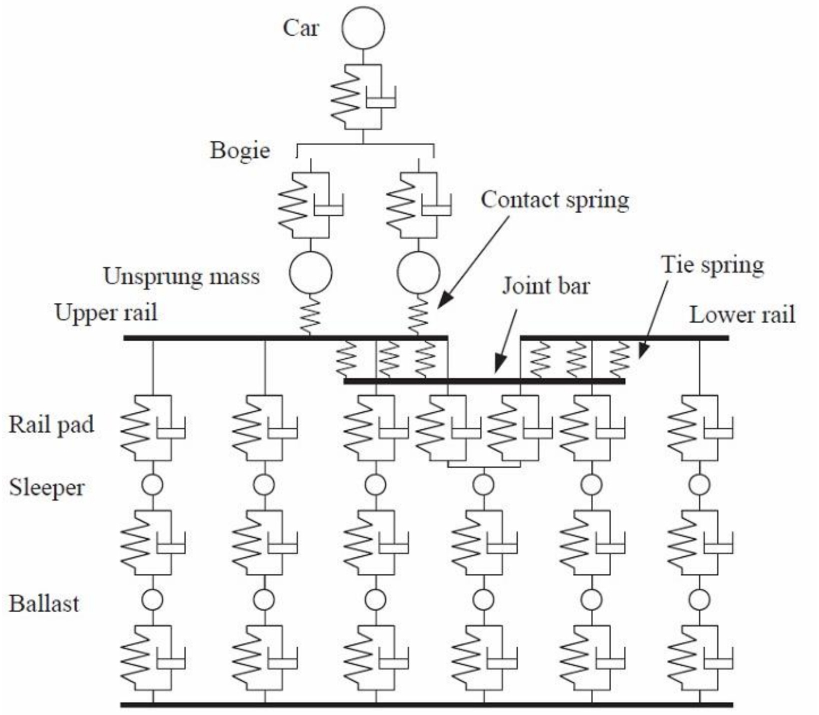

Figure 2-5 Track dynamic analytical model at insulated rail joint

In order to calculate the wheel-IRJ interaction with a displacement excitation model, (Wu & Thompson, 2003) performed an analytical study which a pin between two semi-infinite Timoshenko beams was implemented to represent the joint. Later, a validated revised model with substituting a complex spring instead of the pin was proposed by (Kitagawa T. et al., 2015).

2.3.2 Conclusions Drawn with the Analytical Studies

(Kerr & Cox, 1999) compare the deflection between insulated rail joints and continuous welded rail and deduced that due to the lower bending stiffness of the joint bars, the deflection at IRJ is generally larger than continues welded rail.

According to (Suzuki et al., n.d.), dynamic wheel load is increased by ballast and subgrade settlement as well as deformation and wearing of longitudinal edge of the rail. It was also stated that the difference between the sleepers' settlement can significantly influence the dynamic impact load.

Moreover, it is deduced that the dynamic wheel load increases towards the vicinity of the IRJ, decrease at vicinity and once more increase after passing the joint. Besides, it is believed that application of softer rail pad contributes to reducing the joint dips effect (Suzuki et al., n.d.). It was also illustrated that the presence of longitudinal irregularity at joint dips has higher effects on the wheel dynamic load than the joint gap.

2.4 Experimental Studies on the IRJ

The two test methods including the single lap joint and double cantilever beam were implemented to determine the optimum performance of the combination of adhesive, insulator and surface treatment by (Nicoli et al., n.d.). It is suggested that a surface preparation needs to be performed due to high level of oxidation under the bond line.

An experimental test was performed by (Boyd et al., 2012), to measure the progressive ratcheting by measuring the high stress which is believed to cause the metal flow. The digital image correlation technique was implemented to measure the contour, deformation, vibration and strain. It is claimed that ratchetting of railhead near to the end post is the cause of increasing the need of maintenance at IRJs.

(Elshukri, 2016) performed an extensive experimental investigation to study the properties of various types of end post materials and improve the performance of this component of insulated rail joints. An overview of test machine used in this research can be seen in figure 2-6.

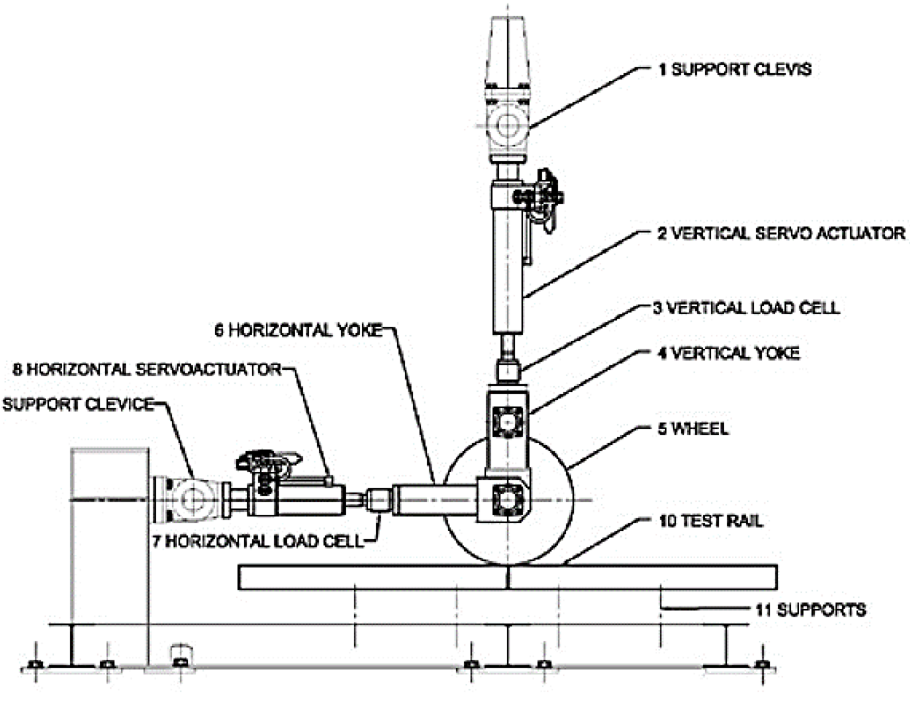

Figure 2-6 Test rig overview (Elshukri, 2016)

(Elshukri, 2016) claimed that the end post material and its thickness are related to IRJ failure and dynamic actions. Low thickness of end post was believed to highly influence the metal flow and high thickness can increase the impact damage to the rail. It was concluded that the epoxy glass material is the optimum material for the end post at IRJ. Similarly, (Mandal, 2016) proposed the fiberglass epoxy end post to have better performance with regard to a lower impact force and the material degradation subsequently.

2.5 Numerical Studies on the IRJ

2.5.1 Numerical IRJ Models

A numerical analysis was performed by (Kabo et al., 2006) to study high frequency dynamic interaction combined with deterioration in forms of rolling contact fatigue and plastic deformation. The FE model used in this research can be seen in figure 2-7. (Gallou et al., 2018) presented a static finite element model to introduce a comparison between the plain rail and IRJ with various support stiffness.

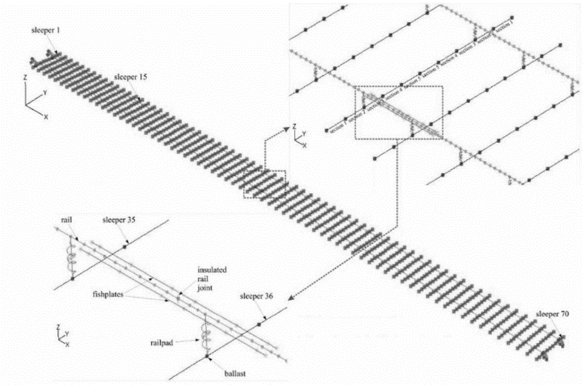

Figure 2-7 Three-dimensional beam FE model of a track (Kabo et al., 2006)

A 2D static numerical model was established by (Zong, 2013) and concluded that the edge effect may result in a larger deflection and higher stress at the rail end. (Pang & Dhanasekar, n.d.) proposed a 3D dynamic finite element model where contact impact near to the IRJ was studied.

(Koro et al., 2004) developed a dynamic finite element model that employed springs to connect the joint bars to the rails that where supported by elastic springs themselves. The edge effect of rail joint was analyzed and the effect of the gap size and train speed on impact force was considered.

(Zakeri & Xia, 2008) implemented a program software, DATI, as a tool to simulate the vertical dynamic interactions between vehicle and track. The interaction between train and track is considered as a dynamic system where rail is modeled using a FE model discretely supported by sleepers that are modeled by Timoshenko beam. The ballast and sleepers are connected by spring and dashpots. The displacement, velocity, acceleration of every component as well as dynamic force between wheel and rail is obtained for further comparison between the various components that are involved in the variation of dynamic behavior of track.

The contact stress near the insulated rail joint was assessed by (Chen & Kuang, n.d.) through a static 3D finite element method. The numerical results showed that the IRJ influence the wheel-rail contact stress distribution which results in incapability of the traditional Hertzian theory to predict the stress contours at this location.

As shown in figure 2-8, a detailed 3D finite element analysis was performed by (Mandal, 2016) to examine the plastic deformation as well as the damage to the end post and railhead due to the wheel load by determining the stress distribution. Three different end post materials with a consistent thickness were implemented in this research. (Kumar Mandal & Peach, 2010) studied various design and failure modes and used a 3D finite element model to find the stress on the various sizes of joint bars.

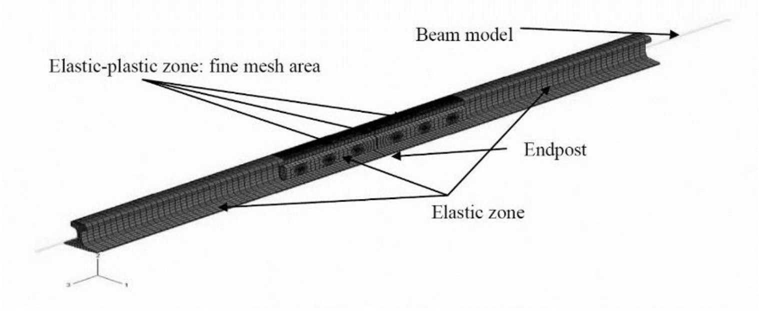

Figure 2-8 Six-bolt IRJ model with beam elements at rail ends (Mandal, 2016)

(Davis et al., n.d.), developed a finite element model using six bolts insulated rail joint and established an assessment of the stress and strain at the presence of IRJ. A significant effort was placed in reducing the stress concentration and optimizing the structural stiffness at IRJ.

To determine the dynamic effects of railway track, a study was performed by (Feng, 2011) using ABAQUS as one of the most popular FEM software. Through this study, track vibration modes were identified and effects of parameters were investigated using the FE model.

The reason for severe damage can be singularity wheel-rail contact pressure. Therefore, the essence of a new shape of railhead is developed to eliminate this singularity (Zong, 2013). Accordingly, three method of search of accuracy and efficiency was coupled with parametric FEM to find the optimal design of the rail shape which is called Stress Minimized Railhead (SMRH). Furthermore, another design method called Embedded IRJ (EIRJ), was implemented to achieve required stiffness. This design used the rails which were embedded into a concrete. These two models are presented in figure 2-5.

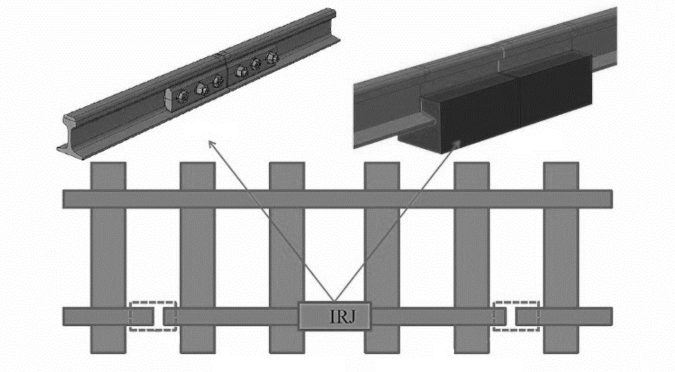

Figure 2-9 Improved design of IRJ (Zong, 2013)

In order to determine the impact dynamic force, a dynamic elasto-plastic finite element analysis was established by (Wen et al., 2005) where implicit to explicit technique was implemented. The same analysis was performed by (Cai et al., 2007) while a wheel was used to pass over the joint with different height at the ends of adjoining rails. Therefore, this allowed the numerical results to represent the effect of height difference as well as train speed and axle load on the contact force and stress on the rails.

(Yang et al., 2018) performed a numerical and experimental study to investigate the wheel-rail impact vibration as well as the noise generated at an IRJ. This study implemented a finite element model which the stiffness and damping corresponding to the fastening system and ballast were calibrated against the field measurement through the comparison of resonance frequencies in frequency response functions. The validation of dynamic behavior was conducted by comparing the decay rate of the track which is known as the rate of reduction of rail vibration amplitude along the track. The FE model used 8 node solid elements for the wheel, rail and sleepers and non-uniform meshing was employed to achieve a more accurate result.

The numerical and experimental studies were carried out by (Papaioannou, 2018) to determine the dynamic behavior of the track in the vicinity of the Insulated Rail Joint. The experimental results that were produced by the hammer test were used to validate and calibrate the finite element model. Moreover, the sensitivity analysis was performed to identify the parameters that affect the behavior of the joint.

According to (Papaioannou, 2018), a non-uniform formation of sleeper spacing was implemented to reduced possible track resonances. Furthermore, among the various parameters, stiffness and damping of the fastening system and ballast as well as sleeper spacing were chosen as the most important parameters that can be used to optimize the behavior of the track at the IRJ.

2.5.2 Conclusions drawn with the Numerical Studies

2.5.2.1 Joint Bar and Insulation Layer Related Conclusions

Based on the research performed by (Sheikh et al., 2014), the frequent cause of insulation failure is adhesive debonding. Accordingly, (Chen & Kuang, n.d.) believed that the deflection may result in higher chance of delamination of insulated layer.

The problems encountering with the failure of IRJ is believed to be sensitive to the varied bending stiffness of the components as well as the presence of the gap even though it is filled with the end post (Kumar Mandal & Peach, 2010). The bending stiffness highly depends on the bending stiffness of the joint bars and tightness of the bolts.

(Kumar Mandal & Peach, 2010) stated that the joint bars have lower vertical bending stiffness in comparison with the rail. This introduce a weak link between the two adjoining rails that results in larger deflection of rail, larger wheel force and higher wheel impact force accordingly. Even though the joint bar can be an aid to provide similar shear capacity to the parent rail at jointed tracks, its resistance decreases to bending the existence of the bolts (Gallou et al., 2018).

Similarly, (Molodova et al., 2016) also believed that the IRJ has higher impact dynamic forces due to low bending stiffness of joint bars as well as the low modulus of elasticity of end post. This impact force is believed to result in high stress concentration, cavity-like damage on railhead, high maximum shear stress and growing crack. It is concluded by (Kabo et al., 2006) that a high stress concentration and plastic deformation may be developed due to low load-carrying capacity of insulating material at insulated rail joint.

There are various solutions proposed by researchers to tackle with the issue regarding the joint bar and insulated layer. (Gallou et al., 2018) believed that the low stiffness of joint bars can be improved by the support condition. It is concluded that maximum vertical displacement decreases and shear stress increases with increase of joint bar width. The increase of the joint bars can improve the bending stiffness of the IRJ while reduction of stress is achievable by increasing the joint bar thickness.

Furthermore, among Epoxy fiberglass, Poly Tetra Flouroethylene (PTFE) and Nylon 66 as the most popular material for end post, it was stated by (Chen & Kuang, n.d.) that using Nylon-66 or PTFE which contribute to a lower Young's modulus of IRJ may result in a high maximum shear stress that may cause a partial loss of bond. This conclusion is in line with (Mandal, 2016) that proposed the fiberglass epoxy end post to have better performance with regard to a lower impact force and the material degradation subsequently.

2.5.2.2 Fastening, Rail Pad and Ballast Related Conclusions

(Sadri & Steenbergen, 2018) showed that the ballast stiffness is one of the most significant parameters that influences the dissipation of energy which can be a tool to identify the degradation rail of the track components.

According to (Feng, 2011), softer rail pad makes larger deflection of rail which results in load distribution on more sleepers. On the other hand, the soft rail pads suppress the transmission of high frequencies to sleeper and ballast that can be an aid to isolate these range of frequencies.

It was also claimed that spring and dashpot representing the track components have highest effects on vibration in vertical direction. Moreover, stiffness of rail pad shifts resonance frequency and damping influence the amplitude of the resonances.

(Zakeri & Xia, 2008) concluded that decreasing the rail pad stiffness results in reduction of ballast, sleeper displacement and wheel-rail interactive force but increase the displacement, acceleration and velocity of the rail.

It should be noted that fatigue damages to fastening and crushing of rail pad appear due to high frequency loads (Wang et al., 2014). The stiffness and damping of the ballast determine the full track resonance while the sleepers and rail pad properties influence the sleeper anti-resonance (Grassie et al., 1982).

Moreover, it is said that the vertical damping of ballast affects the frequency range of 50 to 150 Hz. Besides, the frequency range of 50 to 300 Hz experience changes with the vertical stiffness of ballast. Although the damping and stiffness of the rail pad has small influence in pinned-pinned resonance, it is believed that it significantly affects the rail resonance (Feng, 2011).

2.5.2.3 Sleeper and Support Related Conclusions

The features like sleeper spacing, rail pad and ballast stiffness and damping influence the dynamic response of the track. (Zakeri & Xia, 2008) concluded that the wheel-rail contact force is mainly influenced by the sleeper spacing, unsprung mass and rail stiffness.

(Boyd et al., 2012) claimed that the unsupported railhead edge at adjoining rails accumulates high plastic strain. (Davis et al., n.d.) concluded that firm support may contribute to a lower stress level of different components of IRJ while differential settlement results in higher yield tendency of the joint bars. Furthermore, (Gallou et al., 2018) deduced that reduction of deflection does not have a linear correlation with the support stiffness.

Among the various parameters, the sleeper spacing is accounted to have a considerable effect on the degradation of the track (Sadri & Steenbergen, 2018). The sleeper spacing of 500mm, 600mm and 700mm was implemented to compare the track response and wheel-rail interactive force. It is concluded that increasing the sleeper spacing results in increasing the degradation rate.

As pinned-pinned resonance plays n significant role in noise and vibration radiation of the rails, a substantial focus can be placed to achieve a reduced amplitude at this resonance as well as rail resonance. At resonance of around 1 kHz which is known as pinned-pinned resonance, the wavelength of traveling bending wave is twice the sleeper spacing (Grassie et al., 1982). Therefore, the pinned-pinned resonance is believed to be influenced by the spacing between the discrete supports as well as the bending and shear properties of the rail (Thompson, 2009). It was also mentioned that the support spacing may affect the rail resonance. Similarly, (Papaioannou, 2018) concluded that implementing a non-uniform distribution of the sleepers can affect the pinned-pinned and rail resonances.

The deterioration of sleeper in the vicinity of IRJs can be considered as one of the failure modes beside the bolt loosening and broken rail and joint bars using the step mechanism at insulated rail joint (Zong, 2013). The generation of step mechanism is believed to result in a hit to second rail which produce a high dynamic force. The figure 2-10 shows the generation of step mechanism in the presence of IRJ.

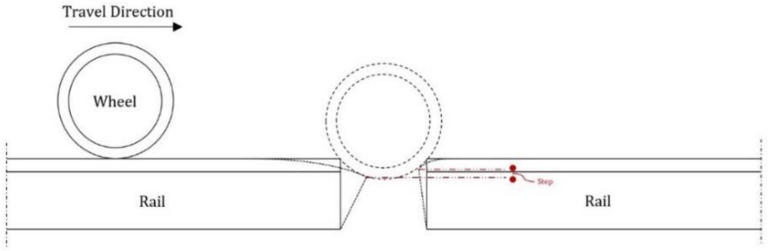

Figure 2-10 Step mechanism in the presence of IRJ

2.5.2.4 Speed and Axle Load Related Conclusions

(Sadri & Steenbergen, 2018) claimed that trains speed and soft substructure increases the degradation rate. It was mentioned that the unsprung vehicle mass doesn't have significant effect on the degradation rate of the track.

(Koro et al., 2004) found that the impact force is highly sensitive to the gaps size for the speed less than 150 $\frac{km}{h}$. Moreover, it was deduced that the impact force is insensitive to the speed of the train. The same conclusion was proposed by (Wen et al., 2005) while it was stated that the impact force is varied with the static axle load.

(Cai et al., 2007) concluded that the effect of train speed is more than the axle loads when it comes to the contact force, stress and strain. It was also shown that the height difference can significantly influence these outputs. Similarly, (Kabo et al., 2006) observed that impact load increases with train speed and joint depth. (Spiroiu, 2016) concluded that the train speed and the unsprung mass possess the highest effect on the wheel-rail dynamic overloads. On the other hands, the sprung mass is believed to have little effect on the dynamic forces.

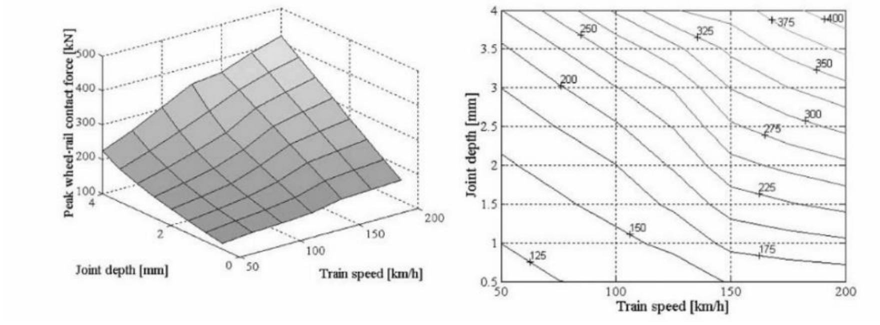

Figure 2-11 Influence of train speed and depth of joint on calculated peak impact force (kN): surface plot (left); contour plot (right) (Kabo et al., 2006)

2.6 Implicit and Explicit FEM Analysis

The finite element method is a numerical problem-solving technique that uses general continuum mechanic concept to assess the design features in various engineering fields. In a general overview, the FEM subdivides a large system into smaller parts that are named finite elements. These elements are obtained through the discretization techniques which is known as meshing (*Finite element method - Wikipedia*, n.d.). In FEM, the computers are utilized to solve the linear and nonlinear matrix equations. These matrix equations include the relation between the stiffness, displacement and the force applied on the structure (Dean, n.d.). The static and dynamic problems can be analyzed using these matrix equations.

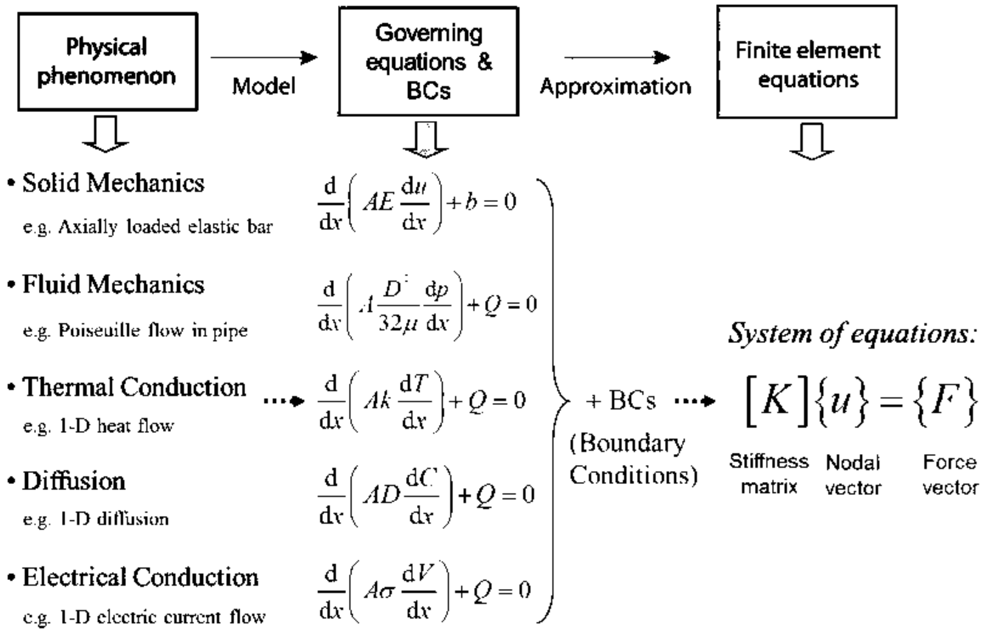

Figure 2-12 Overview on calculation procedure in FEM (Finite Element Method - Introduction, n.d.)

In order to tackle with the nonlinear problems, implicit FEM analysis produce the solution in several steps where the solution for each step is based on the solution for the previous step (*What are the differences between implicit and explicit?*, n.d.). These solutions are obtained using the iteration to verify the global equilibrium at each time increment. Implicit analysis inverts the stiffness matrix over the course of a load/time step. According to (*Implicit vs Explicit FEM*, n.d.), although these solutions are unconditionally stable, the extreme time-consuming procedure, particularly in large models, is a disadvantage of implicit analysis. Therefore, it is recommended to use implicit FEM analysis when the events are slow and a simple static equilibrium exist.

Explicit FEM analysis uses a similar procedure where stiffness matrix is updated at each increment. Despite that the local finite element variables are calculated instead of the global equilibrium. The explicit FEM analysis provides the opportunity to attain faster solution when dynamic analysis is the concern. Based on (*What are the differences between implicit and explicit?*, n.d.), explicit analysis is able to obtain the nodal accelerations directly by multiplying the inverse of the diagonal mass matrix by the net nodal force vector. The acceleration at time n is used to calculate the velocity and displacement at n+0.5 and n+1 respectively . The displacement is further used to determine the strain and the stress can be found using the strain value. Based on (*Implicit vs Explicit FEM*, n.d.), explicit analysis is not unconditionally stable which shows the essence of implementing smaller time steps. It should be noted that the time step used in the explicit analysis must be less than the time for the sound wave to travel across an element which is known as Courant time step. The critical time step is defined as division of the length of the element by the wave propagation velocity ($\Delta t_{min} = \frac{l}{c}$), where wave propagation velocity is calculated from square root of Young's modulus (E) over the density (ρ). The critical time step discussed in chapter two is multiplied by a scale factor of 0.9 by LS-DYANA for stability reason.

2.7 Design of Experiment (DOE) algorithm

Despite of the great technological enhancements in analytical methods and instrumentation, sample preparation is still one of the most important steps that is essential for obtaining accurate and reliable results. In order to perform the optimization step in a system, the influence of factors should be monitored initially. This step requires a huge number of experiments leading to an increase of time as well as the cost of the research. Therefore, studies employ multivariate measures to develop an optimization technique with the highest performance which can reduce the time and the cost of the study .(Müller et al., 2019)

Design of experiment (DOE) is one of the tools which can reduce the time, effort and resources and allows collection of huge number of data while the number of the experiments are limited in an efficient manner. According to (*Boeing Frontiers Online*, n.d.), the statistical analysis in DOE allows determination of various factors at different levels to introduce the most reliable and efficient combination of factors to perform the experiment.

The *factors* or independent variables are those variables that are considered as the certain cause which influence the phenomenon studies. These variables can be changed independently. Based on (*Experimental Design (DOE) economically maximizes information*, n.d.), the factors are divided into two types: Controllable and uncontrollable factors. The controllable factors are those parameters that can be modified in the process while uncontrollable factors cannot be changed in the entire process. The factors can present dissimilar values which are called *levels* of the factor. The *response* or dependent variables are the determined values of the experiments that may be influenced by the input factors.

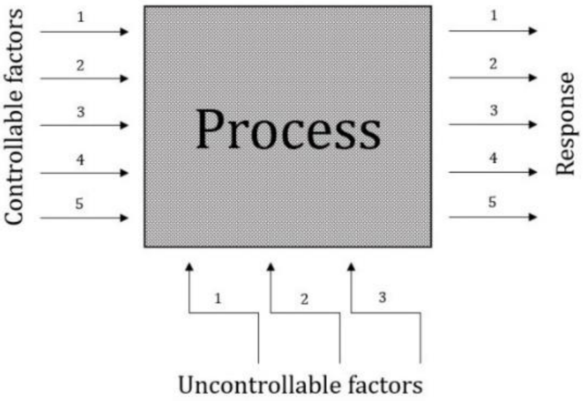

*Figure 2-13 Process factors and responses (*Design of Experiments - A Primer*, n.d.)*

According to (Müller et al., 2019), the DOE includes two main steps:

- Screening design: The purpose of this step is to identify the most influential factors by evaluation of various factors in small number of experiments. The screening step employ three different techniques, each suitable for specific number of factors and levels:
    - Full Factorial Design (FFD): It evaluates the response of all possible combination of factors and levels to provide the information about the main effect and interactions. The number of combinations can be found from the formula: $N=L^k$; where N is the number of experiments, L is the number levels and k is the number of factors of a system. FFD is suitable with studies investigating on fewer than five factors.
    - Fractional Factorial Design (FrFD): This method evaluates the response the factors and levels as well. Since, FrFD is able to reduce the total number of runs when number of factors increase, this method is considered as a subset of FFD experiments. Therefore, FrFD is suitable for experiments with more than 4 factors. The sample size of the FrFD may be one-half or one-quarter of a full factorial design.
    - Plackett-Burman Design (PBD): This method is employed for robustness evaluation, as it considers that some interactions can be entirely disregarded by considering the main effects. PBD evaluate N experiments by allowing a maximum of $k=N-1$ factors, where N is a multiple of four.
- Optimization design: The outcome of screening stage identifies the significant factors involves in the study. The optimization design examines the factors to find the optimum conditions. The response surface methodology (RSM) consists of a sequence of mathematical as well as statistical techniques based on factorial design which describe the behavior of the observations to make statistical predictions. RSM includes six main tools which three most popular tools in DOE optimization stage are discussed below:

- Central Composite Design (CCD): It is the most prevalent second-order design which can be used for modelling processes considering two or more factors. CCD includes three stages: full/fractional two-level factorial design, star design and a center point. The factors in CCD are studied in five levels and the number of experiments can be found from: $N=2^k+2k+C_p$, with k being the number factors and C_p is the number of central points. There are three types of CCDs; circumscribed, inscribed and faced which the applicability of each type is determined based on the number of the factors and the desired properties of the design. In terms of accuracy, circumscribed, inscribed and faced are the most to least accurate methods respectively.
- Box_Behnken Design (BBD): It is utilized for three or more factors with three levels with consistent spaced intervals between levels. The number of experiments is defined by: $N=2k(k-1)+C_p$, with k being the number factors and C_p is the number of central points.
- Dohlert Design (DD): Since Dohlert Design requires a less number of experiments, it is known as the most practical and economical alternatives to other second-order designs. The number of levels is not consistent for all factors which this feature is important for factors that are required to be considered with different levels. The number of experiments is defined by: $N=k^2+k+C_p$, with k being the number of factors and C_p is the number of central points.

The overview of the classification of designs of experiments can be seen in figure 2-14.

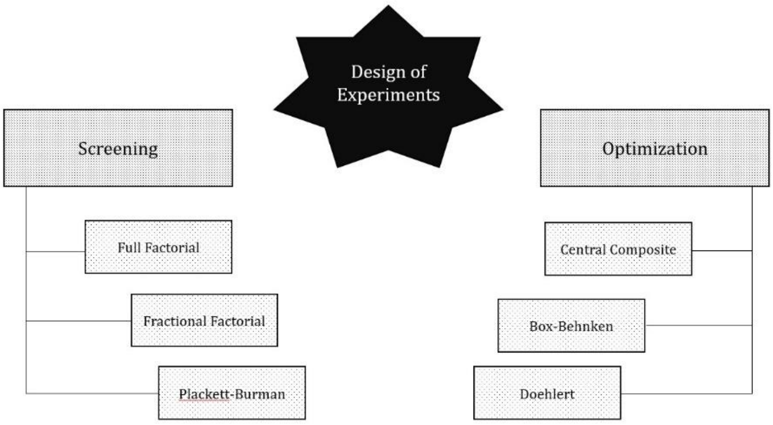

Figure 2-14 Classification of designs of experiments

3

Finite Element Model

In this chapter, a detailed description on the utilized 3D FE model is provided. The original wheel-rail FE model is established by (Yang, 2018) providing set of codes in two FE software packages; ANSYS for implicit analysis and LS DYANA for explicit analysis. The application of latest versions of this software brought the essence of validation of the new proposed FE model against the outputs of the original FE model.

3.1 Train-Track 3D Finite Element Model

3.1.1 Geometries

The 3D FE model that is used in this thesis was originally proposed by (Yang, 2018) using ANSYS APDL 15. This model included 16 concrete sleepers with the spacing of 600mm. Moreover, 2 timber sleepers were placed beneath the insulated rail joint and 2 joint bars were implemented to connect the adjoining rails at the IRJ. The vehicle suspension system, fastening system, rail pad and ballast were simulated as combination of springs and dampers that were calibrated against the field measurements. Moreover, the wheel and axle were designed and placed on the rail. The 8 mass elements representing the carbody are connected to the axle through spring and dampers. The overview of the model is presented in figure 3-1.

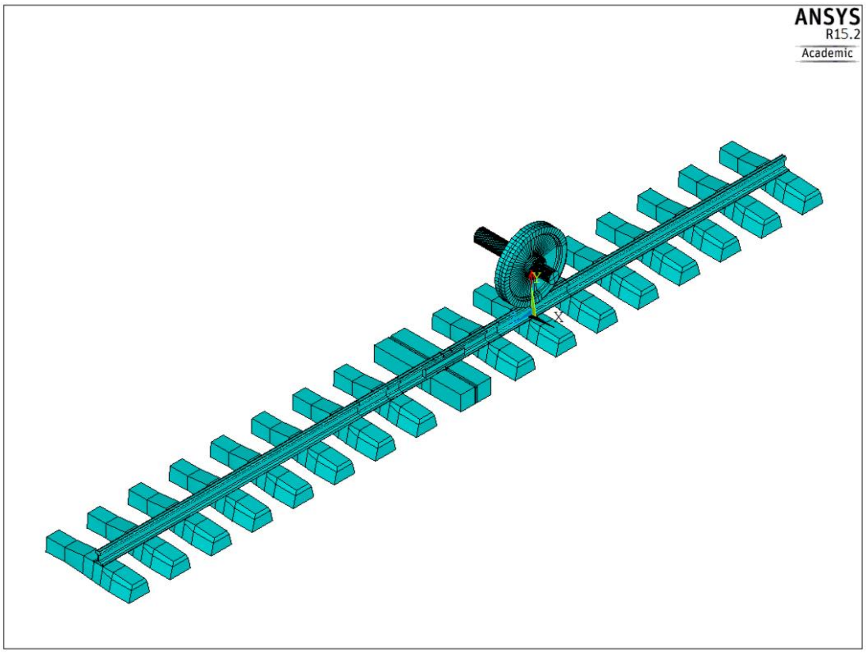

Figure 3-1 Overview of the 3F FE model

3.1.2 Element Types and Material Properties

In order to obtain reliable result, the choice of element types and material models are the important concern in any FE model. Moreover, as both implicit and explicit FEM analysis is implemented in this research, different models of element type had to be chosen in each analysis. The wheel, rail, joint bars and sleepers are modelled using SOLID185 in the implicit analysis (*ANSYS Mechanical APDL Element Reference*, n.d.). This element type is a solid element with eight nodes having degree of freedom in transitions in three directions. SOLID185 is converted to SOLID164 for explicit analysis. This element is defined by eight nodes with the degree of freedom in transitions, velocities and accelerations in x, y and z directions which made it suitable for explicit analysis (*ANSYS Mechanical APDL Element Reference*, n.d.).

Although timber is an orthotropic material and concrete sleeper is equipped with reinforced steel rode, an isotropic material model is assigned to all components that are used in this model (Yang, 2018). The wheel, rail and joint bars are made of steel materials with the same modulus of elasticity, poison ratio and material density. The mechanical properties of components used in this FE model can be seen in the table 3-1.

Table 3-1 Mechanical properties of track components

Component	Material	Modulus of Elasticity	Poisson's Ratio	Density	Yield stress	Tangent Modulus
Rail and Joint bar	Steel	210 GPa	0.3	7800 kg/m^3	500 MPa	21 GPa
Wheel	Steel	210 GPa	0.3	7800 kg/m^3	500 MPa	21 GPa
Concrete Sleeper	Concrete	38.4 GPa	0.2	2520 kg/m^3	-	-
Timber Sleeper	Wood	20 GPa	0.2	1300 kg/m^3	-	-

As it was discussed above, the vehicle suspension system, fastening system, rail pad and ballast were simulated as a combination of spring and damper elements. In the implicit analysis, COMBDIN14 based on its capability in longitudinal translation and torsional rotation in all directions while this element type was converted to COMBI165 in explicit analysis. Since explicit dynamic analysis are often characterized in terms of force-displacement curves, COMBI165 is popular due to its ability of modeling complex force-displacement relations (*COMBI165*, n.d.). The application of spring and dampers required an extensive calibration procedure which resulted in introduction of 27 pairs of linear elastic spring and viscous dampers for each fastening system including rail pad and 15 pairs of linear elastic springs and viscous dampers for ballast connected to the bottom of each sleeper (Yang et al., 2018).

The vertical and lateral calibrated values of the spring and damper elements that are implemented instead of suspension system, fastening system, rail pad and ballast can be seen in the table 3-2 and 3-3 respectively.

Table 3-2 Calibrated values of vertical spring and dampers

Parameters			Calibrated Values
Fastening System (Rail pad)	above Concrete Sleepers	Stiffness	0.722E+07 N/m
		Damping	0.25E+04 Ns/m
	above Timber Sleepers	Stiffness	0.321E+07 N/m
		Damping	0.167E+04 Ns/m
Ballast	beneath all Sleepers	Stiffness	0.3E+07 N/m
		Damping	0.213E+05 Ns/m
Suspension System	-	Stiffness	0.144E+06 N/m
		Damping	312 Ns/m

Table 3-3 Calibrated values of lateral spring and dampers

Parameters			Calibrated Values
Fastening System (Rail pad)	above Concrete Sleepers	Stiffness	0.208E+07 N/m
		Damping	833 Ns/m
	above Timber Sleepers	Stiffness	0.321E+07 N/m
		Damping	833 Ns/m

In order to model the mass of the carbody and bogie, 8 and 4 point elements using MASS21 are implemented respectively. According to (*ANSYS Mechanical APDL Element Reference*, n.d.), this element type is defined by a single node, concentrated mass component which has 6 degrees of freedom; transitions and rotations about the x, y and z axes. The 8 nodes representing the carbody can be found in figure 3-2.

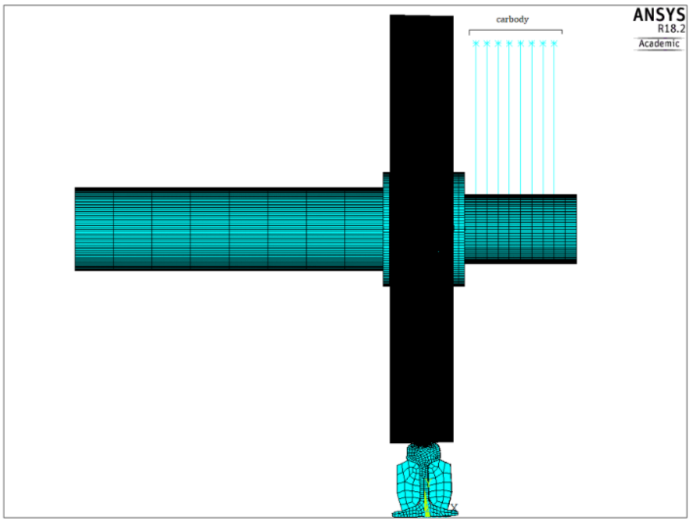

Figure 3-2 Overview of the wheel, axle and carbody formation

3.1.3 Constrains

The bottom ballast nodes are fixed in lateral (x), vertical (y) and longitudinal (z) directions while upper nodes which are connected to the bottom of sleepers are constrained in longitudinal and lateral directions. The upper and bottom nodes of the fastening system and rail pad elements are connected to the rail and sleeper respectively. These nodes are constrained in longitudinal and lateral directions. The bottom nodes of the rail pad elements which are connected to the elements on the top of sleeper and the upper nodes of the ballast elements connected to the elements on the bottom of sleeper are coupled in the vertical direction. The 8 point elements representing the carbody are coupled and fixed in lateral direction. The left side of the wheel axle is constrained in lateral direction. Although free boundaries were used on the rail ends at the joint, non-reflecting boundaries were proposed at the far ends of the rails. This is believed to enable the waves to exist the domain without being reflected and disturb the numerical results.

3.1.4 Contacts

The FE model defines the rolling contact pairs between the wheel and rail as well as the joint bar and rail. Two types of elements, CONTA174 and TARGE170, are implemented to define the contact between these components. CONTA174 is used to present the contact and sliding between 3D target and the deformable surface that is defined by this element type. This element has the ability of translation in x, y and z directions. TARGE170 is used to represent the 3D target surfaces for the CONTA174 element (*ANSYS Mechanical APDL Element Reference*, n.d.). As it can be seen in figure 3-3 (a), the contact element may have similar geometric shape as the solid or shell element face that it is connected. Therefore, it can overlay the solid elements which provide the boundary of a deformable surface that can be in contact with the target surface, defined by TARGE170. The translational or rotational displacement can be imposed on the target segment element. The contact and target elements can also be seen in figure 3-3 (b).

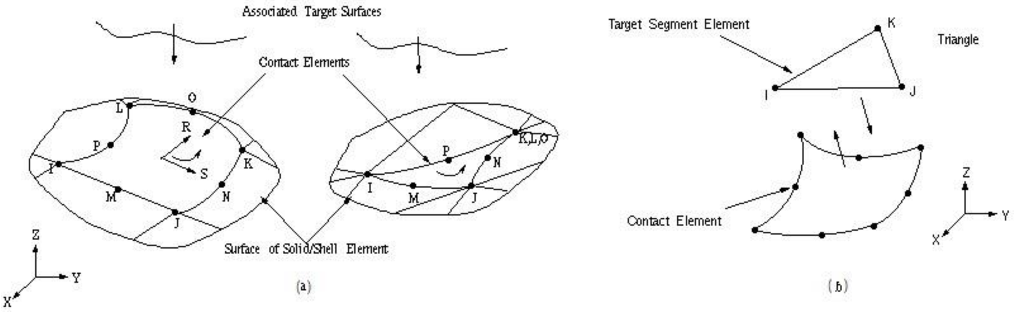

Figure 3-3 Application of contact and target elements (a) Contact element and surface; (b) contact and target element

The friction of coefficient was defined as 0.35 which is believed to result in the most validated model. Besides, the contact algorithm used the Augmented Lagrangian formulation. This optimization method can be used for nonlinear solid body contact of faces by utilizing the penalty-based contact formulation ($F_{Normal} = K_{Normal} \times U_{Penetration} + \lambda$) which can be seen in figure 3-4. To implement the penalty contact algorithm, the master and slave segments must be introduced. Therefore, the master and slave segments are defined on the rail top and wheel tread respectively.

Based on (*Augmented Lagrangian Methods*, n.d.), Augmented Lagrangian method seeks a solution by minimizing the outputs with the updates of λ. The λ results in less sensitivity of the F_{Normal} to the contact stiffness (K_{Normal}).

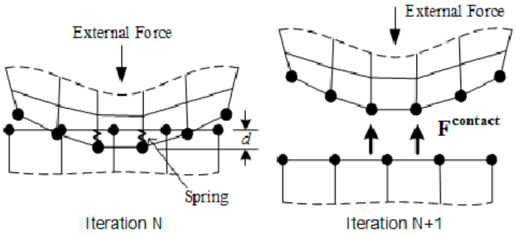

Figure 3-4 Contact formulation

3.1.5 Loads

In the implicit analysis, the bolt pretension force and gravity are applied to the insulated rail joint model. The gravity load is determined by the density of the rail, fishplate, concrete and timber sleepers as well as the carbody and bogie. The two latter loads are applied by implementing the mass point elements which was discussed in the previous part.

The application of pass-by wheel in this model results in the generation of dynamic forces. The dynamic excitation force, which depends on the time, can be determined using the defined contact between the wheel and the rail. Therefore, the output related to RCFORC can be used to determine the excitation force which is applied by the wheel. A sample of the contact force between the wheel and the rail can be seen in figure 3-5.

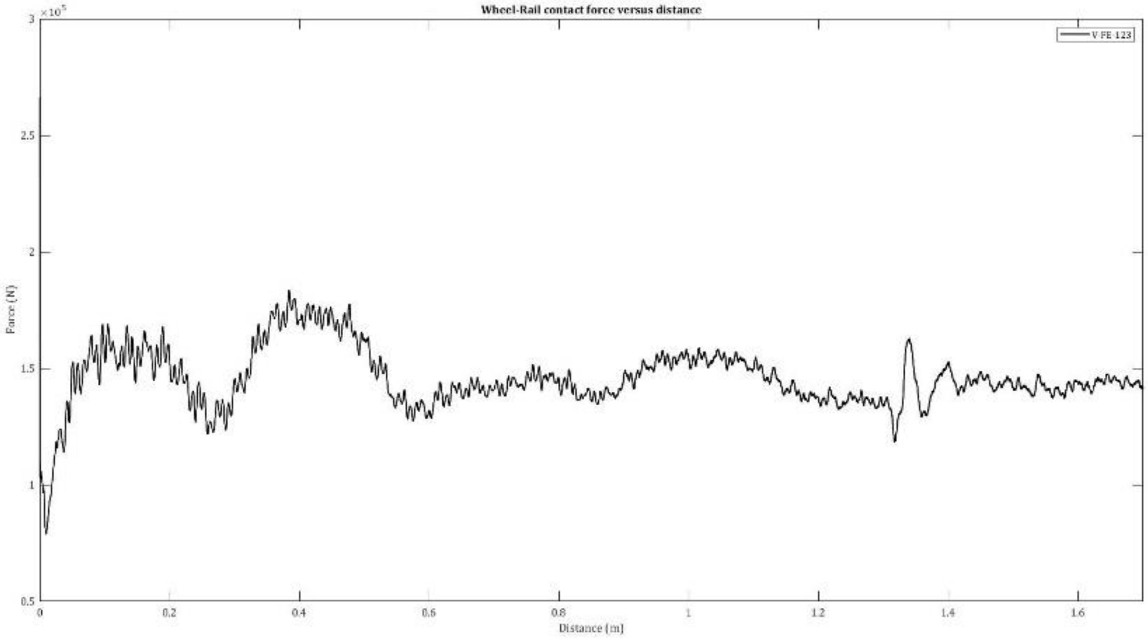

Figure 3-5 Contact force between the wheel and rail

3.1.6 Speed

In order to determine the impact force and the vibration of the rail, the wheel is considered in this finite element model. The determination of the dynamic effects of the pass-by wheel requires assignation of speed to the wheel and carbody. Since, the wheel considered in this model is a traction wheel, two types of velocities exist. The total velocity starts with an initial velocity that is assigned to the carbody which later increases with the rotational velocity that is assigned to the wheel.

In order to perform the comparison between the models with different speeds, the variation in the relaxation time must be considered. Therefore, the time which each system returns into equilibrium is different due to the variation of speed. This is discussed further in chapter 5.

3.1.7 Meshing

In order to obtain accurate result in a computationally efficient way, variant meshing pattern was implemented in this FE model. In the implicit FE analysis, that static wheel is placed on the track to determine the initial conditions for further dynamic analysis. In order to obtain accurate results, finer mesh size of 1mm is used for this particular part of the rail which can be seen in figure 3-6 (a). Besides, in explicit FE analysis, the wheel moves on the rail which results in generation of vibrations of the components. Since accurate results regarding the vibration and impact force are crucial to be obtained near to the IRJ, the finer mesh must be implemented with moving to the vicinity of this location. The meshing pattern in vicinity of IRJ can be seen in figure 3-6 (b). The meshing pattern used for the joint bars, wooden and concrete sleepers are invariant for the entire FE model.

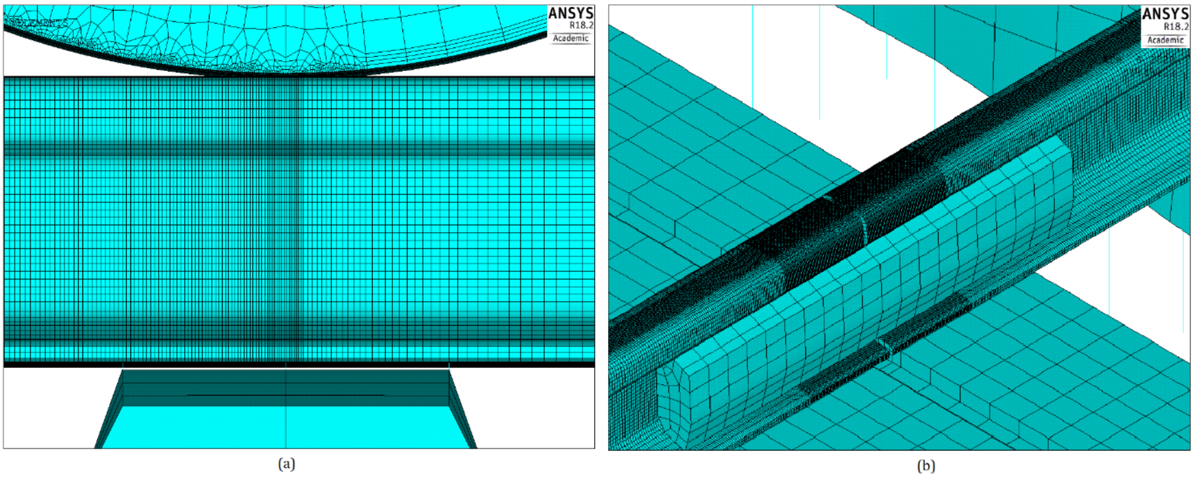

(a) (b)

Figure 3-6 Overview of meshing pattern (a) Under the wheel; (b) At the IRJ

3.2 Simulation Process

3.2.1 ANSYS Implicit Analysis

In general, in order to trace the system's variable in the dynamic systems, the initial conditions are required (*Initial condition - Wikipedia*, n.d.) In this research, implicit solver of the ANSYS Mechanical and CFD is utilized to determine the initial condition. This quasi-static analysis calculates the response of the rail under the gravity of the track components, wheel, bogie and carbody loads as well as the action of bolts pretension. The small displacement static analysis with 6 number of substeps are chosen for this implicit analysis.

The vertical stress distribution on the rail surface can be seen in figure 3-7. Besides, the elliptical contact patch can be seen in this figure. It is fair to say that elliptical contact patch can be one of the factors regarding the validation of the correct simulation of implicit analysis since the similar contact area by Hertzian classical contact theory for non-conformal bodies are achieved.

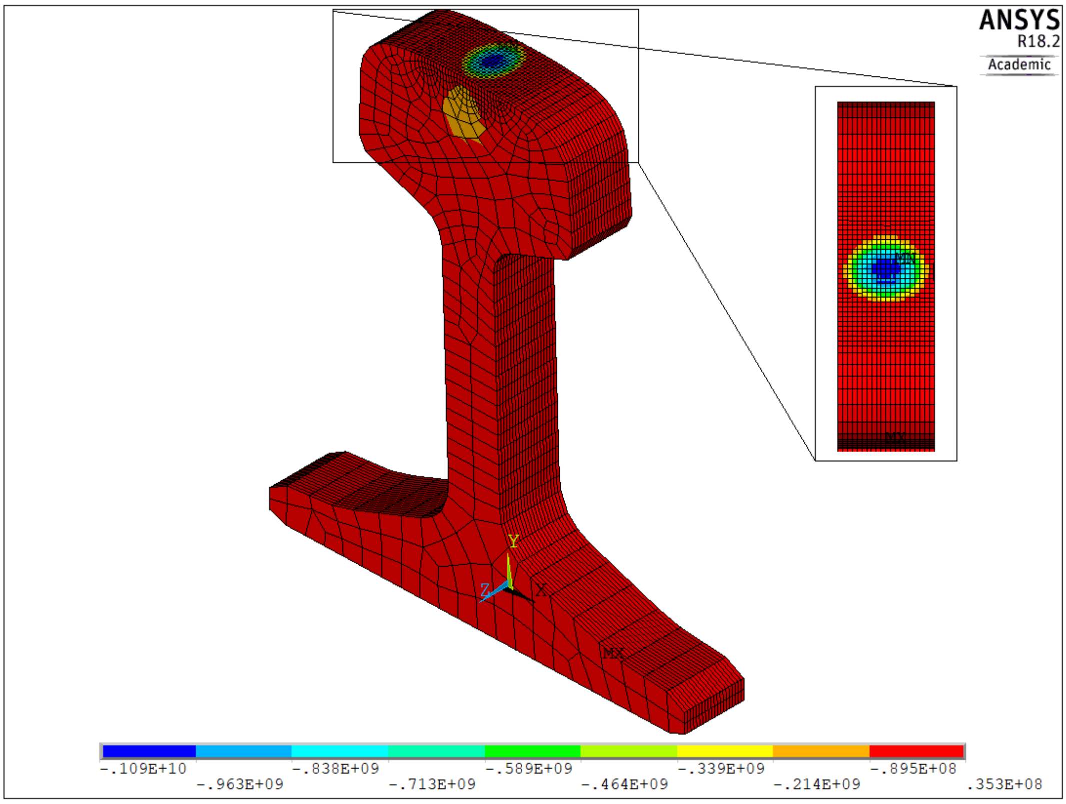

Figure 3-7 Vertical stress distribution on rail surface

3.2.2 LS-DYNA Explicit Analysis

In order to perform the dynamic analysis, explicit and implicit solvers can be implemented. Due to the ability of the explicit analysis in handling the nonlinearities more quickly than implicit analysis, the explicit solver is used to analyze the dynamic behavior of this FE model. Therefore, the nodal displacements and stresses which are written in a text file are used as the initial conditions for the explicit analysis. In order to trace the impact force as well as the dynamic behavior of the track, the wheel is required to pass the IRJ. Therefore, the simulation time is set to 0.06 seconds which allows the wheel to pass the joint considering the velocities of at least 90km/h.

In order to assess the information about the wheel-rail interaction as well the vibration of the track, certain outputs are required to be obtained. These outputs include the time history (D3THDT) and the contact force (RCFORC) where acceleration, velocity, displacement and the contact force between the defined components can be determined respectively. After the implicit to explicit conversion is done successfully, two text files including the displacement information in drelax file and the k file which contains the detail information about the FE model are generated. The k file contains the node, section and material definition as well as the information about the contacts, constrains, loads and velocity of the moving particle. The k file and drelax file are then used as the inputs for LS-DYANA explicit solver. The computational time for the model used in this research is approximately 13-14 hours.

3.3 Validation of the FE Model

The original FE model is created by implementing a series of codes proposed by (Yang, 2018), which convert a simple wheel-rail FE model to the model which was shown in figure 3-1. These series of codes were implemented in the ANSYS APDL 15. In order to achieve the objectives of this research, the original FE model must be modified and new models with variation of sleeper spacing had to be generated. Therefore, the sleepers are required to be removed and new sleepers must be created at desired positions. This procedure involves the remeshing of the rails above the new generated sleepers.

Due to the dissimilar meshing techniques that are implemented in new versions of ANSYS, the issue regarding the incapability of the codes related to the original FE model arose. Therefore, the codes were required to be modified through an extensive comparison between the original FE model created in ANSYS APDL 15 and the model which is created in ANSYS APDL 18. In order to use the model created in new version of ANSYS in the entire stages of this research, it had to be validated against the model created in ANSYS APDL 15. The validation involves the comparison of the power spectral density of the vibration of two models in frequency domain as well as the evaluation of the contact forces in time domain. The conformity of the dominant frequencies including the pinned-pinned resonance as well as the impact force is an important factor that is used to perform the comparison in the validation step. Therefore, the vertical acceleration of the elements in the mid-span are obtained and the PSD versus the frequency is plotted in figure 3-8. The comparable data especially at the dominant frequencies and the impact force in time domain shows that the validation is performed successfully and therefore, the new model generated in ANSYS APDL 18 can be used for further investigation.

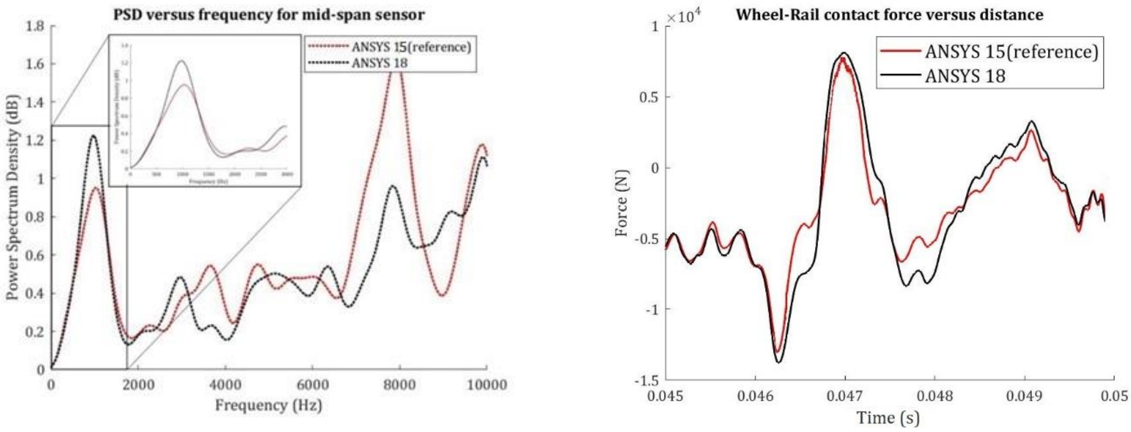

(a) (b)

Figure 3-8 Validation of the new model and original model, (a) impact vibration (b) impact force

4

Parametric Studies -
Vary the Sleeper Spacing

In this chapter, a parametric study is conducted where the sleeper spacing is varied to assess the effects of the sleeper spacing on the performance of the track. The performance of IRJ, i.e. the magnitude of the impact force and track vibration. The analyses are performed in both the time and frequency domains.

4.1 Overview on the Models

In order to analyze the effects of the sleeper spacing on the dynamic behavior of the track, the new FE models were proposed. The sleeper spacing is varied in each new submodel with the aim of understanding the effects of various arrangements of sleepers on the impact force as well as the vibration of the track. As discussed in chapter 3, the original FE model contains 2 timber sleepers beneath the IRJ while the rest of the sleepers are modelled using different geometry with the concrete material properties. The speed of the wheel is 100km/h. As it can be seen in figure 4-1, the spacing between all sleepers is 600mm in the original FE model.

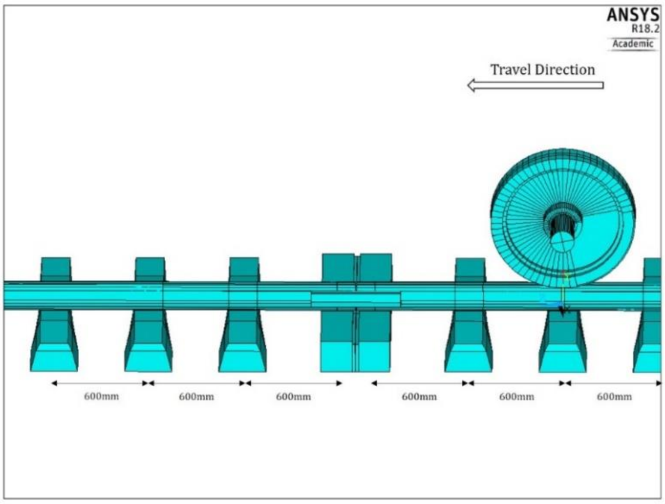

Figure 4-1 Overview of the original FE model

As various submodels are proposed in this research, a specific representation pattern, which can be seen in figure 4-2, is used to let the readers simply understand the properties of each model.

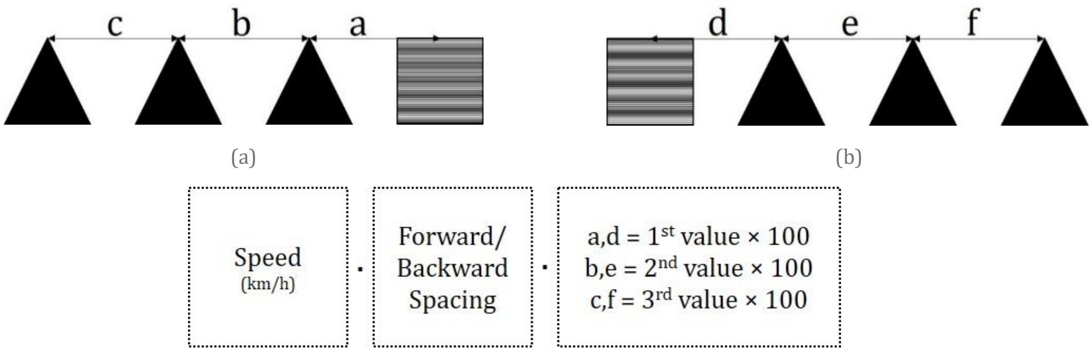

Figure 4-2 Arrangement of the Sleepers in Submodels (a) sleeper spacing after IRJ; (b) sleeper spacing before IRJ

For instance, 100.F.666 represents the submodel with the speed of 100km/h with the forward sleeper spacing of 600mm, 600mm and 600mm respectively.

Since this chapter aims to determine the effects of the sleeper spacing on dynamic behavior of the track in the presence of the insulated rail joint, the position of sleepers in vicinity of the IRJ are altered. Therefore, the original spacing of 600mm is fixed for sleepers far from the IRJ.

In order to assess the effects of sleeper spacing on the dynamic behavior of the track, the sleeper arrangement before and after the IRJ are altered individually. Besides, the application of non-uniform sleeper spacing is believed to provide a closer insight of the effects of the variation of this parameter on the dynamic of wheel-rail interaction such as dynamic impact force and the vibration of the track.

The 100.F.576 and 100.B.576 are proposed with the aim of moving 1st sleeper after and before the IRJ by 100mm near to the joint. Therefore, the sleeper spacing between the timber and 1st concrete sleeper before and after the IRJ is 500mm in each model. In 100.F.756, the 1st concrete sleeper after the IRJ was shifted by 100mm farther. This arrangement is believed to be an aid to understand the effects of the sleeper spacing variation regardless of its distance to the IRJ.

In 100.F.444, a consistent sleeper spacing equal to 400mm after the IRJ was proposed. Therefore, the 1st, 2nd and 3rd sleeper spacing after the IRJ is fixed to 400mm while the rest of the sleeper spacings remain unchanged. This pattern was changed in 100.F.345 where variant sleeper spacing after IRJ was implemented. The 1st, 2nd and 3rd sleeper spacing after the IRJ is fixed to 300mm, 400mm and 500mm respectively.

Finally, non-uniform sleeper spacing behind the IRJ is implemented in the last proposed model. Therefore, the 1st, 2nd and 3rd sleeper spacing before the IRJ is fixed to 300mm, 400mm and 500mm respectively in the 100.B.345. The arrangement of the sleepers is illustrated in figure 4-3 (a) – (f).

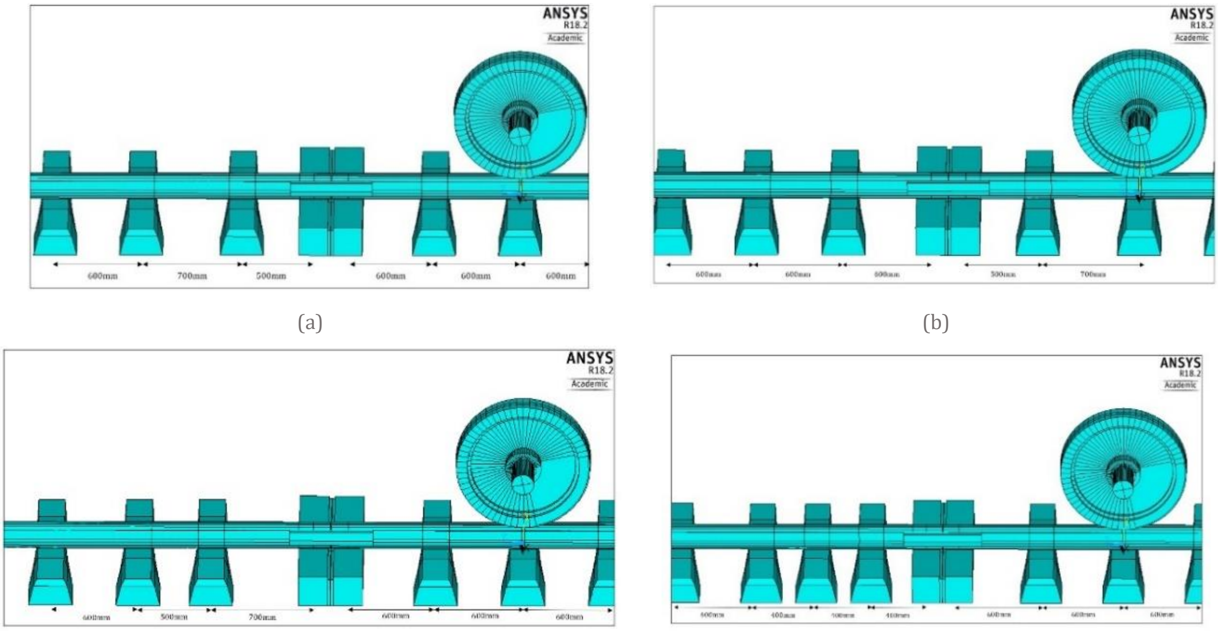

(a) (b)

(c) (d)

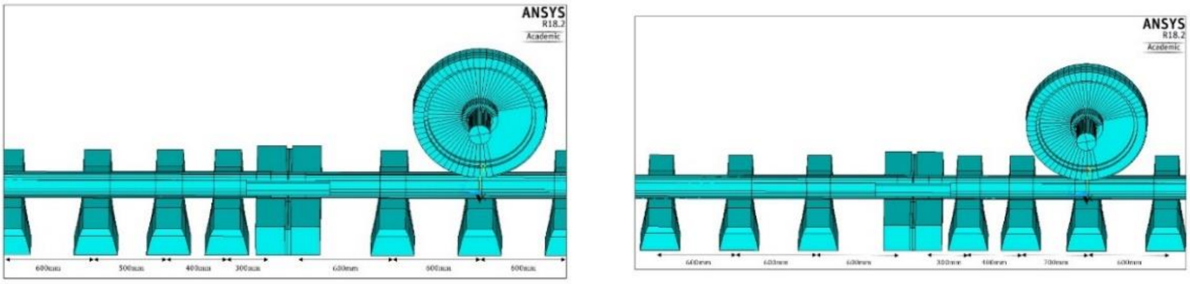

(e) (f)

Figure 4-3 Overview on arrangements of sleeper spacing in proposed submodels; (a) 100.F.576, (b) 100.B.576, (c) 100.F.756, (d) 100.F.444, (e) 100.F.345, (f) 100.B.345

4.2 Comparison Based on Sleeper Spacing Variation

4.2.1 Tools and Techniques

The dynamic behavior of the track includes various dependent variables which may vary from time to time. The vertical vibration of the track as well as the first and second impact forces are the dependent variables which are observed closely in this research.

The impact forces can be determined using RCFORC which is one of the outputs of the explicit analysis performed by LS-DYNA. Moreover, LS-DYANA produces the time history of the vibration of the elements of models. The time history includes acceleration, velocity and displacement. This study implemented the vertical (y-direction) acceleration as the mean to further investigate the effects of sleeper spacing.

The post-processing of the data is performed using the software LS-PREPOST. This software is able to read the output files produced by explicit solver of LS-DYNA. The displacement, velocity, acceleration and energy of the model can be identified globally or by specific parts. The figure 4-4 shows the working environment of the LS-PREPOST.

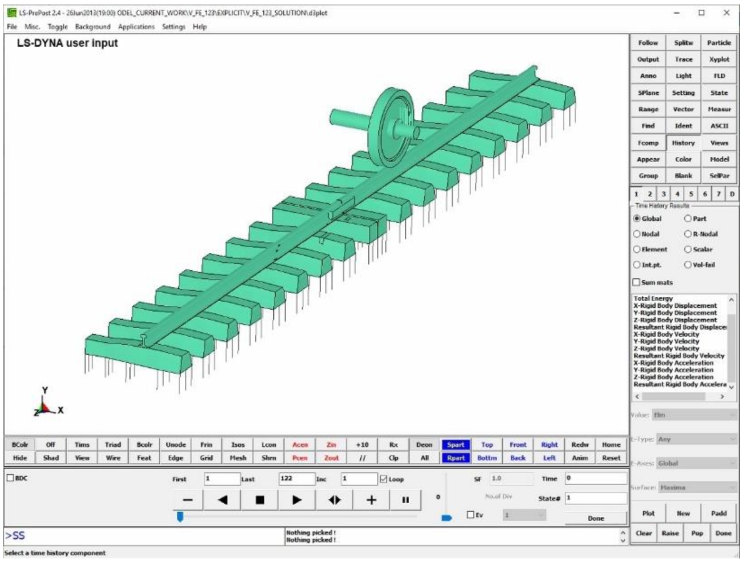

Figure 4-4 Working environment of the LS-PREPOST as post-processing software

In order to compare the dynamic behavior of the track, specific elements are chosen for each model. These elements form the parts which later are used to determine their vibration. The position of these parts is proposed to be consistent with the position of the sensors which may be placed for experimental data acquisition. The Part 18 and Part 19 are proposed to capture the vibrations of the rail adjacent to the IRJ and in the midspan respectively. The position of these two parts can be seen in figure 4-5.

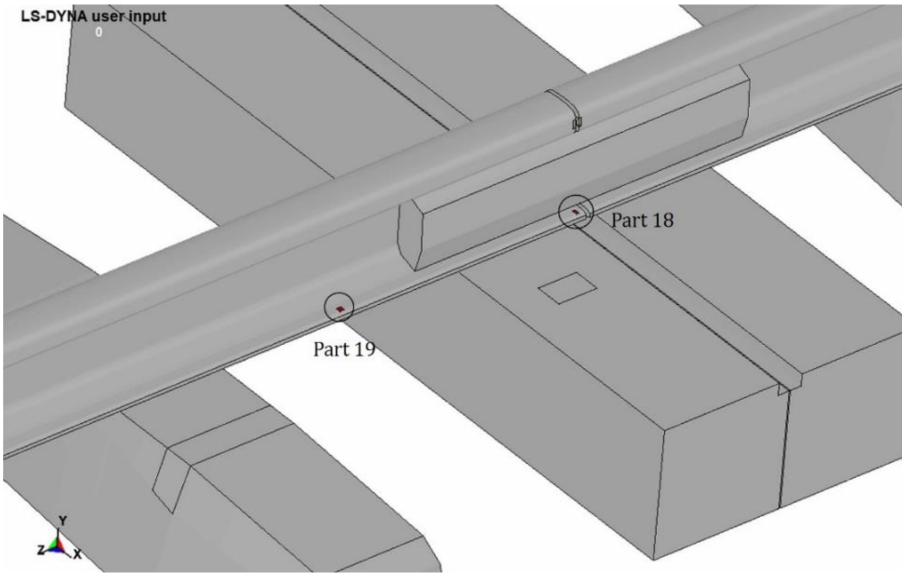

Figure 4-5 Position of part 18 (on-sleeper sensor) and part 19 (mid-span sensor)

MATLAB is another software which is extensively used to perform the post-processing of the data. Various functions and codes are implemented to closely compare the dynamic behavior of the track in all FE models.

The power spectrum of a time series defines the distribution of power into the frequency components that constitute a specific signal. Power spectral density (PSD) is implemented to characterize broadband random signals which can provide a well insight about the power in the frequency ranges. In this research, the power spectral density is used to perform the comparison between the FE models in the frequency range up to 10kHz.

The power spectral density can be determined using periodogram, modified periodogram and welch techniques. In general, the periodogram estimates the PSD through scaling the squared magnitude of the FFT function computed over windowed sections of the input. This estimation is based on the formula:

$$P_{xx}(f) = \frac{1}{LF_s}\left|\sum_{n=0}^{L-1} x_L(n)e^{-j2\pi fn/F_s}\right|^2,$$

where F_s is the sampling frequency, $x_L(n)$ is the signal with the length of L.

The modified periodogram windows the signals in time domain before performing the Fourier transform to smooth the edges of the signal and the height of the sidelobes can be reduced accordingly. The function toolbox *periodogram* in MATLAB allows the users to compute the modified periodogram.

Welch is considered as an improved estimator of the PSD where time series data is divided into segments. Each segment is then computed using modified periodogram. Finally, the average of the PSD estimates will be produced. The welch technique is able to produce the PSD with reduction in the noises. In this research, Welch method is utilized extensively to produce the PSD of the parts 18 and 19. These post-processed data are used to perform the comparison between the FE models. The toolbox function *pwelch* implements Welch's method in MATLAB.

Wavelet power spectrum (WPS) is considered as an appropriate tool for the investigation of non-stationary signal where local changes in the frequency components exist. The WPS of the simulated impact force and vibrations up to 10kHz is used to compare the FE model (Molodova et al., 2014).

4.2.2 Results and Interpretation in Time Domain

4.2.2.1 Impact Force

The contact force between the wheel and rail is one of the outputs of the explicit solver of LS-DYNA which is used in this research. The high-peak force which is generated from the impact between the wheel and rail after IRJ can be extracted from the wheel-rail contact force. The wheel-rail contact and impact force of the original model can be seen in figure 4-6.

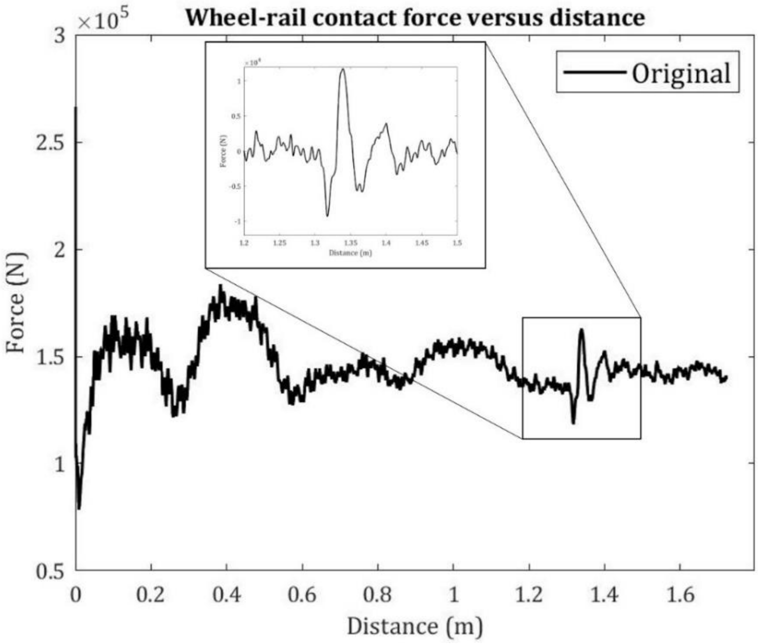

Figure 4-6 Wheel-rail contact force and impact force

As strong changes in stress development occurs in some models, it is difficult to achieve a converged solution for an equilibrium iteration. The dynamic relaxation can be added to stabilize the convergence process. The un-stabilized equilibrium in this FE model can be clearly seen until the distance of 0.6m in figure 4-6. Consequently, the results are trimmed and the outputs after the distance of 0.6m are chosen for further investigation for both wheel-rail contact force and vertical acceleration of the parts.

Since the effect of variation of sleeper spacing on the first and second impact force is to be considered in this research, the results related to the impact forces of the submodels as well as the original FE model are shown in each figure.

According to the impact force of the 100.F.576 and the original model in figure 4-7 (a), it can be seen that the impact force is not affected by reducing the 1st sleeper spacing after the IRJ. Based on figure 4-7 (b), a similar trend has been observed for the 100.B.576 where 1st sleeper spacing before the IRJ was reduced to 500mm. This arrangement resulted in a minor reduction of the second impact force.

As shown in figure 4-7 (c), the impact force is not affected by increasing the 1st sleeper spacing after the IRJ in the 100.F.756. However, the possible improvements can be observed in the 100.F.444 where the 1st and 2nd sleeper spacing after the IRJ were reduced to 400mm.

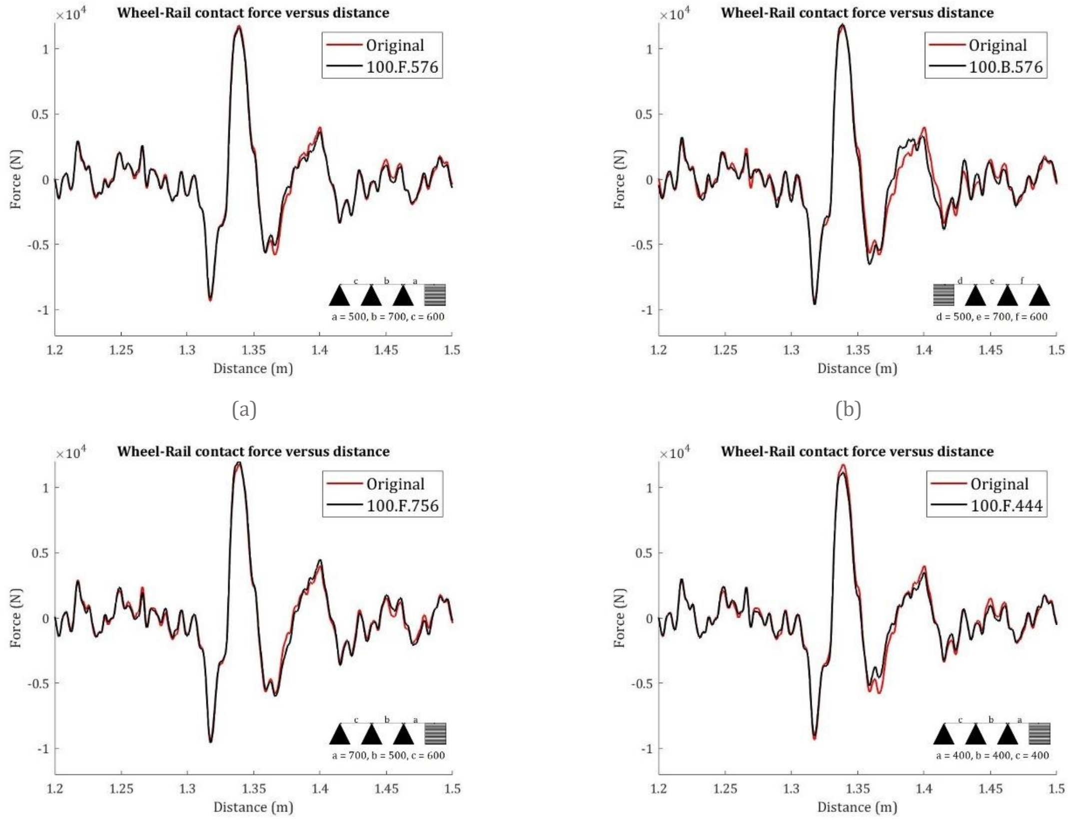

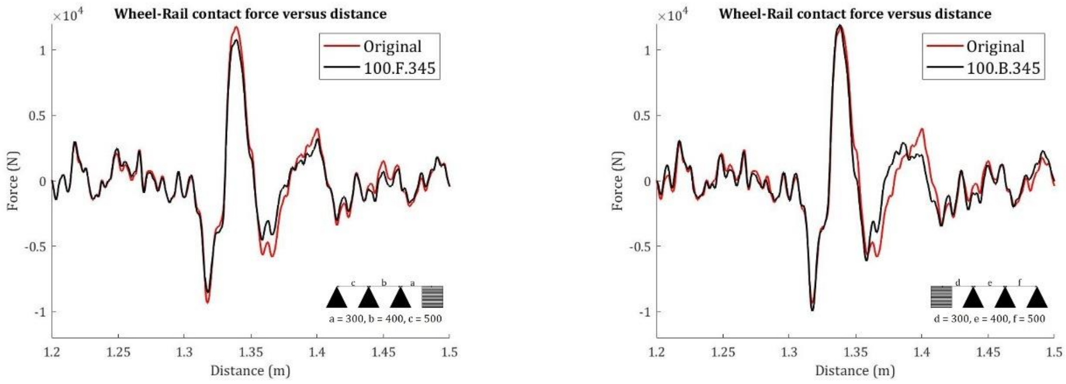

(e) (f)

Figure 4-7 The impact force of the submodels and original model

The consistent sleeper spacing after the IRJ that was implemented in 100.F.444 was altered to a variant arrangement in 100.F.345 which can be seen in figure 4-7 (e). The first impact force is decreased in this model which illustrate the sign of improvements by varying the sleeper spacing after the IRJ. In the 100.B.345, the similar arrangement was utilized for the spacings behind the IRJ. Although there is no improvement in the first impact force, the second impact force was significantly decreased in this model. The result can be seen in figure 4-7 (f).

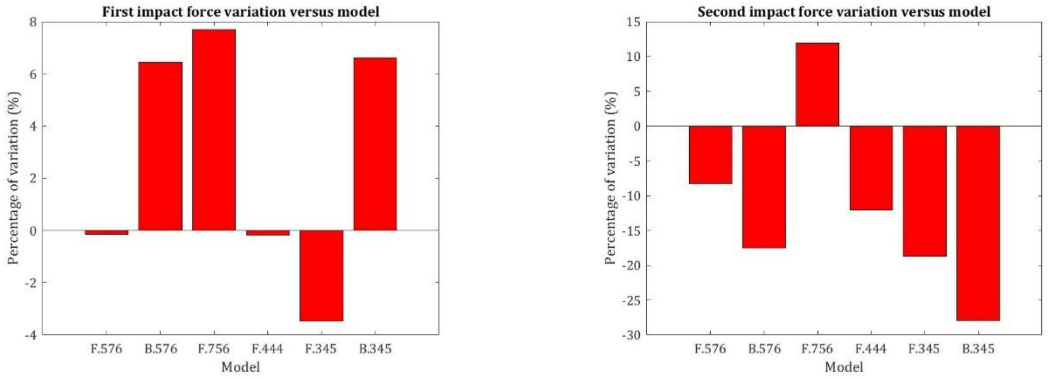

(a) (b)

Figure 4-8 Variation of impact force for the submodels w.r.t original model (a) First impact force; (b) Second impact force

As it can be seen in figure 4-8 (a) and (b), decreasing the 1st sleeper spacing after the IRJ in F.576 does not affect the first impact force significantly while the first and second impact force is noticeably influenced as the result of increasing the 1st sleeper spacing after IRJ in F.756. The implementation of consistent sleeper spacing with the value of 400mm after the IRJ shows an improvement in reduction of the impact force. It should be noted that F.345 is the best submodel in contribution to reduction of the first impact force. Therefore, it can be concluded that varying the 1st, 2nd and 3rd sleeper spacing after IRJ is an effective measure to decrease the impact force. On the other hand, it can be deduced that altering the 1st, 2nd and 3rd sleeper spacing before the IRJ may increase the first impact force whereas this arrangement may contribute to reduction of the second pick of the impact force.

4.2.2.2 Vertical Vibration

The vertical acceleration of the part 18 and 19 was extracted from the outputs using LS-PREPOST. It should be noted that part 18 is the representative of the sensor placed on sleeper beneath the IRJ whereas part 19 is the representative of the sensor placed on the mid-span. The time histories of the vertical acceleration in the submodels and original model can be seen in figure 4-9 (a) – (f). The peak in the vibration due to the impact of wheel to the rail after the joint occurs at 0.047s.

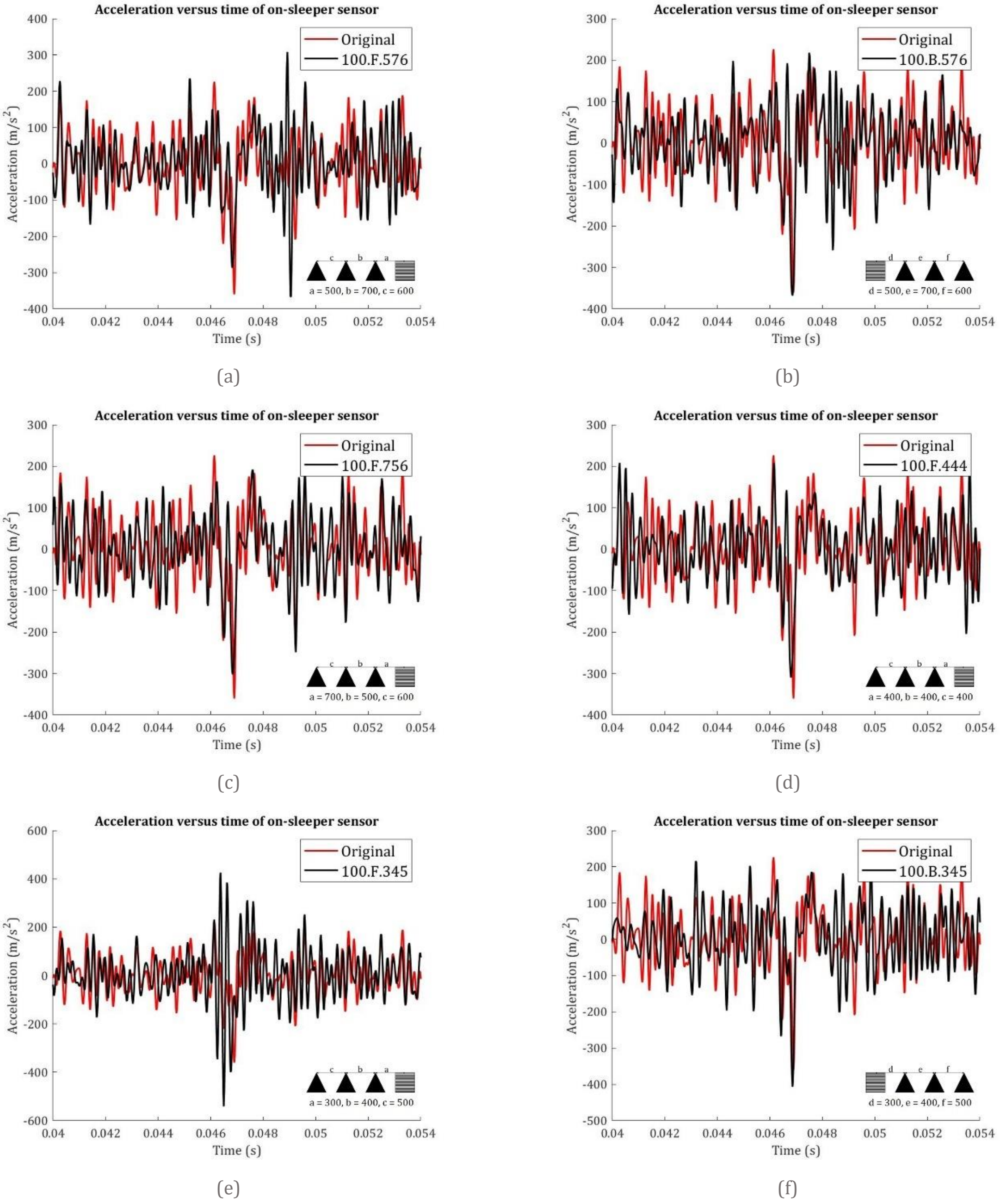

(a) (b)

(c) (d)

(e) (f)

Figure 4-9 The impact vibration of the submodels and original model - vertical acceleration

Based on the results, altering the sleeper spacing before the IRJ does not affect the impact vibration while changing the spacing within sleepers after the IRJ influence the impact vibration significantly. Based on figures 4-9 (a), (c) and (d) the impact vibration is reduced noticeably.

According to figure 4-9 (a), there is a sudden upsurge of the magnitude of the impact vibration after the wheel passed the joint in the case of decreasing the 1st sleeper spacing after the IRJ. From the comparison between figure 4-9 (d) and (e), it is fair to say that implementation of consistent sleeper spacing after IRJ may reduce the impact force, although non-uniform arrangement of sleepers after the IRJ increases the impact vibration significantly.

According to (Xin et al., 2019), a wheel running with speed v over an irregularity of wavelength λ will generate an excitation frequency f which can be determined as follows:

$$f = \frac{v}{\lambda}$$

Since the velocity of all the submodels is fixed to 100km/h (~27.78m/s) and the gap between the two adjoining rails at IRJ is 0.006m, the frequency of the excitation is determined as ~4500Hz.

Generally, when the excitation frequencies are close to the resonance frequency of the track, high oscillation may occur. The arrangement of the sleeper spacing which is implemented in the case of 100.F.345 resulted in a sudden increase of response in the frequencies between the 2kHz-6kHz. Therefore, it can be concluded that due to the sleeper spacing variation in the submodel 100.F.345, the natural frequencies are either increased or coincided with the excitation frequency that resulted in an ultimate increment of vibration of the track.

4.2.3 Results and Interpretation in Frequency Domain

The static approach accounts purely for its elastic properties and the spatial distribution, whereas in a dynamic approach the initial properties will be considered as well. Newton's second law is the basis of structural dynamics in the form of:

$$\vec{\boldsymbol{F}}(t) = \frac{d\vec{\boldsymbol{p}}(t)}{dt} = m\frac{d\vec{\boldsymbol{v}}(t)}{dt} = m \cdot \vec{\boldsymbol{a}}(t)$$

Accordingly, to change the linear momentum of a discrete mass, the application of external force is essential. Since the motion of the inertia can occur as a function of time, the dynamic approach includes the time as another dimension for the analysis whereas a static response requires a time-invariant analysis approach. In a static model, the relationship between input and output is described in terms of an algebraic equation while dynamic model employs a differential equation to describe the relationship between the excitation and response. The general equation of motion accounting for the applied resulting force in dynamic force balance is as follow:

$$m\ddot{x}(t) + kx(t) = F(t)$$

Natural frequency or eigenfrequency is the frequency which a system tends to vibrate in the absence of an external force. The pattern of the motion of a system in its natural frequencies is called normal mode. Since the track structure contains specific vibration modes, it is important to determine the natural frequencies and the relative motion of the structure accordingly. In order to calculate the natural frequencies, the external force is removed from the equation of motion and a homogeneous differential equation is obtained:

$$m\ddot{x}(t)+kx(t)=0$$

The free vibration which is known as the modes of a structure can be characterized by finding the eigenfrequencies, which are purely dependent on the structure properties, as well as the eigenvectors. The general solution of the above differential equation is determined in the form of:

$$x_{\text{hom}}(t)=C_1\cos(\omega_0 t)+C_2\sin(\omega_0 t) \quad \text{with;} \quad \omega_0=\sqrt{\frac{k}{m}}$$

In order to find the total response of a system, the particular solution is required to be calculated by substituting the excitation force into the equation of motion. The particular solution has the same frequency as the excitation and therefore, the amplitude of its coefficients can be found by substituting the particular solution in the equation of motion. If a single harmonic force is considered the particular solution is in the form of:

$$x_{\text{part}}=\hat{x}_{\text{p}}\cos(\omega t+\theta)$$

The general solution is the sum of the general solution of the homogeneous equation and the particular solution:

$$x(t) = x_{\text{hom}}(t)+x_{\text{part}}(t)$$

In general, it can be concluded that the total vibration of a structure depends on the excitation force that is applied to the structure as well as the free vibration of the system imposed by the initial conditions which is also dependent on the properties of the structure. Therefore, understanding the relationship between vibration (also called response), modes (also called resonance) and the excitation in a structure is an important factor to propose a precise analysis of the dynamic behavior of the track.

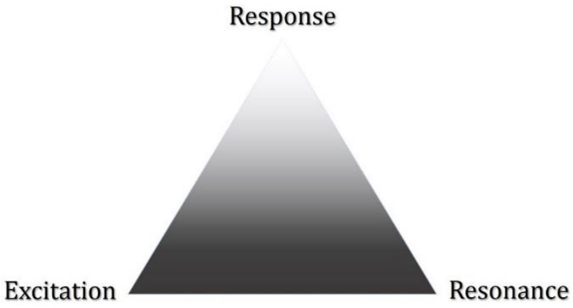

Figure 4-10 Relation between the vibration, resonance and excitation in a system

The figure 4-10 illustrates the triangle relationship between the total vibration (response) of a system, its modes (resonance) and the vibration due to the excitation applied on the system. As it was mentioned before, the total response of a system is determined by the sum of free vibration and the vibration due to the direct influence of the excitation force. As it was discussed above, the modes are dependent on the properties of the structure while the latter depends on the excitation force.

In order to analyze the dynamic relationships between response, resonance and excitation more carefully, time history of the results has to be converted into the frequency domain. This can be done using the Fourier transform technique where results in time domain are transformed into the frequency domain. In this research, Welch's technique is implemented to determine the power spectral density. This technique is based on the Fourier transform which convert the time domain results into the frequency domain by calculating the power of the spectrums in the frequency ranges.

Once the results in frequency domain are established, the comparison stage can be started. Therefore, the variation of the amplitudes of response, excitation and resonance can be collected in each specific frequency and the relationship between these variables can be established accordingly. For instance, if the amplitude of the excitation and free vibration were increased, it can be concluded that the total response of the structure is increased as well. On the other hand, the reduction in amplitude of the excitation and free vibrations will result in the reduction of the total response of the structure.

Table 4-1 Relationship between excitation, mode and response of a system

Condition	Excitation	Resonance	Response
1st condition	↓	+ ↓	= ↓ *
2nd condition	↓	+ ↑	= N/A
3rd condition	↑	+ ↓	= N/A
4th condition	↑	+ ↑	= ↑ *

* If resonance doesn't occur

The table 4-1 describes the relationship between the excitation, resonance and response of a system in same frequency ranges. According to this table, reduction in amplitude of excitation and resonance results in reducing of amplitude of the response. Similar trend can be seen for the increasing of these amplitudes. On the other hands, the increase in one of the amplitudes of excitation or resonance and reduction of the other one results in the magnitude of the response to be unpredictable unless its magnitude is measured.

It should once more be noted that the above relationship is valid when the comparison is conducted in the frequency domain. Moreover, the predictable magnitudes of the response have an important exception. If the frequency of the excitation force is occurred at the same frequency of the modes of a structure, the amplitude of its motion increase significantly, which is known as resonant frequency. Therefore, in the 4th condition where the amplitude of both excitation and resonance decreases, the magnitude of the response can be significantly increased if the specific frequency of excitation and resonance coincide.

4.2.3.1 100.F.576

According to figure 4-11 (a) and (b), the PSD of the excitation and response are decreased around the frequencies of 600Hz and 1kHz. As said by (Papaioannou, 2018), the amplitude of the rail (~600Hz) and pinned-pinned (~1kHz) resonances are decreased by reducing the 1st sleeper spacing after the IRJ. The figure 4-11 (a) illustrates a similar trend where the amplitude of the response of the track is reduced around these frequencies. On the other hand, the response is increased around the frequency of 3kHz. Since the excitation is not altered at this frequency, the arrangement of the sleeper spacing is believed to result in variation of resonance amplitude at the high-frequencies (~3kHz).

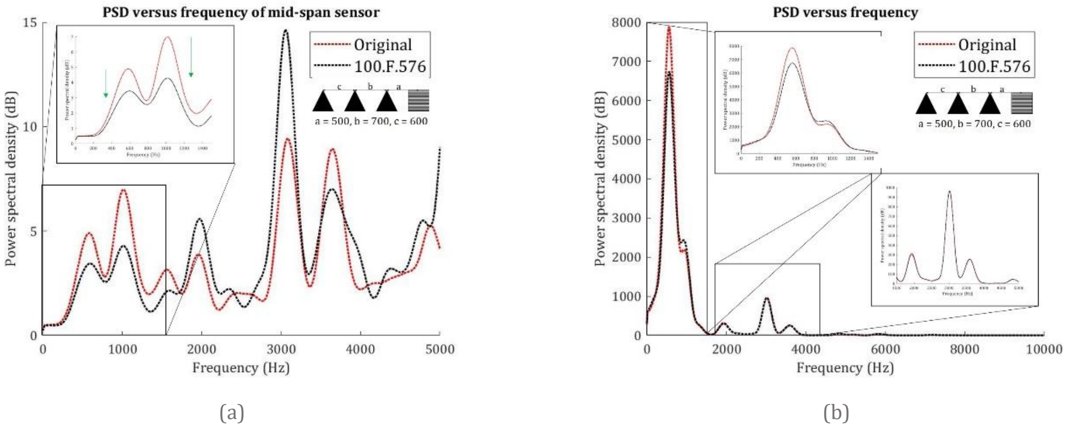

(a) (b)

Figure 4-11 (a) PSD of vertical acceleration; (b) PSD of contact force

4.2.3.2 100.B.576

According to figure 4-12 (b), the PSD of the excitation experiences a constant amplitude around the frequency of 1kHz and a minor increment around the frequencies of ~600Hz and 3kHz. The figure 4-12 (a) shows that the response is decreased significantly around the frequency of 1kHz while it is slightly increased around the frequency of 600Hz. It may be concluded that this arrangement had reduced the amplitude of the pinned-pinned resonance (~1kHz) while in the slight increase of the response at the frequency of 600Hz is due to the increment of PSD of excitation at this frequency. Around the frequency of 3kHz, the similar trend to the 100.F.576 can be observed where the amplitude of the response is increased at this frequency.

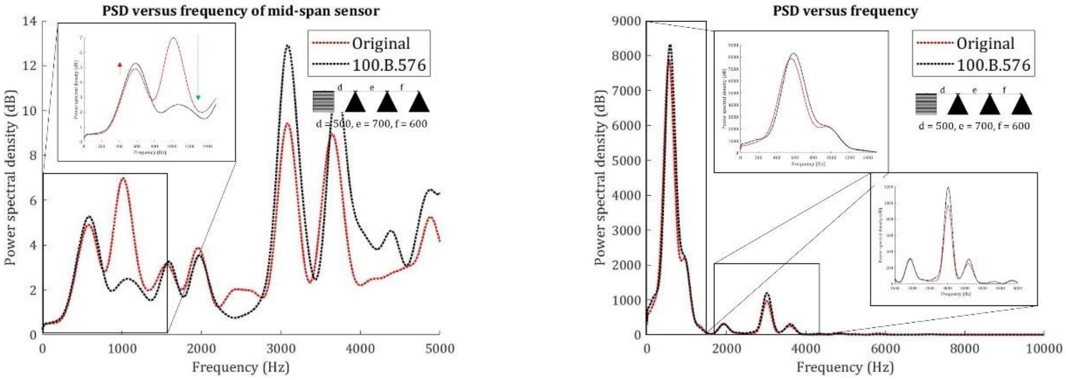

(a) (b)

Figure 4-12 (a) PSD of vertical acceleration; (b) PSD of contact force

4.2.3.3 100.F.756

According to (Papaioannou, 2018), increasing the sleeper spacing after the IRJ may results in the growing of the amplitude of rail resonance (~600Hz) and reduction of the amplitude of pinned-pinned resonance (~1kHz). As it is shown infigure 4-13 (b), this arrangement results in incrementation of the PSD of contact force around the frequency of 600Hz. The response of the track is increased around 600Hz and decreased significantly around the frequency of 1kHz which can be seen in figure 4-13 (a). This is believed to be in line with the founding of (Papaioannou, 2018) for this specific arrangement of sleeper spacing. On the other hand, the amplitude of the response is increased around the frequency of 3kHz.

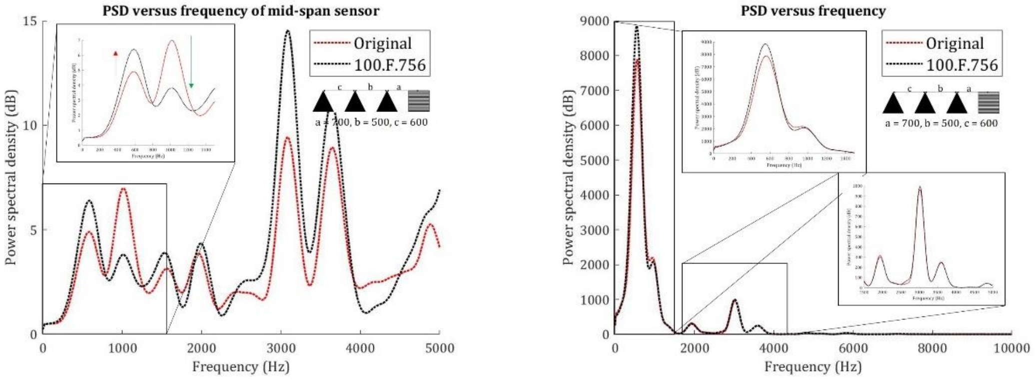

(a) (b)

Figure 4-13 (a) PSD of vertical acceleration; (b) PSD of contact force

4.2.3.4 100.F.444

Based on figure 4-14 (b), the PSD of excitation calculated from contact force around 600Hz is decreased similar to 100.F.576 while no variation is observed around other frequencies. Furthermore, the amplitude of the rail (~600Hz) and pinned-pinned (~1kHz) resonances are believed to be decreased when 1st sleeper spacing after the IRJ is reduced (Papaioannou, 2018). Since response of the track is defined as the sum of vibrations due to excitation and the resonance of the track, its amplitude in the frequencies around 600Hz and 1kHz are decreased accordingly.

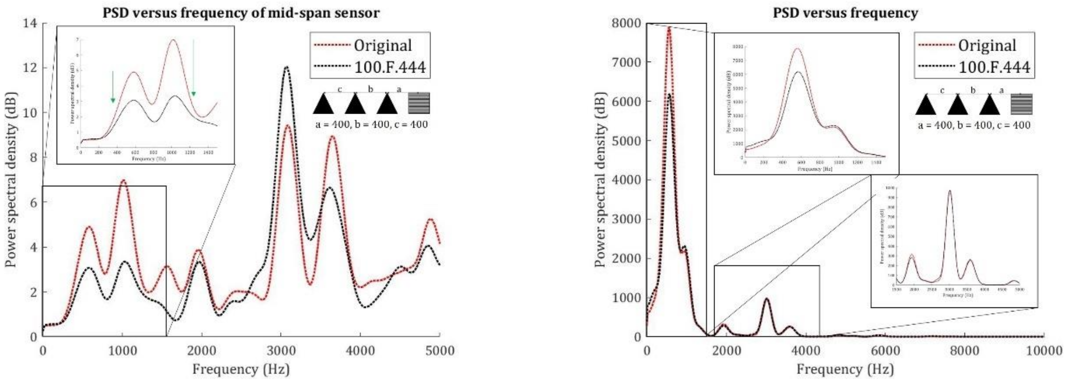

(a) (b)

Figure 4-14 (a) PSD of vertical acceleration; (b) PSD of contact force

4.2.3.5 100.F.345

Similar to the model 100.F.444, the amplitude of the PSD of excitation which is determined from the contact force is reduced significantly around the frequency of 600Hz. Since the amplitude of the rail (~600Hz) and pinned-pinned (~1kHz) resonances are decreased by the application of variant sleeper arrangement after the IRJ, the PSD of the response is affected accordingly. According to figure 4-15 (a), the PSD of the response proves this statement where the amplitude around the frequencies of 600Hz and 1kHz are decreased significantly. It should be mentioned that the PSD of response is amplified around the frequency of 3kHz.

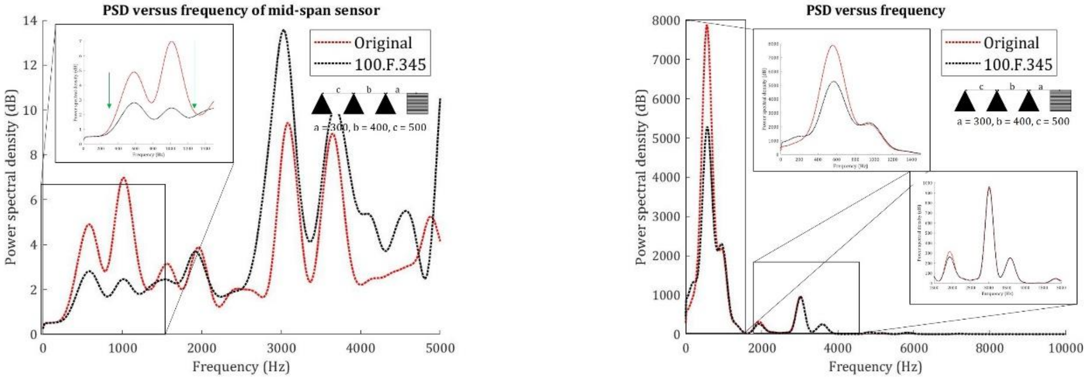

(a) (b)

Figure 4-15 (a) PSD of vertical acceleration; (b) PSD of contact force

4.2.3.6 100.B.345

According to figure 4-16 (b), the PSD of the excitation is decreased significantly around the frequency of 600Hz while the response around this frequency is increased. It can be said that altering the sleeper spacing before the IRJ results in ultimate incrementation of amplitude of rail resonance (~600Hz). It can be deduced that the increase of the amplitude of resonance around 600Hz overcome the reduction of excitation around the same frequency. Therefore, the response experienced an increase around the frequency of 600Hz. Besides, this arrangement resulted in amplification of response relative to the resonance around the frequency of 3kHz.

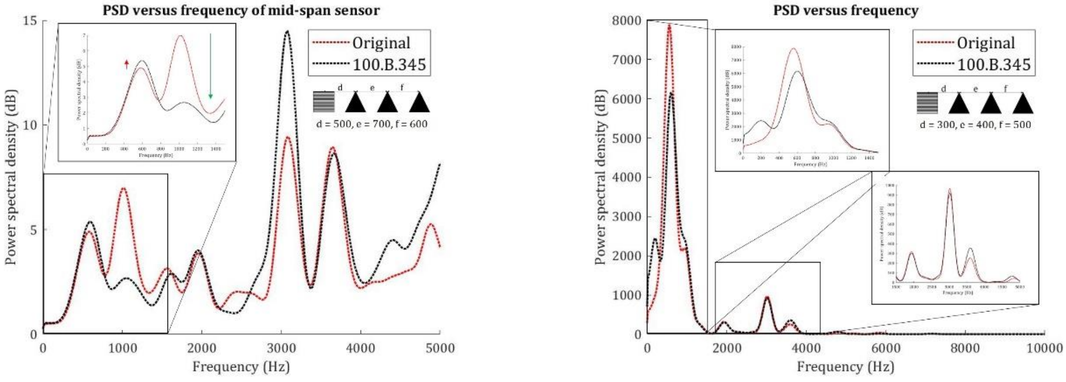

(a) (b)

Figure 4-16 (a) PSD of vertical acceleration; (b) PSD of contact force

4.2.3.7 Wavelet Power Spectrum (WPS)

The WPS of the impact vibration of submodels and the original model that is recorded using the part 18 can be seen in figure 4-17 (a) – (g). The unit of the color bar is m/s².

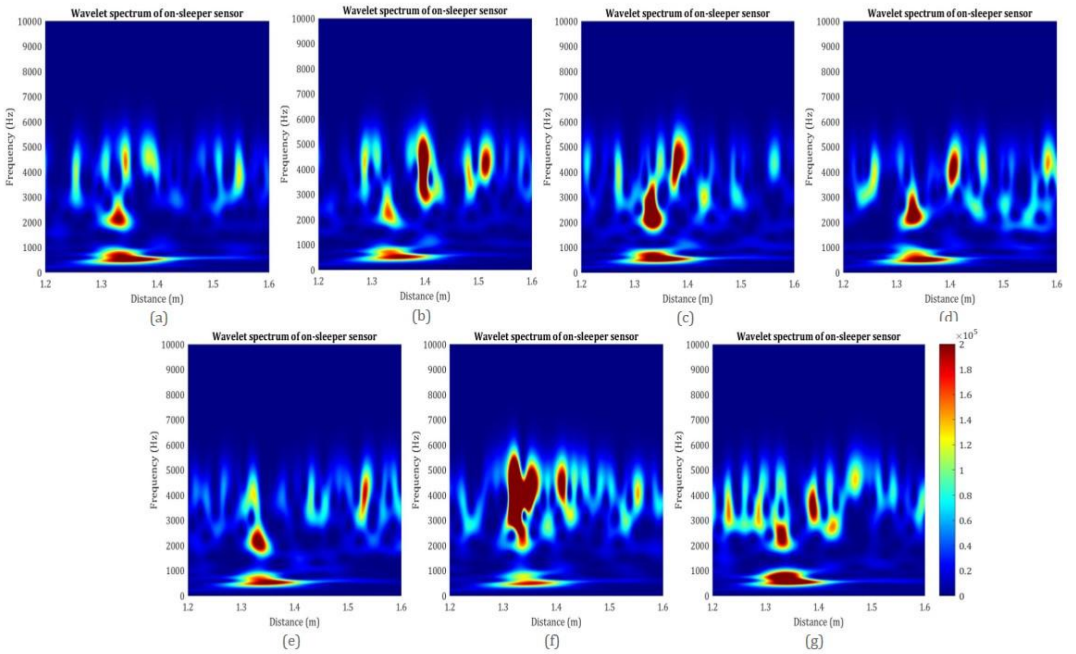

Figure 4-17 WPSs of the submodels and original impact vibration (upper row: (a) Original, (b) 100.F.576, (c) 100.B.576, (d) 100.F.756; lower row: (e) 100.F.444, (f) 100.F.345, (g) 100.B.345)

According to figure 4-17 (f), application of the non-uninform sleeper spacing after the IRJ may result in increasing of the high-frequency energy concentration which may result in significant increase of the noise. On the other hand, 100.F.345 showed the best improvement in reduction of the low- frequency energy concentration up to the frequency of 1kHz.

Generally, the implementation of the non-uniform sleeper spacing after the IRJ results in reduction of energy concentration in frequencies between 200Hz – 1kHz while this parameter increases when non-uniform sleeper spacing before the IRJ is applied. Moreover, implementation of uniform sleeper spacing in the original model results in the lowest energy concentration at frequencies around 3kHz.

4.3 Conclusion

As a conclusion of the parametric studies performed in this chapter, possible improvements in reduction of the impact force was observed from the results shown in this chapter. In the railway networks with dense railway traffic, such as the case in the Dutch railway network, significant impact forces are experienced by the track components due to the various axles of the trains. Therefore, it is believed that small reduction of the impact force can be considered as valuable improvement in reducing the degradation to the rail and IRJ components.

The submodel 100.F.345 which implemented a non-uniform sleeper spacing after the IRJ showed the best result in reduction of the first impact force. Since the wheel experience a jump after the first impact, it contacts the rail with a relative high impact force. The second impact force due to this phenomenon can be observed from the results shown in this chapter. The reduction of the sleeper spacing before the IRJ and implementation of variant sleeper arrangement after the IRJ showed the best results in terms of decreasing the second impact force.

From the perspective of vertical vibration, reduction of the magnitude was observed in three of the submodels where sleeper spacing after the IRJ was altered while the variation of sleeper spacing before the IRJ did not result in any improvement. Although the consistent sleeper spacing after IRJ can decrease the vertical vibration, a variant arrangement of sleepers which can be seen in the submodel 100.F.345, results in increment of this parameter significantly.

Throughout the frequency analysis, it was shown that implementation of non-uniform sleeper spacing after the IRJ can reduce the response of the track in low frequencies. This reduction includes the amplitude of the dominant frequencies around 600Hz and 1kHz where the rail and pinned-pinned resonances exist. According to the results show in this chapter, it can be deduced that reduction of the low-frequency vibration is due to the reduction of excitation and resonance at these frequencies. Therefore, it can be claimed that reduction of certain resonances due to the variation of sleeper spacing which was obtained by (Papaioannou, 2018) can effectively improve the dynamic interaction between wheel and rail by reducing the response at low frequencies. On the other hand, application of non-uniform sleeper spacing increases the high-frequency vibration significantly which is believed to be influenced by the amplitude of the resonance of the track.

5

Parametric Studies - Traffic Speed

In this chapter, a parametric study is conducted where various train speeds are simulated to assess the effects of the traffic speed on the performance of the track. The performance of IRJ, i.e. the magnitude of the impact force and track vibration. The analyses are performed in both the time and frequency domains.

5.1 Overview on the Models

5.1.1 Traffic Speed

In order to analyze the individual effect of the traffic speed on the dynamic behavior of the track, the new models were proposed with changing the speed of the wheel. Therefore, the arrangement of the sleepers is consistent between submodels and the original model while the speed of the pass-by wheel is altered. In this chapter the original model was used as the reference to conduct the comparison with the submodels. The speed of the wheel in original model is 100km/h and consequently this value was decreased and increased to determine the effects of traffic speed on the impact force and the vibration of the track.

Table 5-1 Overview on the traffic speed of the submodels

Model	Description
90.F.666	Wheel speed *decreased* to 90km/h
Original	Wheel speed = 100km/h
110.F.666	Wheel speed *increased* to 110km/h
120.F.666	Wheel speed *increased* to 120km/h
140.F.666	Wheel speed *increased* to 140 km/h
170.F.666	Wheel speed *increased* to 170 km/h
200.F.666	Wheel speed *increased* to 200 km/h

The wheel implemented in this model is considered to be a traction wheel. Therefore, the torque applied to the axles results in gradual increment in the speed. Consequently, the initial speed of the wheel is increased from t=0s to the end of the simulation time. This phenomenon is illustrated in figure 5-1.

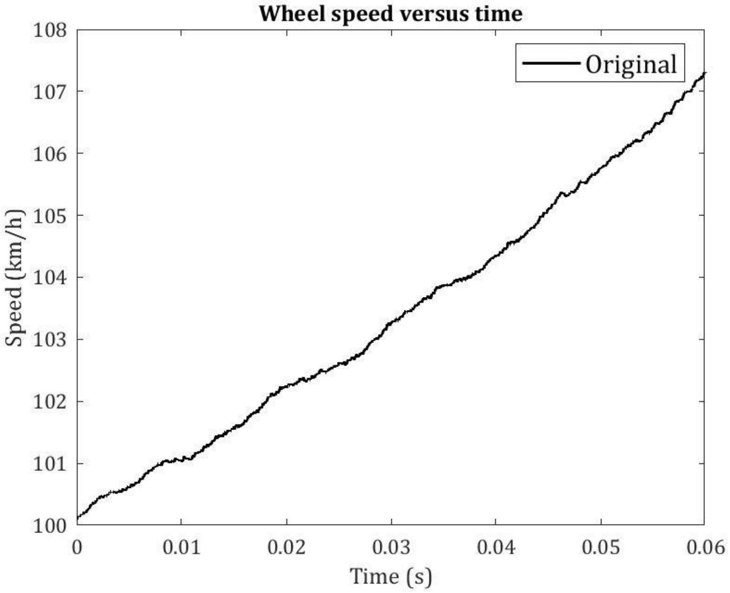

Figure 5-1 Increment in the wheel speed

5.2 Comparison Based on Traffic Speed Variation

In order to conduct the comparison between the submodels proposed in this chapter, similar tools and techniques that were used in the previous chapter had been implemented. Therefore, the PSD of the vertical acceleration and contact force was calculated using the *pwelch* function toolbox in MATLAB. Moreover, the WPS of the impact vibration and impact force was obtained to provide better insights on the effect of the traffic speed on the vibration of the track as well as the impact force at the insulated rail joint.

5.2.1 Results and Interpretation in Time Domain

5.2.1.1 Impact Force

Similar to the previous chapter, the impact force is obtained from the contact force between the wheel and rail by post-processing the data in RCFORC. Since, the dynamic relaxation from the start to the quasi-steady state rolling is required to be achieved, increasing the speed of the wheel results in larger dynamic effects and therefore it takes longer distance to achieve the relaxation. This difference can be seen in figure 5-2.

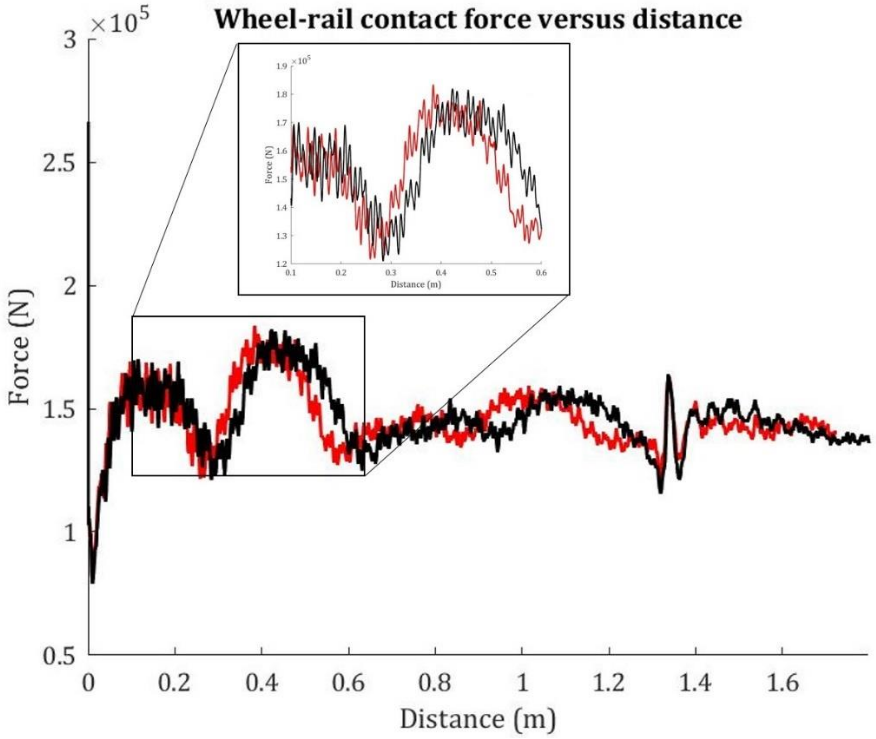

Figure 5-2 Difference between the contact force due to the deviated dynamic relaxation time

According to figure 5-3 (a) – (f), variation of the wheel speed can significantly alter the magnitude of the impact force. Figure 5-3 (a) shows that decreasing the speed of the wheel can reduce the magnitude of the impact force. On the other hand, increasing the wheel speed increase the impact force noticeably which can be seen in figure 5-3 (b) – (f).

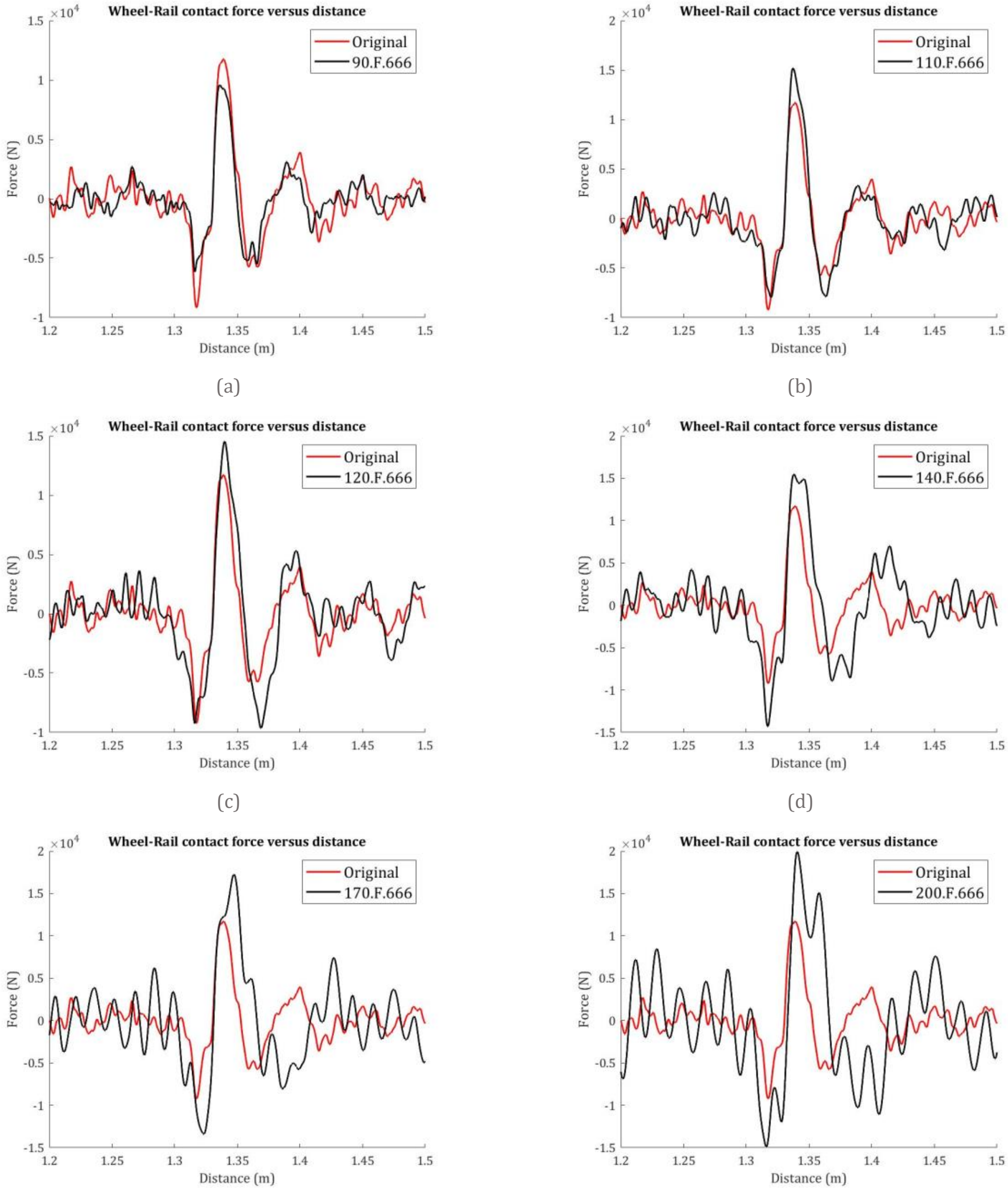

(a) (b)

(c) (d)

(e) (f)

Figure 5-3 The impact force of the submodels and original model

The magnitude of the first and second impact force are extracted and shown in figure 5-4 (a) and (b) respectively. As a general concept, the first impact force increases with the increase of the speed. However, it should be noted that the magnitude of the first impact force in the speed of 120km/h experiences a lower increase compared to the speed of 110km/h. This is considered as a plausible window for improvement in railway operation. The first impact force is significantly increased with increasing the speed in the submodels, 140.F.666, 170.F.666 and 200.F.666.

The second impact force is also influenced by the speed of the wheel except for the submodel with the speed of 110km/h where a negative variation of the second impact force relative to the original model with the speed 100km/h can be seen.

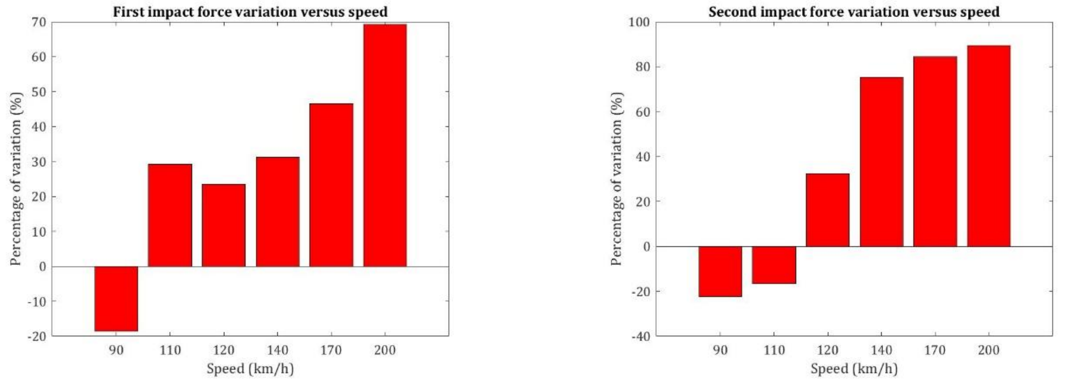

(a) (b)

Figure 5-4 Variation of impact force for the submodels w.r.t original model's speed (a) First impact force; (b) Second impact force

5.2.1.2 Vertical Vibration

The vibration of the original model and each submodel is shown in figure 5-5 (a) – (f). Generally, the speed utilized in these submodels did not result in any improvement in term of the vertical vibration. Nevertheless, the vibration for the velocity of 110km/h is not increased significantly. This may be considered as an improvement where the traffic speed is increased without changing the vertical vibration. On the other hand, the vibration is increased significantly for the speed of 120, 140, 170 and 200km/h. The effect of the high speed traffic on the impact vibration can be clearly seen based on figures (c) – (f). The impact resulted in high magnitude of the vibration at the distance of 1.347m.

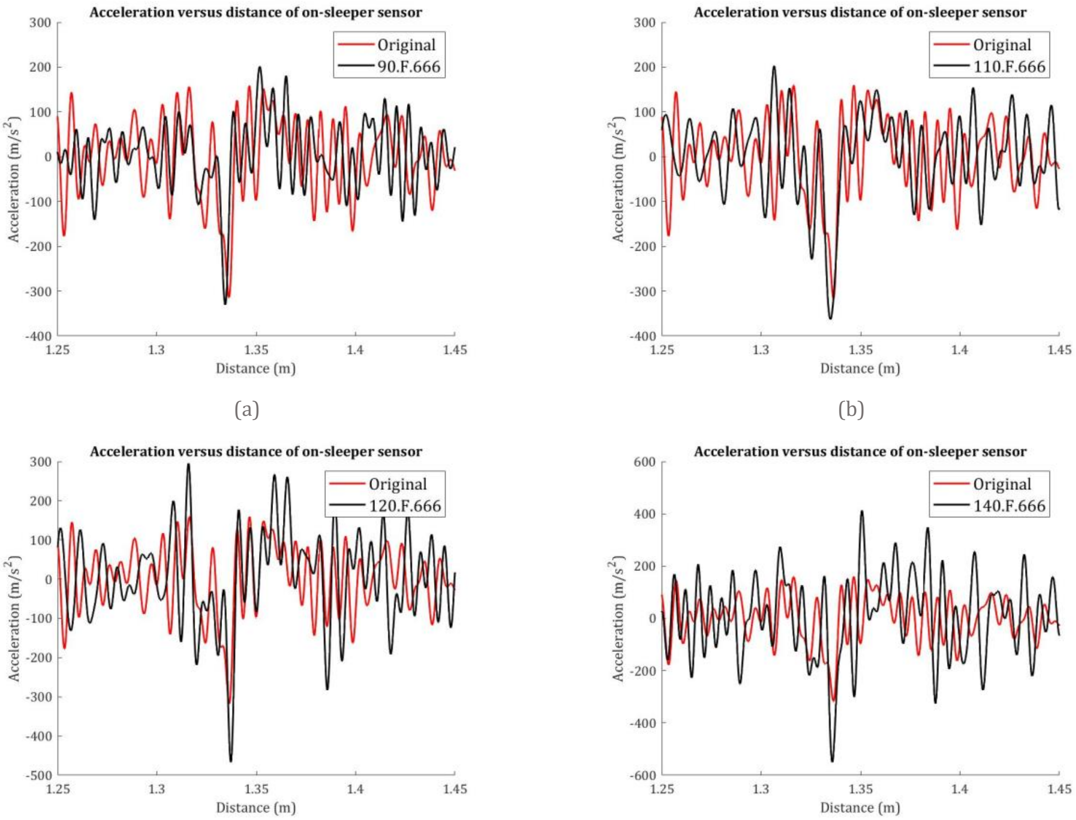

(a) (b)

(c) (d)

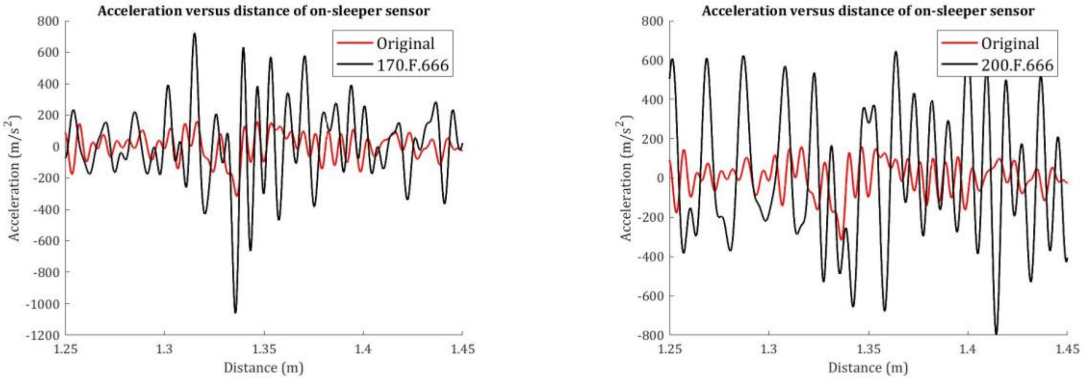

(e) (f)

Figure 5-5 The impact vibration of the submodels and original model - vertical acceleration

5.2.2 Results and Interpretation in Frequency Domain

As discussed in the previous chapter, to analyze the dynamic relationships between response, resonance and excitation more carefully, the time history of the vibration and contact force is converted into the frequency domain. This is believed to provide a better understanding of the effects of the traffic speed on the dynamic interaction between wheel and rail.

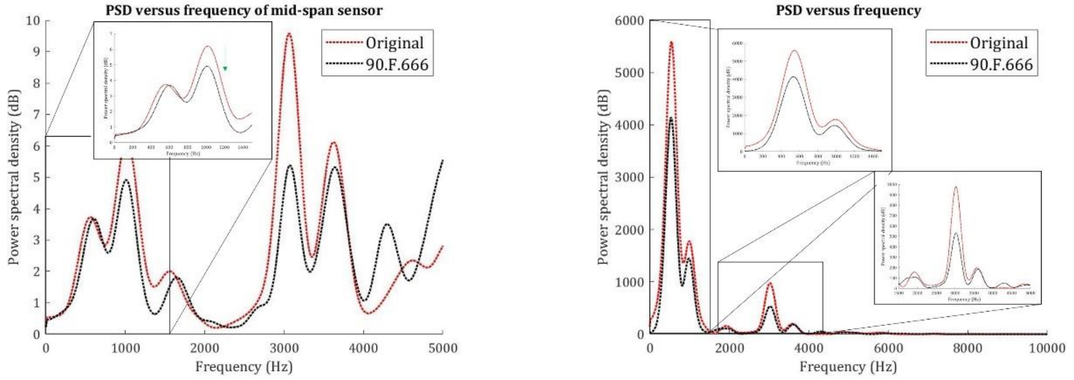

(a) (b)

Figure 5-6 (a) PSD of vertical acceleration; (b) PSD of contact force

According to figure 5-6 (b), the amplitude of the PSD of excitation in the frequencies of 600Hz, 1kHz and 3kHz is decreased with reduction of the speed to 90km/h. Moreover, figure 5-6 (a) shows that the PSD of the vertical acceleration of the track is decreased in the frequencies of 1kHz and 3kHz.

Based on figure 5-7 (b), the PSD of the excitation is increased significantly around the frequencies of 600Hz and 3kHz as the result of increasing the speed to 110km/h. The response around these frequencies are increased accordingly. The similar trend can be observed in figure 5-8 where the speed of 120km/h is implemented. Therefore, the effects of varying the speed of the traffic on the response can be clearly seen from figure 5-7 (a) and 5-8 (a).

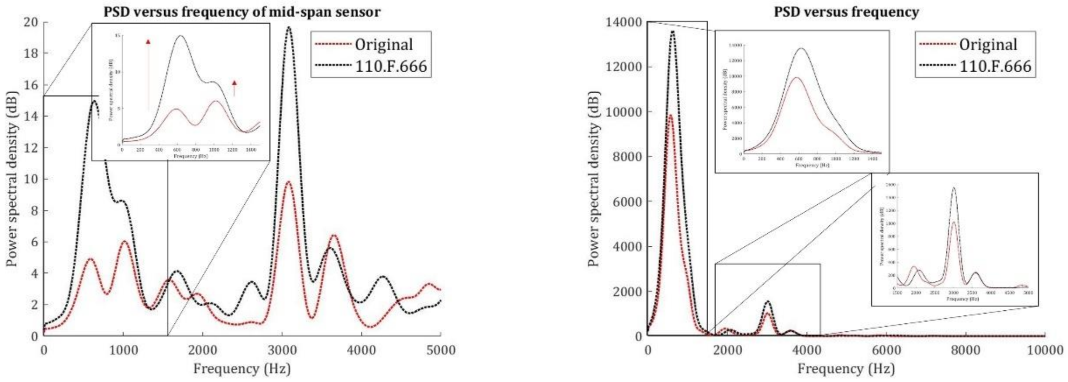

(a) (b)

Figure 5-7 (a) PSD of vertical acceleration; (b) PSD of contact force

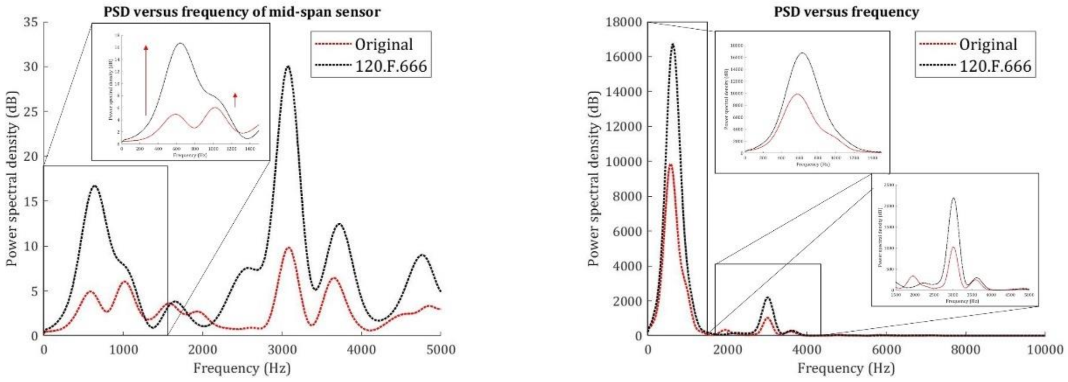

(a) (b)

Figure 5-8 (a) PSD of vertical acceleration; (b) PSD of contact force

According to figure 5-9 (b) and 5-10 (b) increasing the speed to 140 and 170km/h results in noticeable upsurge of the PSD of excitation around 600Hz and 3kHz. Accordingly, the PSD of the response experienced a noticeable increment within these frequencies. As can be seen in figure 5-10 (b), high-frequency excitation (~3kHz) is ultimately influenced by the application of high speed traffic. Besides, it is fair to say that the effect of traffic speed on the high-frequency excitation is noticeably more than the excitation in lower frequencies. Subsquently, the response is extremely influenced by the amplification of the PSD of excitation based on figure 5-10 (a).

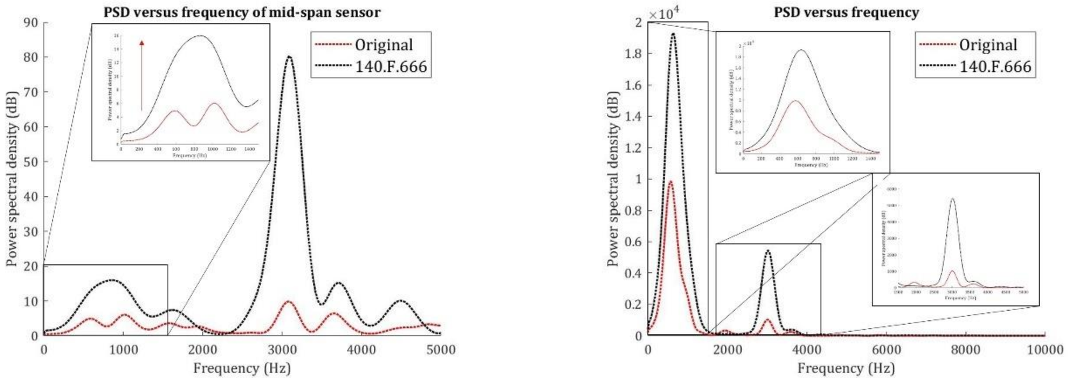

(a) (b)

Figure 5-9 (a) PSD of vertical acceleration; (b) PSD of contact force

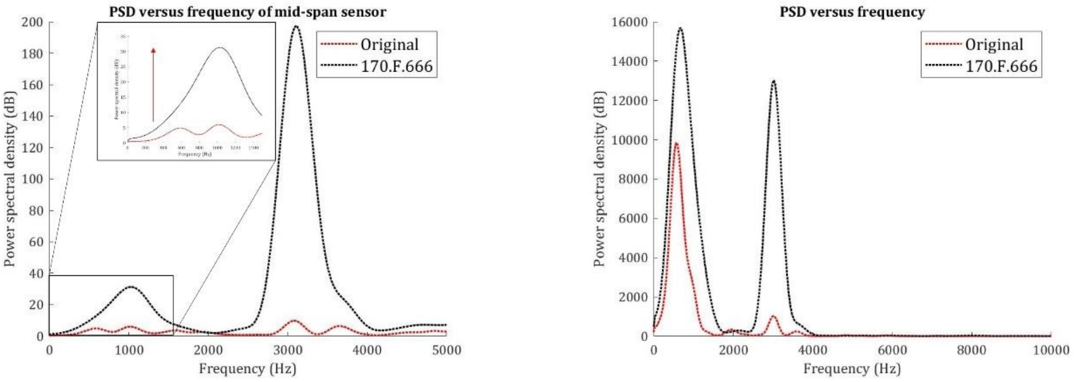

(a) (b)

Figure 5-10 (a) PSD of vertical acceleration; (b) PSD of contact force

Based on figure 5-11 (b), increasing the speed to 200km/h results in significant increase in the PSD of the excitation in the frequencies around 600Hz and 3kHz. The effect of this prominent increase can be clearly seen on the PSD of the response in figure 5-11 (a). It can be concluded that speed of 200km/h has ultimate effects on the high-frequency excitation and response.

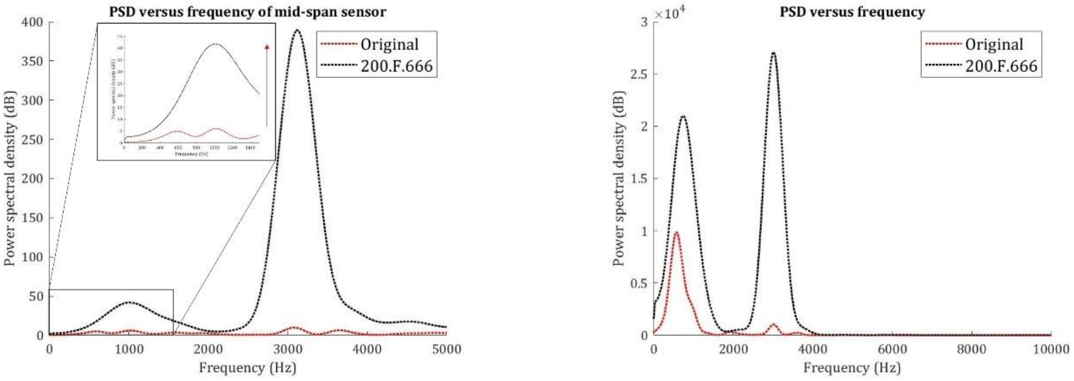

(a) (b)

Figure 5-11 (a) PSD of vertical acceleration; (b) PSD of contact force

5.2.2.1 Wavelet Power Spectrum (WPS)

In order to have better understanding of the dynamic response of the track, the WPS of the impact vibration is illustrated in figure 5-12 (a) – (g). The unit of the color bar is m/s^2. Generally, the increase of the speed results in the amplification of the vibrations within the frequency higher than 1kHz. Besides, the increment in the energy concentration more than the frequencies of 3kHz is higher than the broadband 200Hz – 1kHz. Moreover, figure 5-12 (a) demonstrates that decreasing the speed cause the reduction of the energy concentration in all range of frequencies.

The figure 5-12 (f) and (g) shows a prominent high-frequency energy concentration for the submodels with the speed of 170km/h and 200km/h respectively. Moreover, the ultimate increase of the vibrations between the frequencies of 200Hz and 1kHz within the distance of 1.2m to 1.5m can be clearly seen in these two cases.

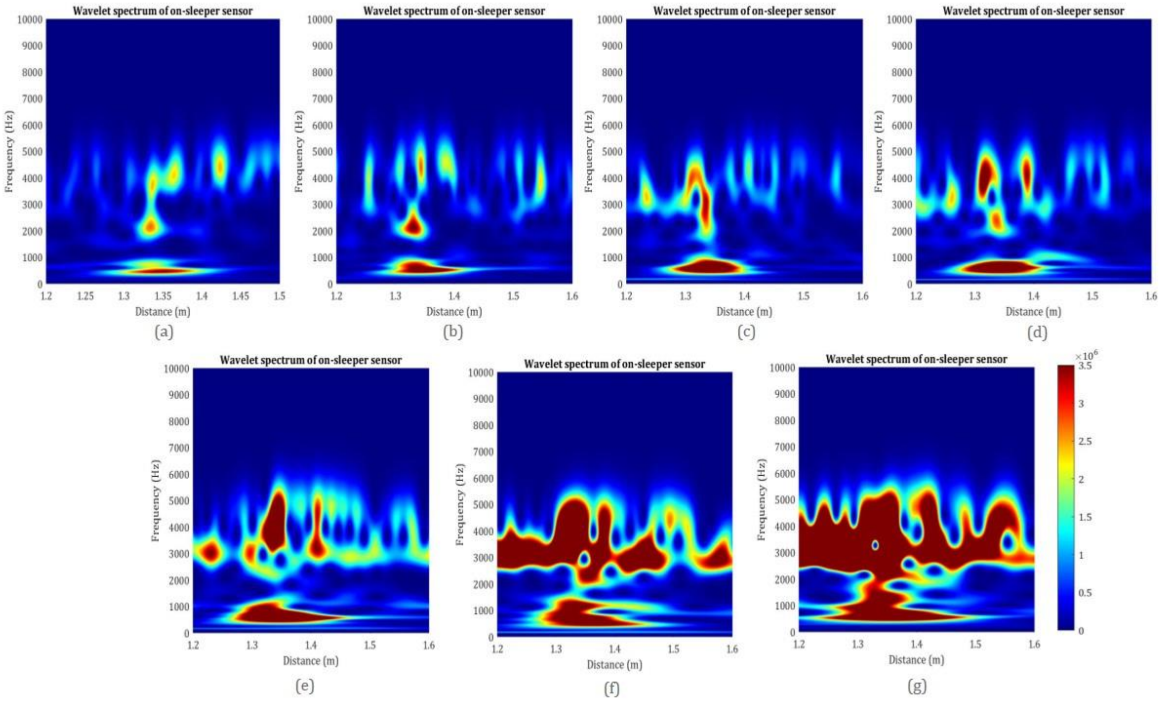

Figure 5-12 WPSs of the submodel and original impact vibration (upper row: (a) 90.F.666, (b) Original, (c) 110.F.666, (d) 120.F.666; lower row: (e) 140.F.666, (f) 170.F.666, (g) 200.F.666)

5.3 Conclusion

As a general concept, it can be concluded that the impact force is influenced by the speed of the traffic. Accordingly, the impact force upsurges with the increasing of the speed. The effects of increasing the speed can be clearly seen on the impact force in the case of implementing the speed of 140km/h, 170km/h and 200km/h. By comparing the results with the original model, the increment of the first impact force at the speed of 120km/h is less than the submodel with the speed of 110km/h. This can be assumed as an interesting finding which illustrates the plausible improvements in reduction of the impact force while the traffic speed is increased.

Furthermore, it can be concluded that the vertical vibration is increased significantly with the increase of the speed. According to the obtained results, the vibration at the speed of 110km/h is less than the original model with the speed of 100km/h while this parameter is increased at the speed of 120km/h onwards.

According to the frequency analysis, increasing the speed results in the prominent energy concentration of the response in frequencies more than 3kHz. Besides, the amplitude of the track vibration at frequencies between 200Hz and 1kHz is increased by increasing the speed. It should be mentioned that the amplification of the vibration is more dominant for the frequencies more than 3kHz compare to the broadband 200Hz to 1kHz. Therefore, it can be concluded that the increase of the speed has more influence on the higher frequencies which results in the incrementation of the noise propagation.

6

Performance Optimization

In this chapter, a performance optimization is conducted where the combination of various types of non-uniform sleeper spacing and traffic speeds are comprehensively considered and assessed. The performance of the IRJs, i.e. the to the impact force, low and high-frequency vibrations contribute mainly to the track degradation, passenger comfort and noise radiation respectively. The design of experiment (DOE) is the statistical tool utilized to proceed with the performance optimization. The proposed optimized model is nominated in this chapter.

6.1 Overview on the Procedures

Optimization is defined as the means of acquiring best possible solution for a defined problem within specific constraints. The best solution is defined as the most cost effective and highest achievable performance which the losses are minimized. An optimization algorithm is a procedure which is performed iteratively by comparing several solutions to achieve an optimum solution. The optimization problems are formulated with recognizing the design variables and constraints. The variables are defined as the parameters which the design problem is highly sensitive to them. The constraints represent the range of the values that are assigned to the variables which are limited due to the certain resource limitations and physical phenomenon.

Design of experiment (DOE) is a systematic method to obtain the relationship between factors and the output of a process. The DOE includes two main design steps; screening design and optimization design. The screening design is the method of identifying the most sensitive factors which highly affect the process while the purpose of optimization design is to find the most optimum condition by considering the inputs of a system. The detailed information about the DOE can be found in the chapter 2. In this research, the optimization design is implemented to identify the most optimum performance of the wheel-rail interaction.

The performance of the wheel-rail interaction is evaluated by considering the magnitude of the impact force as well the impact vibration. The degradation of the track components, disturbance of the passenger comforts and generation of the noise are highly susceptible to occur at these locations (Oregui et al., 2015). The impact force and vibration in the time domain are determined at instance that the wheel hits the rail after the joint. Besides, the frequency analysis is required to obtain a better understanding of the low and high-frequency vibration since these two factors are believed to be the cause of the effects on passenger comfort and noise radiation (Thompson et al., n.d.). The wavelet power spectrum of the impact vibration is utilized to perform the comparison between the performance of submodels in range of frequencies. The relationship between the optimization factors, analysis types and criteria zones can be found in figure 6-1.

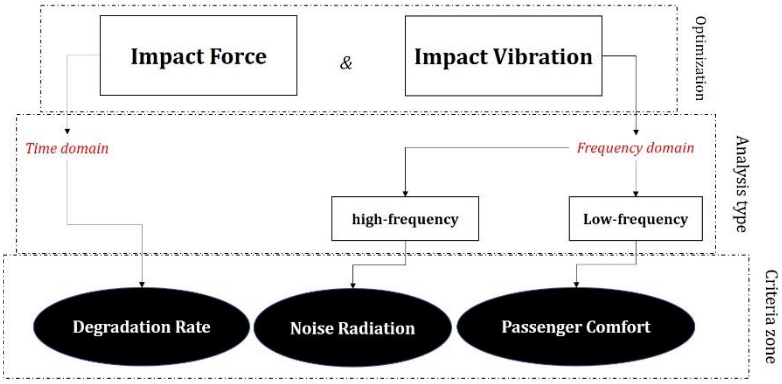

Figure 6-1 The relationship between optimization factors, criteria and analysis type

The sleeper spacing and the traffic speed are the two factors which are considered in the optimization process in this research. In chapter 4 and 5, the parametric studies had been performed on these two variables and valuable results were achieved. It is believed that the combination of these two factors can provide the opportunity for the operators and the infrastructure managers to synchronize the sleeper spacing with the speed of the trains to experience the lowest low-frequency and high-frequency vibrations as well as the impact force that can increase passenger comfort and reduce noise generation as well as the maintenance requirements respectively.

According to the findings in chapter 4, it was concluded that the implementation of non-uniform sleeper spacing after the IRJ may improve the performance of the wheel-rail dynamic interaction. Besides, the implementation of variant 1st,2nd and 3rd sleeper spacing showed the highest improvement in terms of reduction of the impact force and low-frequency vibration. Moreover, the essence of providing a feasible design convinced this research to remove the 1st concrete sleeper after the IRJ and place two concrete sleepers between the timber and the next concrete sleeper. This arrangement which can be seen in figure 6-2 is believed to provide the chance for the infrastructure contractors to not manipulate the further sleepers which can reduce the costs.

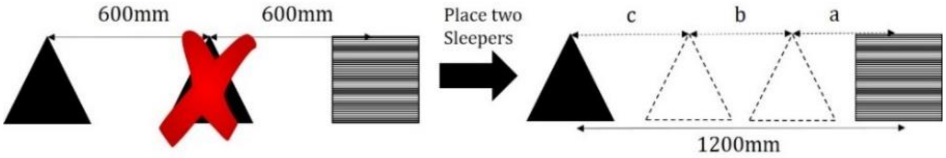

Figure 6-2 Overview on the arrangement of the concrete sleepers for optimization stage

With regard to the findings in the chapter 4, the lower and upper bounds for both 1st and 2nd sleeper spacings after the IRJ are defined as 300mm and 600mm respectively. The 3rd sleeper spacing is calculated by deducting the two first sleeper spacings (a and b) from 1200mm which is the distance between the timber sleeper and the first unremoved concrete sleeper. Due to the geometry of the concrete sleepers, certain limitation regarding the spacing exist. Subsequently, the sleeper spacing less than 300mm is not feasible to be achieved.

According to the chapter 5, the dynamic interaction between the wheel and rail is highly influenced by the increasing of the speed. Since the two typical trains that are operated on the Dutch railway network (sprinter and intercity trains) are considered in this research the speed of the traffic is limited to their operation speed which is 140km/h with the lower bound of 100km/h.

The optimization design in DOE implements several tools which were discussed in chapter 2. With regard to the properties and the techniques used in the central composite design (CCD), this tool is utilized to conduct the performance optimization in this research. The CCD design is studied at five levels by utilizing full two-level factorial design, a center point and an axial distance (α). Since the flexibility of the CCD depends on the selection of the axial distance and the central point, these factors are accounted as the important parameters in CCD design.

In order to propose the optimized model, the values within the lower and upper boundaries of the sleeper spacing and traffic speed are to be considered in this research. Therefore, the axial distance is fixed to a value lower than 1. The interaction between the variables by illustrating the factorial design, axial and central points can be seen in figure 6-3.

The value of 0.6 is employed for the axial distance. This value is recommended by the function toolbox *ccdesign* in MATLAB. Therefore, the five limits (-1, -0.6, 0, 0.6, 1) are utilized to construct the CCD subsequently.

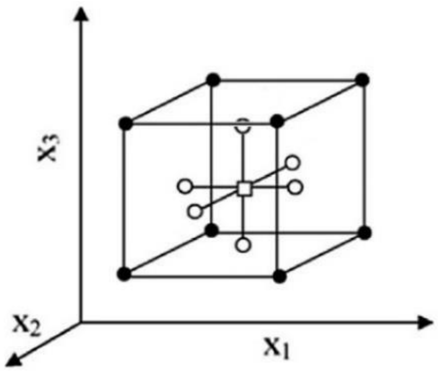

Figure 6-3 Central composite designs for the optimization of three variable. (•) Points of factorial design, (○) axial points, and (▭) central point

In order to increase the simplicity of determining the combination of the three chosen factors, the same toolbox in MATLAB is implemented. There are 15 combinations which the results are shown in figure 6-4.

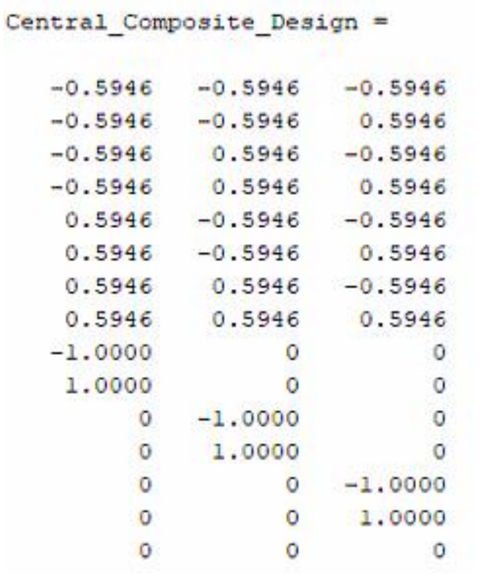

```
Central_Composite_Design =

   -0.5946   -0.5946   -0.5946
   -0.5946   -0.5946    0.5946
   -0.5946    0.5946   -0.5946
   -0.5946    0.5946    0.5946
    0.5946   -0.5946   -0.5946
    0.5946   -0.5946    0.5946
    0.5946    0.5946   -0.5946
    0.5946    0.5946    0.5946
   -1.0000         0         0
    1.0000         0         0
         0   -1.0000         0
         0    1.0000         0
         0         0   -1.0000
         0         0    1.0000
         0         0         0
```

Figure 6-4 Combination of the factors using CCD

The values of the 1st, 2nd sleeper spacing and traffic speed corresponding to the coefficients obtained from the central composite design in MATLAB is illustrated in figure 6-5 (a) and (b).

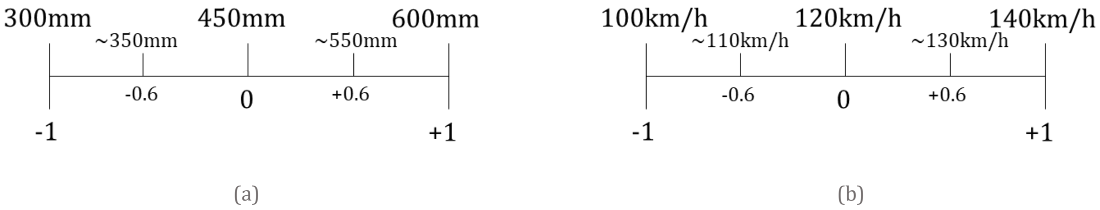

Figure 6-5 The values corresponding to the coefficients (a) 1st and 2nd sleeper spacing; (b) traffic speed

Therefore, the combinations of the 1st, 2nd sleeper spacing and the traffic speed with respect to figure 6-4 is shown in the table 6-1.

Table 6-1 Combination of the 3 factors for performance check

Submodel	Speed (km/h)	1st sleeper spacing (mm)	2nd sleeper spacing (mm)
1	110	350	350
2	110	350	550
3	110	550	350
4	110	550	550
5	130	350	350
6	130	350	550
7	130	550	350
8	130	550	550
9	100	450	450
10	140	450	450
11	120	300	450
12	120	600	450
13	120	450	300
14	120	450	600
15	120	450	450

According to the procedure in the performance optimization shown in figure 6-6, the value of the 3rd sleeper spacing after the IRJ must be calculated by deducting the sum of the 1st and 2nd sleeper spacing from 1200mm. If this value is less than 300mm the combination will be rejected due to the limitation caused by the geometry of the concrete sleepers. Therefore, the case 4, 8, 12 and 14 are eliminated and 11 submodels are used to conduct the comparison between the performance of the proposed submodels and obtain the most optimized combination in terms of reducing the impact force as well as the low and high-frequency vibration of the track.

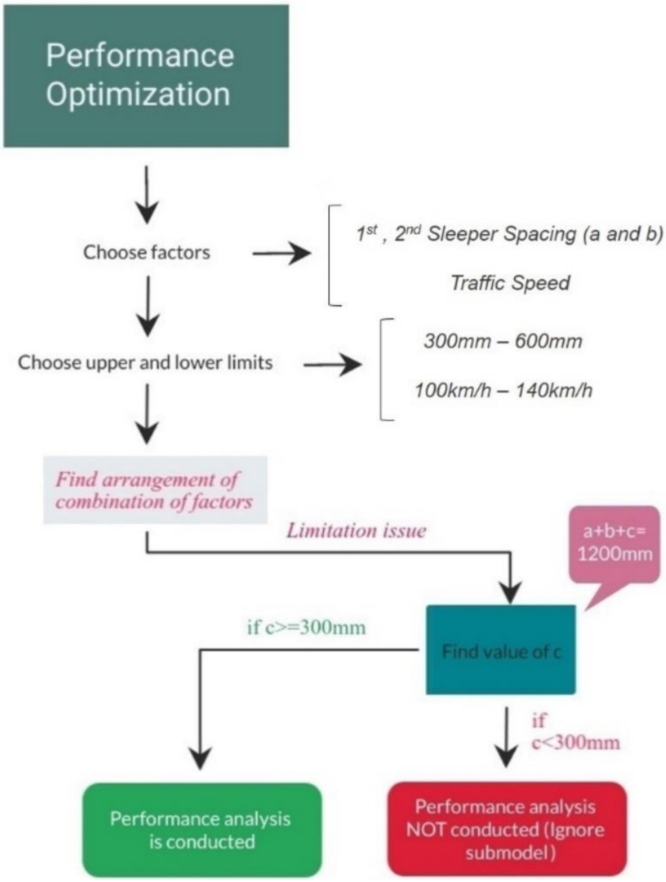

Figure 6-6 Flowchart of the performance optimization

As various submodels are proposed in this chapter, a specific representation pattern is used to let the readers simply understand the properties of each model. This pattern can be seen in figure 6-7.

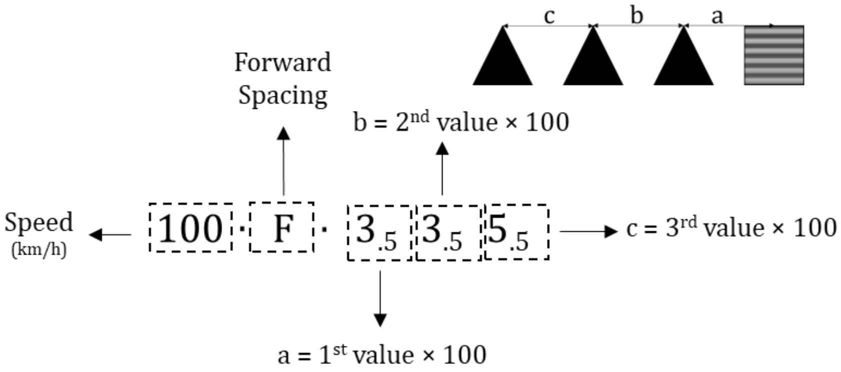

Figure 6-7 Representation pattern for submodels

Similar to the previous chapters, the original models are produced as a reference to conduct the comparisons with the proposed submodels. The uniform sleeper spacing is implemented for the original models. Besides, the speed of the wheel is 100, 110, 120, 130 and 140 km/h for the original models. The table 6-2 presents the list of the submodels which are produced to perform the comparison between these models.

Table 6-2 List of submodels

Model Nr.	Submodel	Model Nr.	Submodel
1	$100.F.4_{.5}4_{.5}3_{.0}$	7	$120.F.4_{.5}4_{.5}3_{.0}$
2	$110.F.3_{.5}3_{.5}5_{.0}$	8	$130.F.3_{.5}3_{.5}5_{.0}$
3	$110.F.3_{.5}5_{.5}3_{.0}$	9	$130.F.3_{.5}5_{.5}3_{.0}$
4	$110.F.5_{.5}3_{.5}3_{.0}$	10	$130.F.5_{.5}3_{.5}3_{.0}$
5	$120.F.3_{.0}4_{.5}4_{.5}$	11	$140.F.4_{.5}4_{.5}3_{.0}$
6	$120.F.4_{.5}3_{.0}4_{.5}$		

6.2 Results and Interpretation

6.2.1 Impact Force

The peaks shown in figure 6-8 (a) – (k) are defined at the position where the wheel hit the rail after the joint. This impact results in a high magnitude of the contact force which is called impact force. The impact force is obtained from the contact force between the wheel and rail by post-processing the data in RCFORC. The impact force of each submodel and the original model with identical speed but uniform spacing of 600mm for 1st, 2nd and 3rd sleeper spacing is illustrated in figure 6-8 (a) – (k).

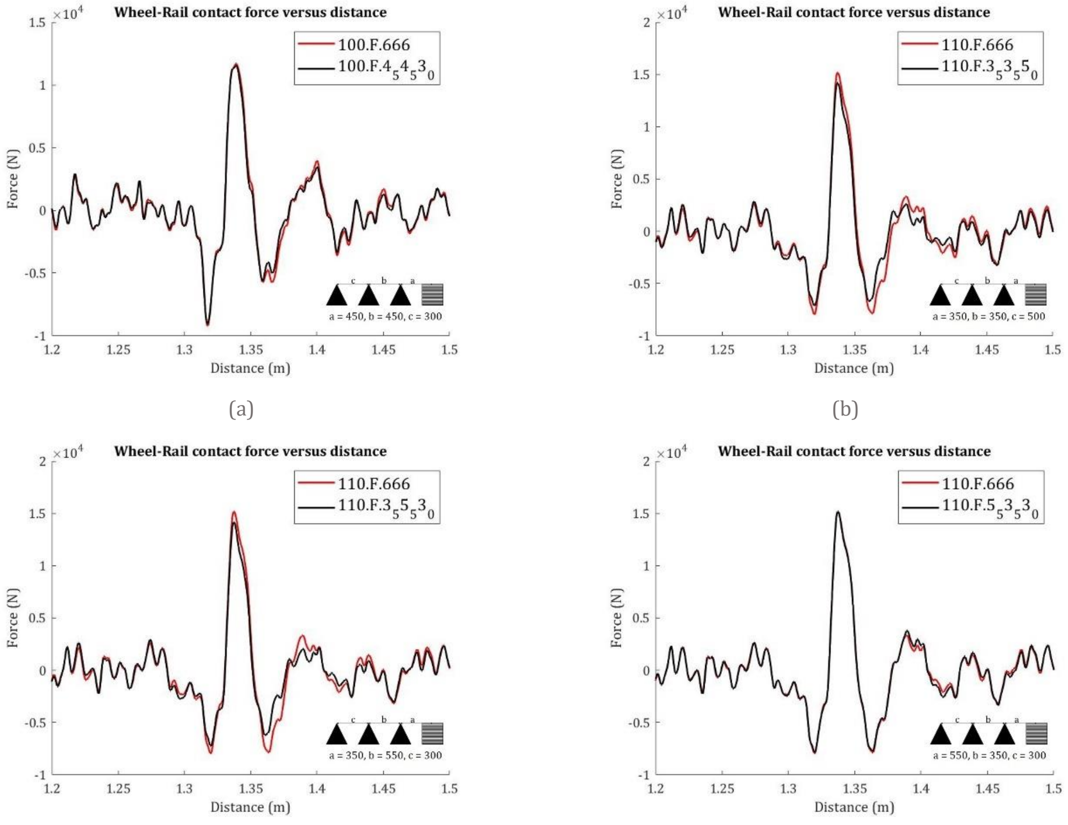

(a) (b)

(c) (d)

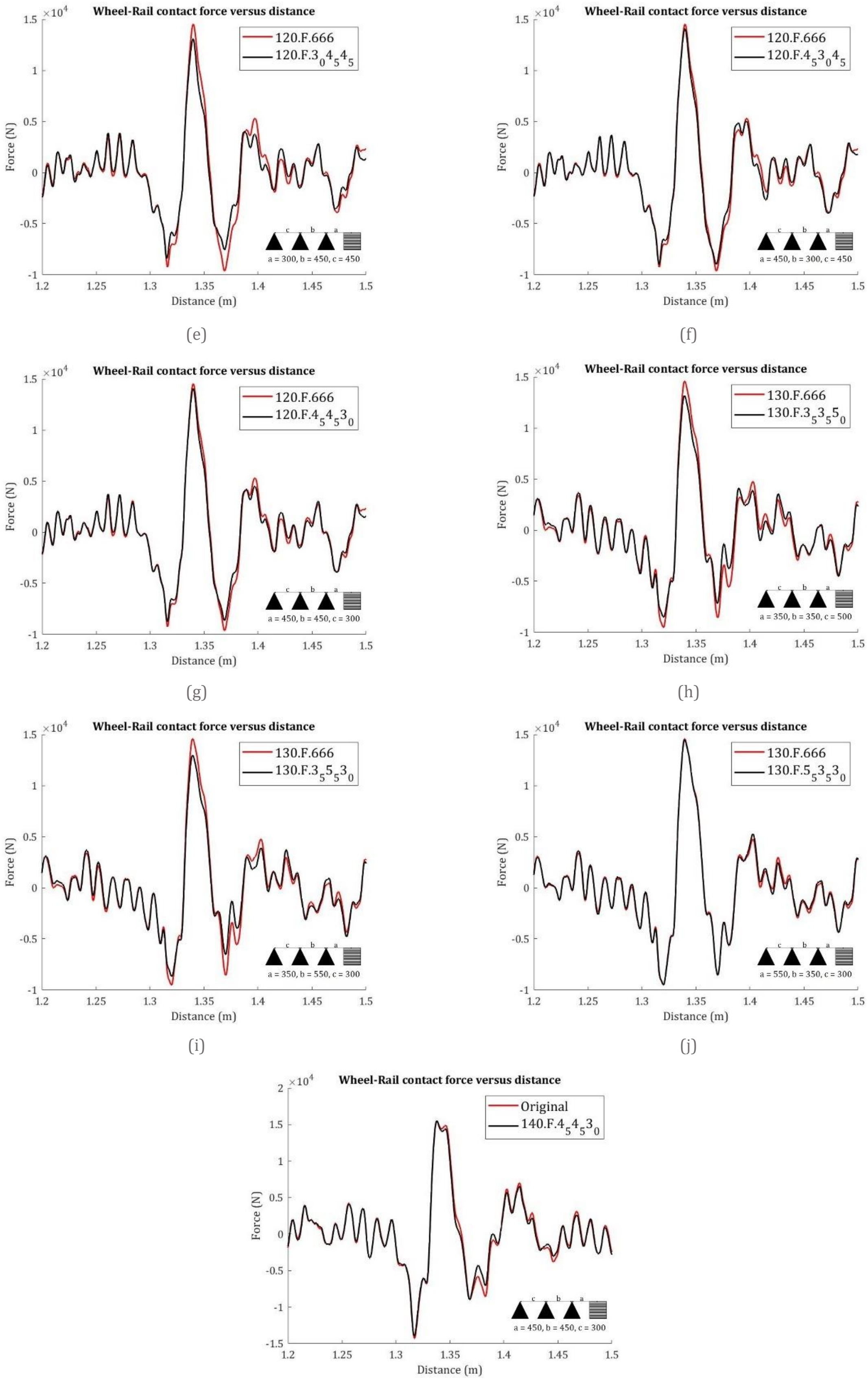

(e) (f)

(g) (h)

(i) (j)

(k)

Figure 6-8 The impact force of submodels and original models

The amplitude and the variation of the impact force of the submodels with respect to the original models are shown in figure 6-9 (a) and (b). According to figure 6-9 (a), the submodel $100.4_{.5}4_{-5}3_{.0}$ obtained the lowest impact force followed by the speed of 130km/h and 120km/h in the $130.3_{.5}5_{.5}3_{.0}$ and $120.3_{.0}4_{.5}4_{.5}$ respectively.

By comparing the variation of impact force in the proposed submodels, plausible improvements can be observed except in the case of $110.5_{.5}3_{5}3_{0}$. According to figure 6-7 (b), application of non-uniform sleeper spacing in the speed of 120, 130 and 140km/h has impressive effects on reduction of impact force.

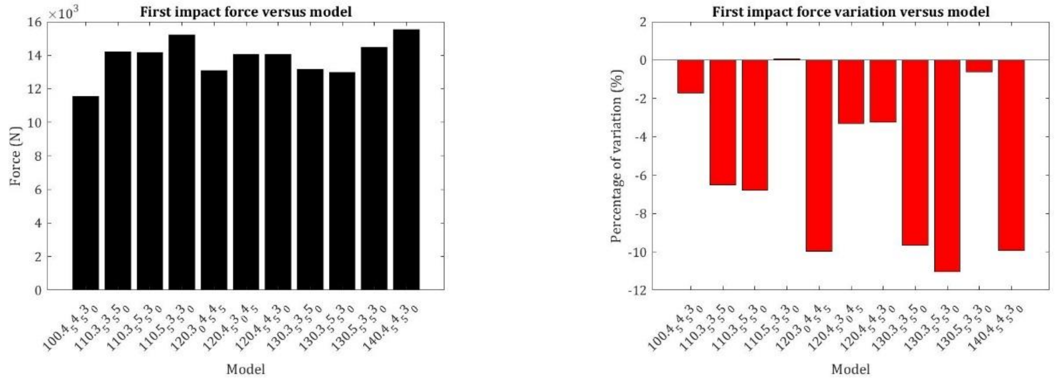

(a) (b)

Figure 6-9 First impact force for the submodels (a) First impact force values; (b) Variation w.r.t original model

6.2.2 Vertical Vibration

The magnitude of the impact vibration of each submodel and the original models with identical speed but uniform spacing of 600mm for 1st, 2nd and 3rd sleeper spacing is shown in figure 6-10 (a) – (k). The high peak of vibration can be seen at the distance of 1.347m where the impact occurs.

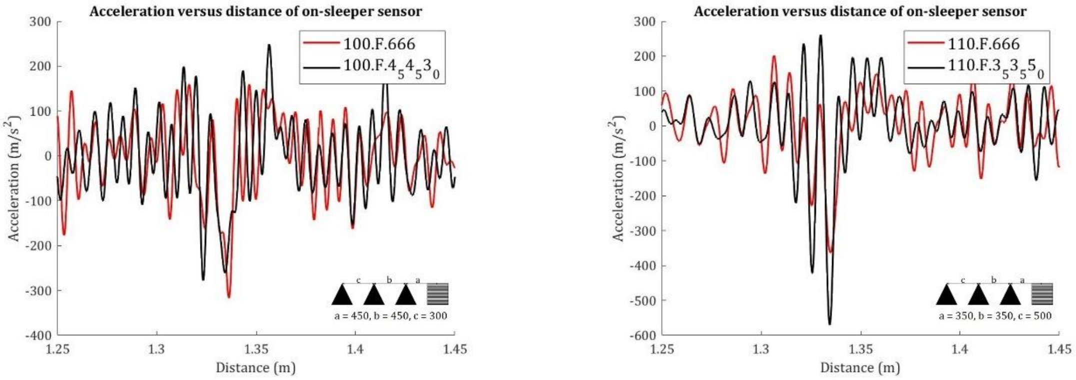

(a) (b)

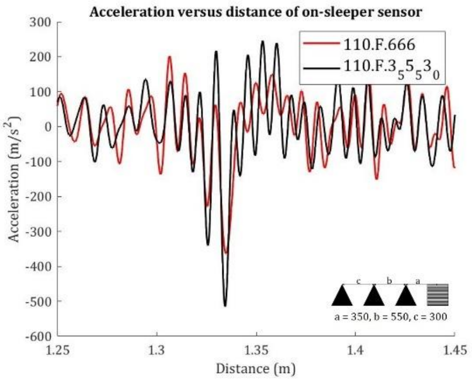
Acceleration versus distance of on-sleeper sensor
110.F.666
$110.F.3_5 5_5 3_0$
Acceleration (m/s^2)
Distance (m)
300
200
100
0
-100
-200
-300
-400
-500
-600
1.25
1.3
1.35
1.4
1.45
c
b
a
a = 350, b = 550, c = 300

(c)

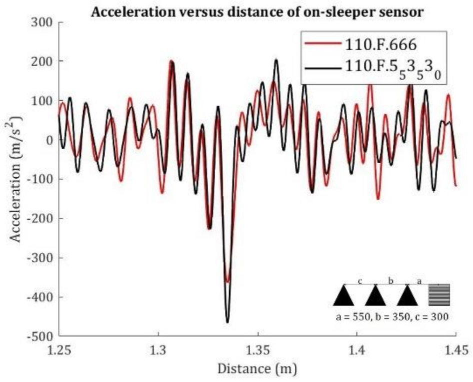
Acceleration versus distance of on-sleeper sensor
110.F.666
$110.F.5_5 3_5 3_0$
Acceleration (m/s^2)
Distance (m)
300
200
100
0
-100
-200
-300
-400
-500
1.25
1.3
1.35
1.4
1.45
c
b
a
a = 550, b = 350, c = 300

(d)

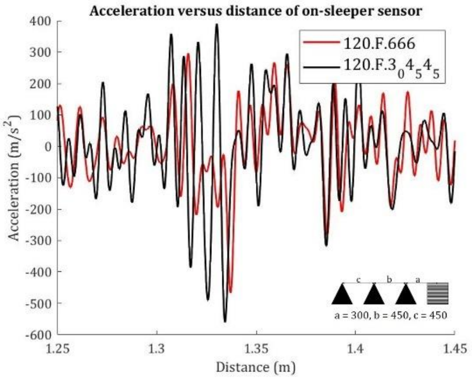
Acceleration versus distance of on-sleeper sensor
120.F.666
$120.F.3_0 4_5 4_5$
Acceleration (m/s^2)
Distance (m)
400
300
200
100
0
-100
-200
-300
-400
-500
-600
1.25
1.3
1.35
1.4
1.45
c
b
a
a = 300, b = 450, c = 450

(e)

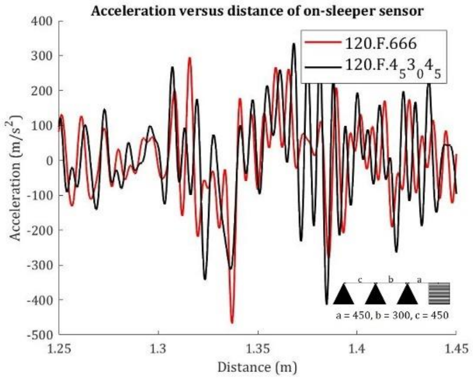
Acceleration versus distance of on-sleeper sensor
120.F.666
$120.F.4_5 3_0 4_5$
Acceleration (m/s^2)
Distance (m)
400
300
200
100
0
-100
-200
-300
-400
-500
1.25
1.3
1.35
1.4
1.45
c
b
a
a = 450, b = 300, c = 450

(f)

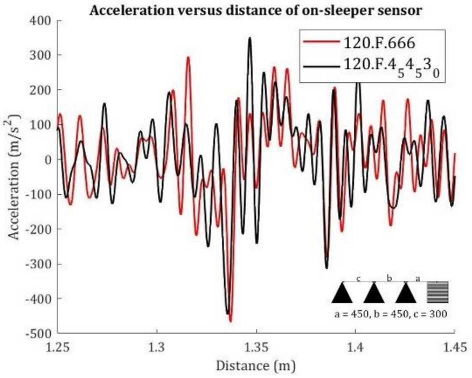
Acceleration versus distance of on-sleeper sensor
120.F.666
$120.F.4_5 4_5 3_0$
Acceleration (m/s^2)
Distance (m)
400
300
200
100
0
-100
-200
-300
-400
-500
1.25
1.3
1.35
1.4
1.45
c
b
a
a = 450, b = 450, c = 300

(g)

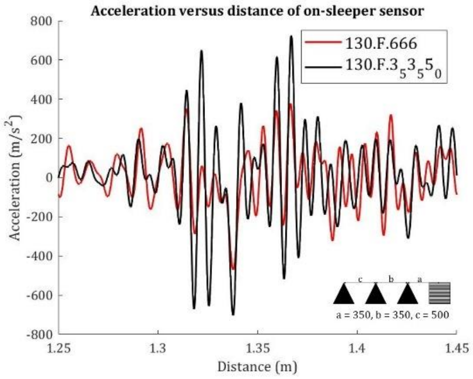
Acceleration versus distance of on-sleeper sensor
130.F.666
$130.F.3_5 3_5 5_0$
Acceleration (m/s^2)
Distance (m)
800
600
400
200
0
-200
-400
-600
-800
1.25
1.3
1.35
1.4
1.45
c
b
a
a = 350, b = 350, c = 500

(h)

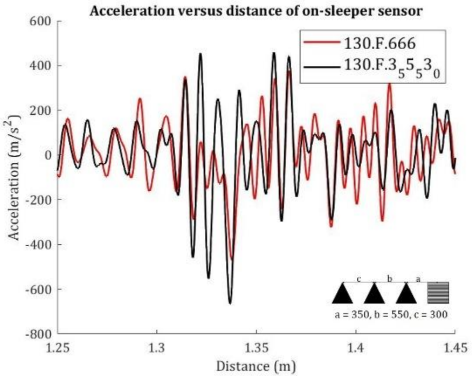
Acceleration versus distance of on-sleeper sensor
130.F.666
$130.F.3_5 5_5 3_0$
Acceleration (m/s^2)
Distance (m)
600
400
200
0
-200
-400
-600
-800
1.25
1.3
1.35
1.4
1.45
c
b
a
a = 350, b = 550, c = 300

(i)

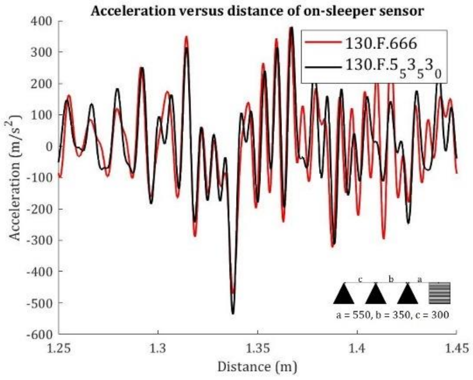
Acceleration versus distance of on-sleeper sensor
130.F.666
$130.F.5_5 3_5 3_0$
Acceleration (m/s^2)
Distance (m)
400
300
200
100
0
-100
-200
-300
-400
-500
-600
1.25
1.3
1.35
1.4
1.45
c
b
a
a = 550, b = 350, c = 300

(j)

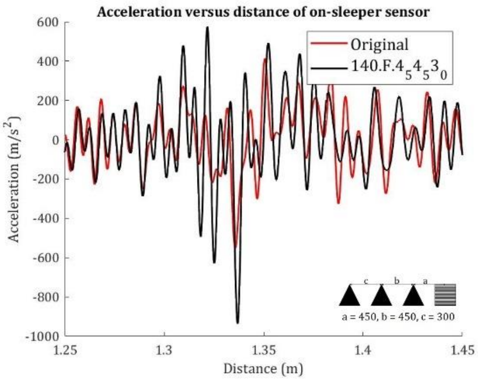

(k)

Figure 6-10 The impact vibration of submodels and original models - vertical acceleration

According to (de man, 2002), the passenger comfort is influenced by the low-frequency vibrations. Besides, (Pradhan et al., 2017) claimed that the passenger comfort is significantly affected by the vibration transmission in low frequencies between 0.5 – 100Hz. Accordingly, the low-frequency band-pass is implemented to filter the vertical vibrations. The amplitude and the variation of the low-frequency vibration of the submodels with respect to the original models with identical speed are shown in figure 6-11 (a) and (b). Based o figure 6-11 (a), the $100.F.4_{.5}4_{.5}3_{.0}$ has the lowest low-frequency vibration compare to other submodels. According to figure 6-11 (b), non-uniform sleeper spacing resulted in reduction of the low-frequency vibrations in majority of the submodels. The submodel $100.F.4_{.5}4_{.5}3_{.0}$ experienced the highest reduction of the low-frequency vibration while the results show a noticeable increment of this parameter in the $120.F.4_{.5}3_{.0}4_{.5}$.

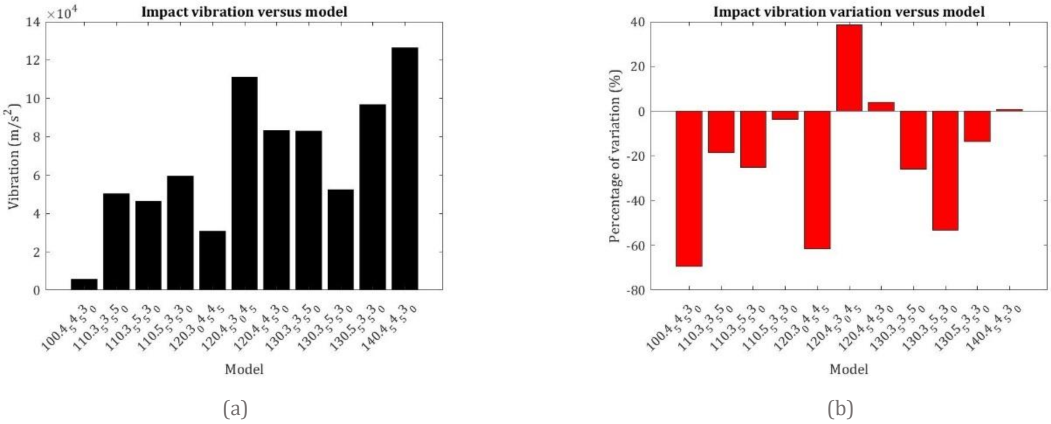

(a) (b)

Figure 6-11 Impact vibration of the submodels (a) Impact vibration values; (b) Variation w.r.t original model

In order to have better understanding of the dynamic response of the track, the WPS of the impact vibration is illustrated in figure 6-12 (a) – (l). The unit of the color bar is m/s^2. The WPS of the original models; 100.F.666, 110.F.666, 120.F.666, 130.F.666 and 140.F.666 can be seen in figures (a), (c), (g), (k) and (o) respectively.

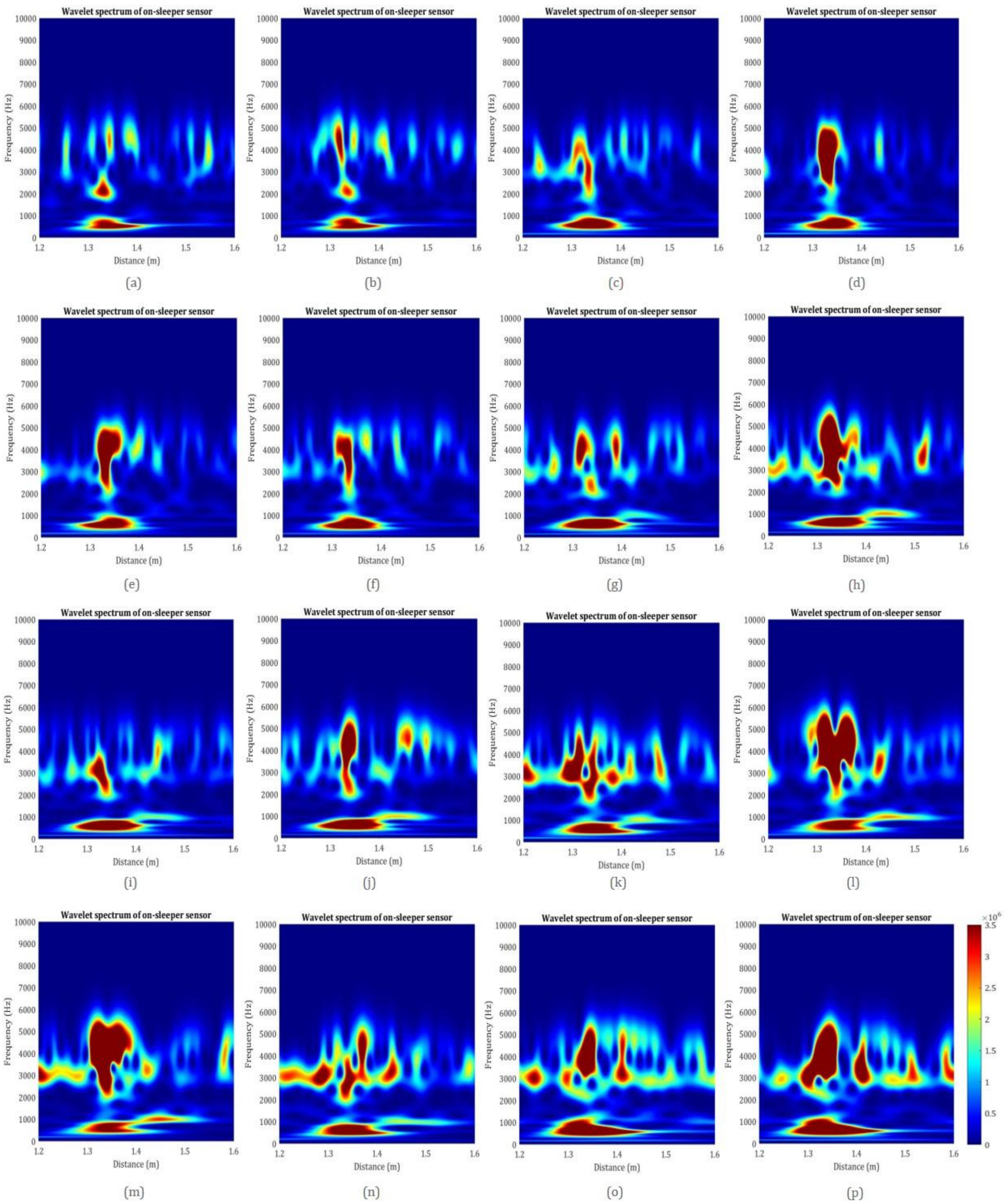

(a) (b) (c) (d)

(e) (f) (g) (h)

(i) (j) (k) (l)

(m) (n) (o) (p)

Figure 6-12 WPSs of the submodel and original impact vibration (first row: (a) 100.F.666, (b) 100.F.4$_{.5}$4$_{.5}$3$_{.0}$, (c) 110.F.666, (d) 110.F.3$_{.5}$3$_{.5}$5$_{.0}$; second row: (e) 110.F.3$_{.5}$5$_{.5}$3$_{.0}$, (f) 110.F.5$_{.5}$3$_{.5}$3$_{.0}$, (g) 120.F.666, (h) 120.F.3$_{.0}$4$_{.5}$4$_{.5}$; third row: (i) 120.F.4$_{.5}$3$_{0}$4$_{.5}$, (j) 120.F.4$_{.5}$4$_{.5}$3$_{.0}$, (k) 130.F.666, (l) 130.F.3$_{.5}$3$_{.5}$5$_{.0}$; forth row: (m) 130.F.3$_{.5}$5$_{.5}$3$_{.0}$, (n) 130.F.5$_{.5}$3$_{.5}$3$_{.0}$, (o) 140.F.666, (p) 140.F.4$_{.5}$4$_{.5}$3$_{.0}$)

By comparing the WPS of the submodels and the original models with same speed and uniform sleeper spacing, it can be concluded that application of non-uniform sleeper spacing results in increasing the energy concentration in high frequencies around 3kHz. This result is identical with the findings obtained in chapter 4 where non-uniform sleeper spacing was implemented. Despite of the prominent high-frequency vibration in 9 models, the 100.F.4$_{.5}$4$_{.5}$3$_{.0}$

and 120.F.$4_{.5}3_{.0}4_{.5}$ show the lowest energy concentrations compare to the other proposed submodels. On the other hand, the 130.F.$3_{.5}3_{.5}5_{.0}$, 130.F.$3_{.5}5_{.5}3_{.0}$ and 140.F.$4_{.5}4_{.5}3_{.0}$ shows the highest energy concentration at the high frequencies.

6.3 Decision the Optimum Combination

In order to select the optimum design, the objective functions are required to be defined. The impact force is highly regarded as the cause of degradation of the track and the low-frequency vibration affects the passenger comfort (Pradhan et al., 2017). Moreover, the wheel-rail interaction is considered as the cause of the noise radiation. Therefore, the decision on the choice of the most optimum design, is based on the impact force, low-frequency vibration as well as the high-frequency vibrations.

6.3.1 Variation Analysis - *w.r.t* original models

With the aim of choosing the optimum design, various optimization schemes are implemented in this research. Accordingly, the results are analyzed by determining the variation of the performance of the submodels compare to the models with identical speed and uniform sleeper spacing. This approach can illustrate the possibility of reduction of the impact force and vibration in each speed block. Besides, the performance of the submodels can be considered distinctly. Later, the submodels are divided into blocks with similar sleeper spacing and different speeds. Accordingly, the influence of the specific sleeper spacing on different speeds are evaluated and the most influential sleeper spacing arrangement is selected.

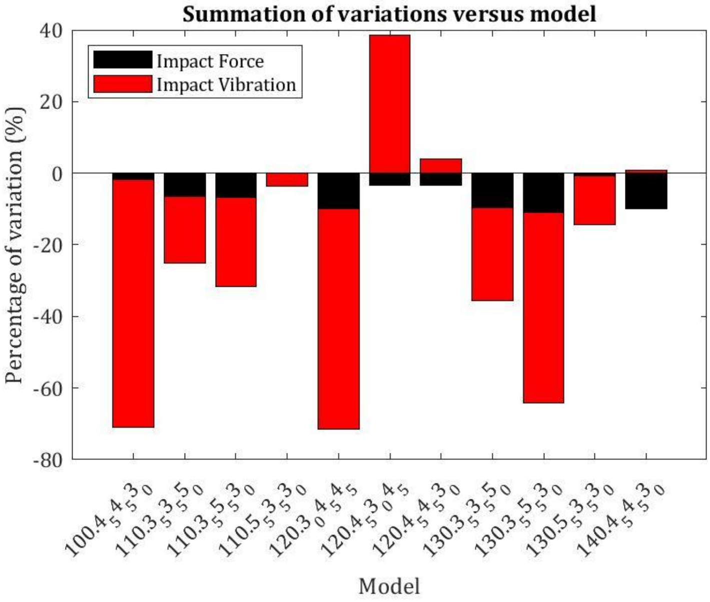

Figure 6-13 Summation of variation of outputs w.r.t original model – Performance block

The variations of the impact force and low-frequency vibrations with respect to the original models (100.F.666, 110.F.66, 120.F.666, 130.F.666 and 140.F.666) are shown in figure 6-13. In a general overview, the application of the non-uniform sleeper spacing results in significant reduction of the low-frequency vibration within all speed blocks. The submodels $100.F.4_{.5}4_{.5}3_{.0}$, $120.F.3_{.0}4_{.5}3_{.0}$ and $130.F.3_{.5}5_{.5}3_{.0}$ obtained the highest improvement in reduction of the low-frequency vibration whereas the $120.F.4_{.5}3_{.0}4_{.5}$ experienced an increase in the low-frequency vibration. The improvements in the reduction of the impact force can be seen in 9 submodels. The submodels $130.F.3_{.5}5_{.5}3_{.0}$, $140.F.4_{.5}4_{.5}3_{.0}$ and $130.F.3_{.5}3_{.5}5_{.0}$ experienced the highest reduction in the impact force respectively while the $110.F.5_{.5}3_{.5}3_{.0}$ and $130.F.5_{.5}3_{.5}3_{.0}$ did not experience any reduction of the impact force.

The variation of the impact force and low-frequency vibration in specific sleeper spacing blocks are illustrated in figure 6-14. The implementation of 1st, 2nd and 3rd sleeper spacing of 550, 350 and 300mm does not result in any improvement in the impact force. Besides, this arrangement of sleepers caused a small reduction of the low-frequency vibration when the speed of 110 and 130km/h is utilized. On the other hand, the implementation of the 350, 350 and 500mm and 350, 550 and 300mm for the 1st, 2nd and 3rd sleeper spacing resulted in significant reduction of both the impact force and impact vibration in the speeds of 110 and 130km/h. Although the sleeper spacing of 450, 450 and 300mm influenced the low-frequency vibration at the speed of 100km/h, it caused a minor increase of impact vibration at the speed of 120 and 140km/h. Besides, this formation of the sleepers resulted in improvement of low-frequency vibration at the speed of 100, 120 and 140km/h.

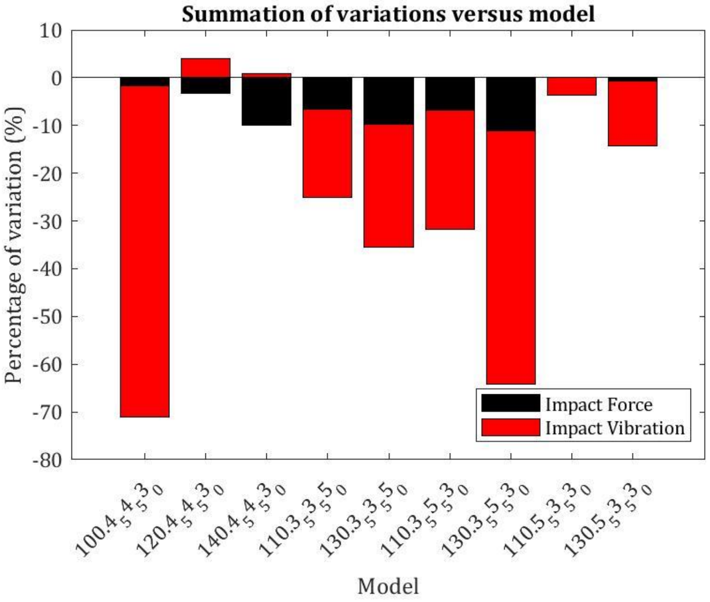

Figure 6-14 Summation of variation of outputs w.r.t original model – Sleeper spacing block

Overall, the $100.F.4_{.5}4_{.5}3_{.0}$ is the most optimized model in terms of reduction of the impact vibration while $130.F.3_{.5}5_{.5}3_{.0}$ showed the best improvement of the impact force. Besides, the implementation of the submodels $100.F.4_{.5}4_{.5}3_{.0}$ and $120.F.3_{.0}4_{.5}4_{.5}$ caused highest sum improvement of the impact force and low-frequency vibrations. In addition, although the application of non-uniform sleeper spacing is believed to result in incrementation of the vibration at high frequencies, the WPS in figure 6-10 shows that the implementation of non-uniform sleeper spacing in the submodels 100.F.$4_{.5}4_{.5}3_{.0}$ may not result in significant increment of the high-frequency vibrations. Therefore, the 100.F.$4_{.5}4_{.5}3_{.0}$ is nominated as the most optimized model in this research.

According to (Zong, 2013), the average life of the IRJs are is reported as 200 MGT with requirements of replacement in the period of 1-2 years. The failure of IRJ in UK costs £10 million in a two year period. Despite of the introduction of the new signaling system; ERTMS, the insulated rail joints are widely used nowadays. Therefore, the essence of reducing the impact force is considerably crucial to decrease the maintenance cost of the IRJs. Since there are repetitive impact forces exerted on the track due to the large number of train axles in the dense railway networks, small percentage of reduction in the impact force can increase the service life of the IRJs and reduce the maintenance cost subsequently.

6.3.2 Interaction Analysis - *hiplot*

The *hiplot* toolbox is a lightweight interactive visualization tool which helps users to understand the correlations and patterns in high-dimensional data. Accordingly, the *hiplot* is utilized to discover the relations between the factors; 1st, 2nd and 3rd sleeper spacing as well as the speed of the traffic and the outputs; impact force, low-frequency vibration. The results are shown in figure 6-15.

Since the degradation of the rail depends on the impact force and the passenger comfort and noise generation are influenced by the impact vibration, the performance of the proposed submodels can be investigated by considering the impact force and impact vibration distinctly. The application of the *hiplot* is believed to be an aid to focus on the objective functions separately.

According to figure 6-15, the minimum impact force is obtained for the 100.F.$4_{.5}4_{.5}3_{.0}$. The next submodels with lowest impact forces are the 130.F.$3_{.5}5_{.5}3_{.0}$ and 120.F.$4_{.5}3_{.0}4_{.5}$. The impact force obtained for these two submodels shows that implementation of non-uniform sleeper spacing can result in consistent impact force although the traffic speed is increased. The similar results can be observed when the impact forces between 1400 to 1420kN are considered. The employment of non-uniform sleeper spacing resulted in similar impact forces despite different speeds; 110, 120 and 130km/h are utilized.

On the other hand, the sleeper arrangement may increase the impact force significantly. Although the results in chapter 5 showed that lower traffic speed may result in lower impact force, the implementation of the 1st, 2nd and 3rd sleeper spacing of 550mm, 350mm and 300mm results in upsurge of the impact force in the submodel with the speed of 110km/h which is similar to when the speed of 140km/h is applied.

Based on figure 6-15, the lowest low-frequency vibration is found at the speed of 100km/h. The low-frequency vibration at the speed of 120km/h with the 1st, 2nd and 3rd sleeper spacing of 300mm, 450mm and 450mm resulted in the second lowest low-frequency vibration. Moreover, the submodel $140.F.4_{.5}4_{.5}3_{.0}$ has the highest low-frequency vibration which is identical to the results which are obtained in the impact force.

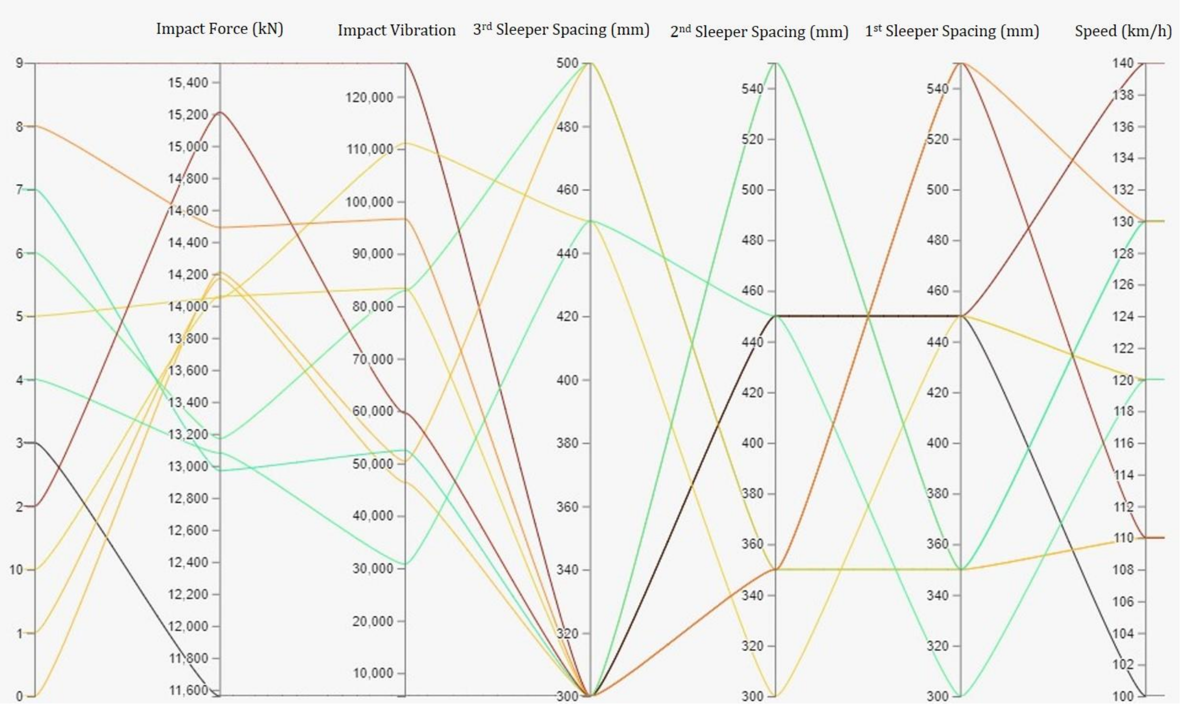

Figure 6-15 The correlation between the input factors and the outputs using hiplot toolbox

6.3.3 Data Analysis - Surface fitting

Data fitting is the process of fitting the models to acquired data by implementing various techniques which includes curve and surface fitting (*Curve fitting - Wikipedia*, n.d.). The surface fitting is the process of constructing the surface that has the best fit to a series of data points. The surface fitting involves regression, interpolation and smoothing methods. In the regression method, the estimation of the relationship between the output and input variables are performed using linear and nonlinear regression. In the interpolation method, the exact fit to the data as well as filling missed data are required while in smoothing method, a smooth function with reduced noise and approximate fit data are built. The regression analysis investigates the measures of uncertainty of the fitted data compared to the observed data.

The dedicated *data fitting* toolbox in MATLAB allows the users to import and perform different fitting techniques to produce the curve and surface models fitted to 2-D and 3-D data respectively (*Curve and Surface Fitting - MATLAB & Simulink*, n.d.). This toolbox implements various techniques to produce the fitting data such as regression, interpolation and smoothing. The working environment of the data fitting toolbox in MATLAB can be seen in figure 6-16.

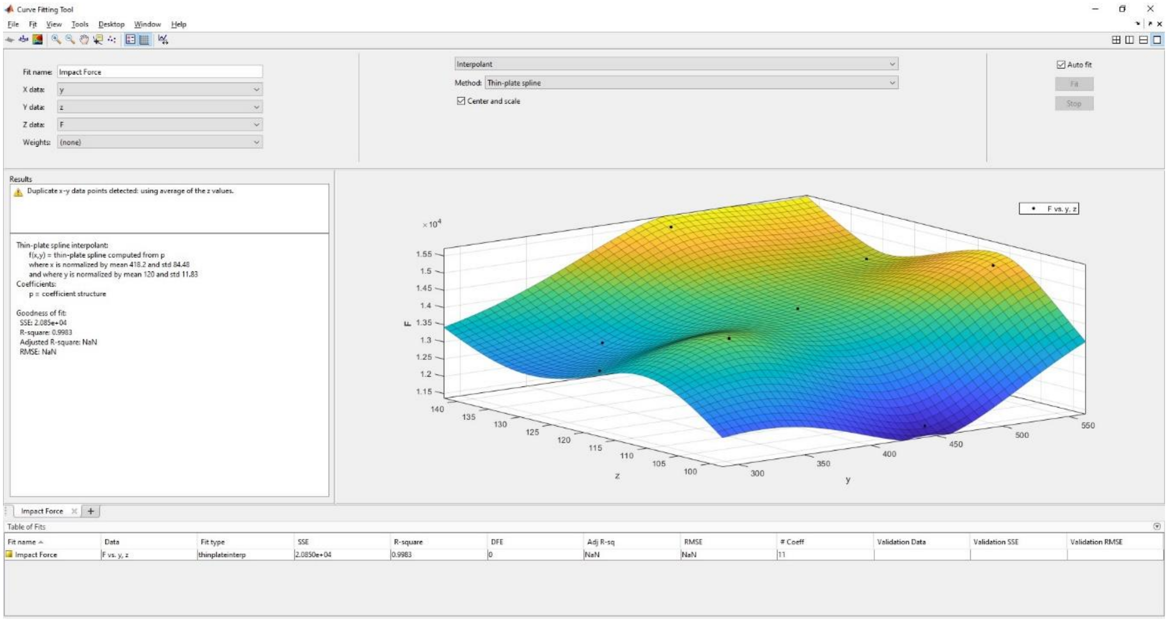

Fit name: Impact Force
X data: y
Y data: z
Z data: F
Weights: (none)

Interpolant
Method: Thin-plate spline
☑ Center and scale

☑ Auto fit

Results

```
Duplicate x-y data points detected: using average of the z values.
```

```
Thin-plate spline interpolant:
     f(x,y) = thin-plate spline computed from p
     where x is normalized by mean 418.2 and std 84.48
     and where y is normalized by mean 120 and std 11.83
Coefficients:
     p = coefficient structure

Goodness of fit:
  SSE: 2.085e+04
  R-square: 0.9983
  Adjusted R-square: NaN
  RMSE: NaN
```

Table of Fits

Fit name ▲	Data	Fit type	SSE	R-square	DFE	Adj R-sq	RMSE	# Coeff	Validation Data	Validation SSE	Validation RMSE
Impact Force	F vs. y, z	thinplateinterp	2.0850e+04	0.9983	0	NaN	NaN	11			

Figure 6-16 Working environment of the MATLAB data fitting toolbox

In this research, the interpolation fitting technique is utilized to obtain the surface model which includes speed as well as 1st, 2nd and 3rd sleeper spacing as the input variables and the impact force and low-frequency vibration as the output variables. The interpolation technique includes various sub-techniques which the thin-plate spline (TPS) is utilized based on its performance in producing the highest value of R-squared (R^2) in this research. Accordingly, the data related to the impact force and low-frequency vibration which corresponds to each input factor are extracted and the surface fitting with considering the speed against each sleeper spacing is constructed. The figure 6-17 (a) – (c) and figure 6-18 (a) – (c) illustrate the fit surfaces considering the impact force and low-frequency impact vibration.

According to figure 6-17 (a), there is a high magnitude of impact force within the boundaries where speed of 140km/h and 1st sleeper spacing of 550mm exist. Moreover, the fitted results show that the traffic speed of 110km/h results in high magnitude of the impact force by using the 1st sleeper spacing around 300 and 550mm. On the other hand, application of smaller 1st sleeper spacing in combination to the speed of 100km/h results in the lowest magnitude of the impact force. Besides, the combination of small 1st sleeper spacing and the speed of 130km/h resulted in noticeable low magnitude of the impact force.

According to figure 6-17 (b), similar results can be found for the impact force when speed and 2nd sleeper spacing are considered. Besides, the prominent magnitude of the impact force is occurred when the 2nd sleeper spacing of 450mm is implemented in combination with the speed of 140km/h. Based on figure 6-17 (c), the impact force is highly dependent on the traffic speed regardless of the distance of the 3rd sleeper spacing, Subsequently, the magnitude of the impact force is high when speed of 110 and 140 is utilized for all 3rd sleeper spacing.

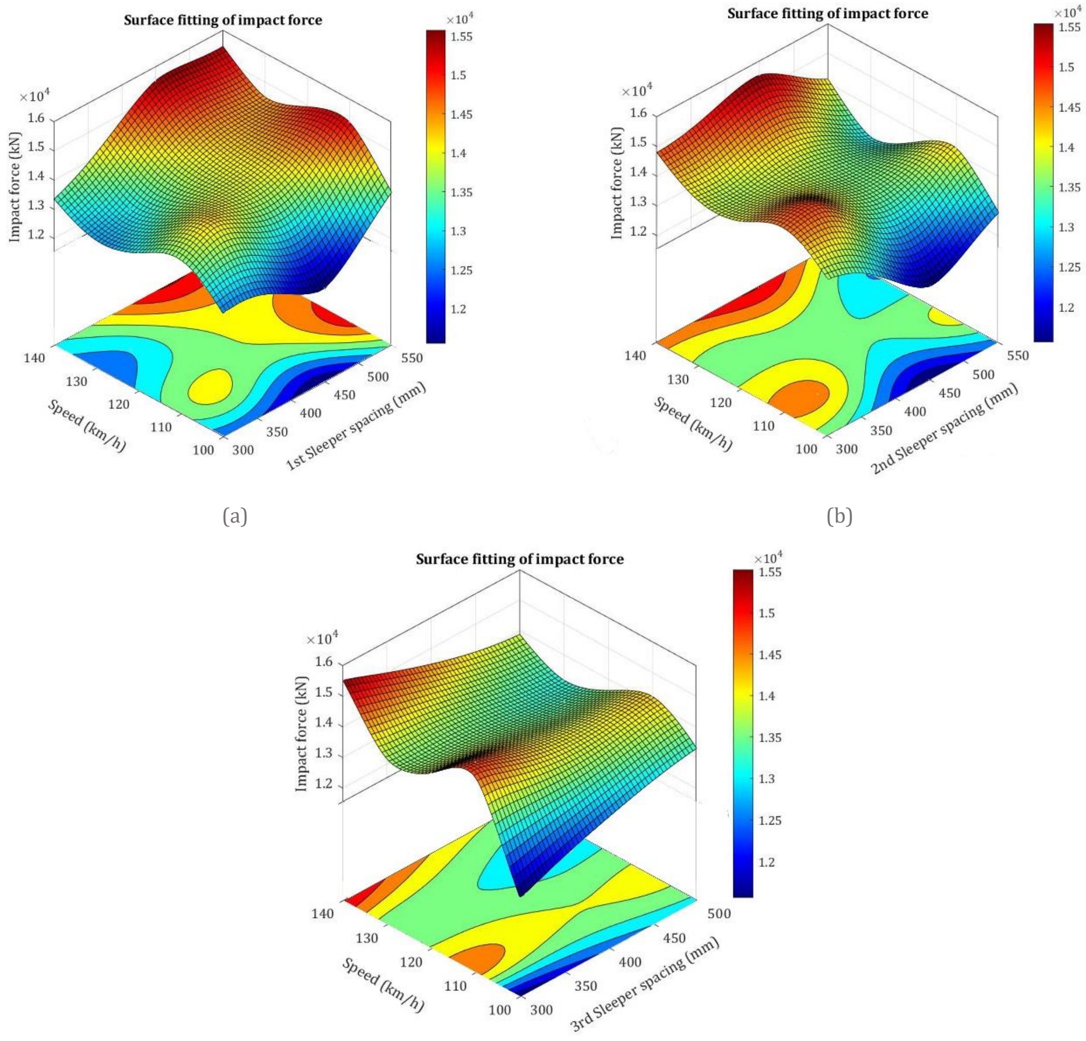

(a) (b)

(c)

Figure 6-17 Surface fitting of impact force (a) Speed vs 1st sleeper spacing; (b) Speed vs 2nd sleeper spacing; (c) Speed vs 3rd sleeper spacing

According to figure 6-18 (a), the simultaneous increment of the speed and 1st sleeper spacing cause the increasing of the magnitude of the low-frequency portion of the impact vibration. Accordingly, the combination of speed of 140km/h and 1st sleeper spacing of 550mm results in the highest magnitude of impact vibration while the value of 100km/h and 300mm for these two parameters results in the lowest value of the low-frequency vibration.

Based on figure 6-18 (b), the combination of the speed of 140km/h with the lower values of 2nd sleeper spacing resulted in high magnitude of the low-frequency impact vibration. On the other hand, the application of the slower traffic speed in combination with the wide range of 2nd sleeper spacing results in the low magnitude of the low-frequency vibration. According to figure 6-18 (c), the low-frequency vibration is highly dependent on the traffic speed regardless of the distance of the 3rd sleeper spacing, Subsequently, the high magnitude of the impact force can be seen when speed of 140 is utilized for all 3rd sleeper spacing while the low-frequency vibration experiences its lowest magnitude when the speed of 100km/h is used.

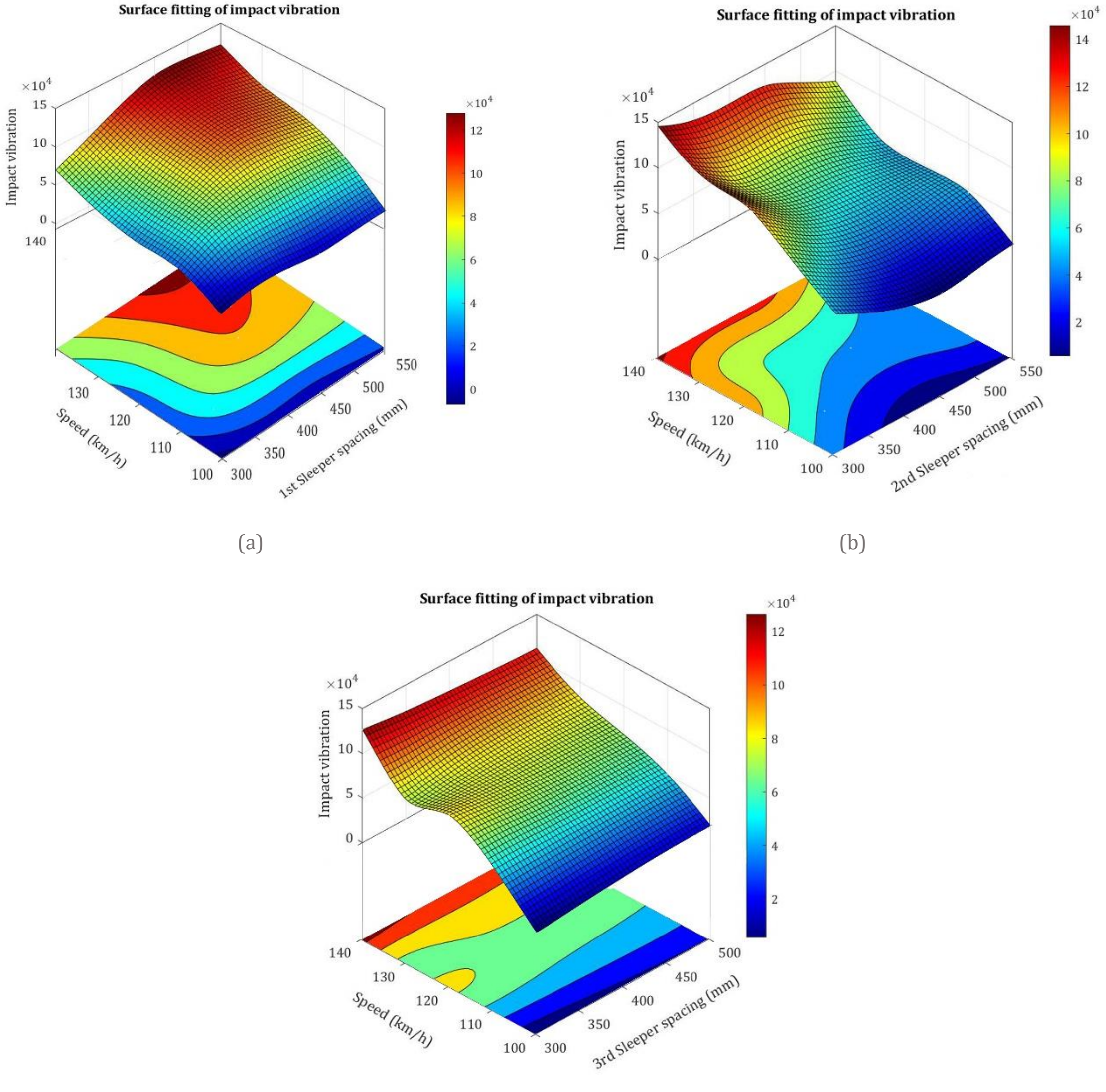

(a)

(b)

(c)

Figure 6-18 Surface fitting of impact vibration (a) Speed vs 1st sleeper spacing; (b) Speed vs 2nd sleeper spacing; (c) Speed vs 3rd sleeper spacing

6.3.4 Sensitivity Analysis

In order to evaluate the influence of the independent variables on the outcomes of a system, the sensitivity analysis can be performed. In other words, sensitivity analysis examines how sources of uncertainty contribute to the total uncertainty of a model (*Sensitivity Analysis Definition*, n.d.). The one-at-a-time (OAT) is one of the most common approaches utilized to examine the effects of the input factors on the output. The OAT involves varying one input and keep other factors unchanged at their nominal values (*Sensitivity analysis - Wikipedia*, n.d.). The changes in the output will be measured by repeating this step for all inputs. Therefore, this method is believed to provide the detailed information about the effectiveness of the output on each individual factor.

Accordingly, this research conducts the sensitivity analysis by considering the first impact force and the impact vibrations as the dependent variables of the model. In order to examine the contribution of the different factors to the outputs of the model, the sensitivity analysis is performed in two phases. First, the variation of the 1st and 2nd sleeper spacing in different speed blocks are considered individually. In the next phase, the effects of the speed in the 4 different sleeper spacing block is observed. The input factors and outputs are normally presented in scatter diagram and the correlations are obtained subsequently. However, due to the limited number of experiments proposed by DOE, such diagram cannot be plotted. Therefore, a linear regression analysis is performed to obtain the relationship between the inputs and outputs.

According to figure 6-19 (a), the first impact force is significantly sensitive to the distance of 1st sleeper spacing after the IRJ. Besides, it should be mentioned that by increasing the speed, the sensitivity of the impact force to the 1st sleeper spacing increases. On the other hand, the results show that the impact force is barely sensitive to the value of the 2nd sleeper spacing. Based on figure 6-19 (b), the 1st and 2nd sleeper spacing have noticeable influence on the impact vibration. It should be mentioned that impact vibration is highly sensitive to the distance of the 1st sleeper spacing when the speed of 120km/h is utilized for the traffic.

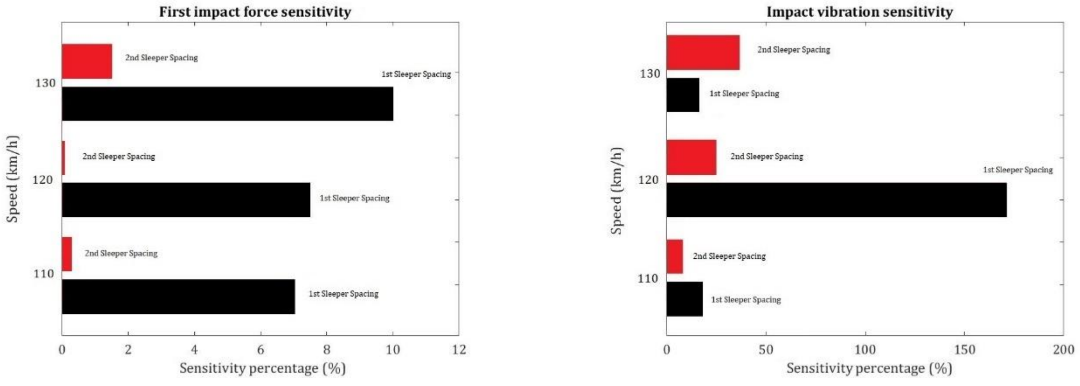

(a) (b)

Figure 6-19 Sensitivity analysis in speed block (a) First impact force; (b) Impact vibration

The sensitivity of the first impact force and impact vibrations to the variation of the speed are illustrated in figure 6-20 (a) and (b). According to figure 6-20 (a), the impact force is highly sensitive to the speed when the sleeper spacing of the 450, 450 and 300mm is implemented. The sensitivity of the impact force to the traffic speed is consistent for other arrangements of the sleepers. Based on figure 6-20 (b), the impact vibration is noticeably sensitive to the traffic speed.

The sleeper arrangement of $3_{.5}3_{.5}5_{.0}$ results the lowest sensitivity of impact vibration to the traffic speed.

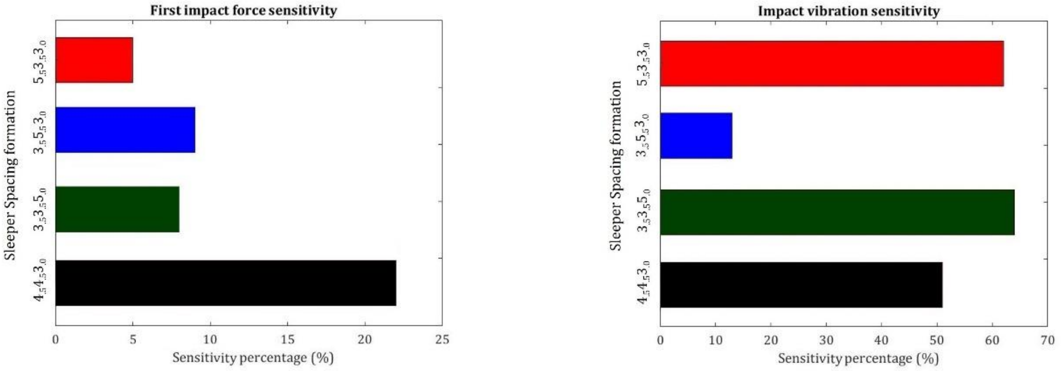

(a) (b)

Figure 6-20 Sensitivity analysis in sleeper spacing block (a) First impact force; (b) Impact vibration

6.4 Conclusion

The DOE technique was implemented in this chapter to acquire the best possible solution with regard to the impact force, low-frequency vibration and the energy concentration of vibration in high frequencies. According to (Oregui et al., 2015), the impact force is believed to be the cause of degradation of the track and low-frequency vibration is known to be the source of passenger comfort fluctuation based on (Pradhan et al., 2017). The high-frequency vibration is known to be the source of noise generation (Thompson et al., n.d.). Therefore, the goal of the optimization is to reduce the impact force, low-frequency impact vibration as well as the high-frequency vibrations.

Accordingly, the central composite design was utilized to determine the combination of the 3 factors which were defined as the speed, 1st sleeper spacing and 2nd sleeper spacing after the IRJ. In order to provide a feasible design, it was decided to remove the first sleeper after IRJ and replace it with the two concrete sleepers. Therefore, the 1st sleeper spacing is the distance between the timber and the 1st concrete sleeper after IRJ, the 2nd sleeper spacing is the distance between the 1st and 2nd concrete sleeper after IRJ and the 3rd sleeper spacing is defined as the 1200mm minus the summation of 1st and 2nd sleeper spacing.

The two optimization schemes that are utilized in this research includes selection of the optimum model based on the comparison between the performance of the submodels with two approaches. The comparison between all proposed submodels in the first approach demonstrated that the sleeper spacing of 350, 550 and 300mm together with the speed of 130km/h showed the best improvement in reducing the impact force while when the speed of 100km/h is combined with the sleeper spacing of 450, 450 and 300mm, the highest improvement in reduction of low-frequency vibration is achieved. In the second approach, the 1st, 2nd and 3rd sleeper spacing of 350, 350 and 500mm and 350, 550 and 300mm showed the best improvement among other sleeper spacing arrangements. The assessment on the performance of the submodels showed that application of non-uniform sleeper spacing can result in reduction of the impact force and vibration simultaneously. The $100.F.4_{.5}4_{.5}3_{.0}$ and $120.F.3_{.0}4_{.5}4_{.5}$ resulted in the highest reduction of the sum of impact force and impact vibration.

The WPS of the impact vibration showed that implementation of non-uniform sleeper spacing amplifies the high-frequency energy concentration. However, application of the model $100.F.4_{.5}4_{.5}3_{.0}$ showed the least increment of energy concentration in high frequencies compare to other proposed submodels. Therefore, the sleeper spacing of 450, 450 and 300mm with the traffic speed of 100km/h is nominated as the most optimized model in this research.

According to the results shown on the *hiplot*, it is concluded that the implementation of non-uniform sleeper spacing can provide the opportunity to increase the traffic speed although the impact force is not influenced. In order to propose a fitted surface model, the dedicated MATLAB toolbox, *cftool* was utilized. Accordingly, the boundaries where highest and lowest impact force and low-frequency vibration may be achieved is illustrated. The fitted surface model presented in this chapter is believed to provide the comprehensive relation between the combination of 1st, 2nd and 3rd sleeper spacing with the speed as the input factors and the impact force and low-frequency vibration as the outputs.

The sensitivity analysis performed in this chapter showed that the impact force is highly sensitive to the distance of the 1st sleeper spacing. The prominent sensitivity of the impact vibration to the 1st sleeper spacing when the speed of 120km/h is implemented was examined through the analysis. Moreover, the results showed a significant sensitivity of the impact force and vibration to the traffic speed.

7

Performance of the Optimized Models - Intercity and Sprinter

In this chapter, the performance of the proposed optimized models under different loading condition is assessed. Subsequently, two typical trains operating in the Dutch railway network; Intercity and Sprinter trains are utilized for this purpose. Furthermore, the effects of these two loading conditions on an optimized model obtained in chapter 6 is evaluated.

7.1 Overview of the Trains

In order to evaluate the performance of the proposed optimized models under different loading condition, the two particular trains that are operated on the Dutch railway network are selected. The sprinter trains are the electric multiple unit trains which are operated since 1975. There are 4 types of sprinter trains; SGM, SLT, FLIRT and SNG. These trains are considered as local trains with limited speed and car number. A sample of the sprinter trains is shown in figure 7-1.

Figure 7-1 A sprinter train in Utrecht

The intercity trains are the electric multiple unit (EMU) trains which are utilized to provide faster and long-distance service. There are five types of intercity trains; ICM, VIRM, DDZ, Intercityrijtuig and the TRAXX which is used for international services. These trains obtain more capacity for the passengers and therefore, they are heavier than the sprinter trains. A sample of intercity trains can be seen in figure 7-2.

Figure 7-2 An intercity train in Amsterdam

Based on the application of each train, the design weight and speeds are different. Accordingly, the axle load for the sprinter trains is around 18 tons whereas the intercity trains possess the axle load of 22 tons.

7.2 Overview on the Models

In order to assess the significance of the loading condition and evaluate the performance of the proposed optimized models under the different load conditions, the new submodels were created. Beside the optimized model proposed in chapter 7, the worst case submodel $120.4_{.5}3_{.0}4_{.5}$ was also used to check its performance under different load condition. Subsequently, the axle loads of the intercity and sprinter trains were used to modify the mass of the point elements (MASS21) that are the representative of the carbody and bogie. The carbody and the bogie are modeled with 8 and 4 point elements using MASS21. According to the model proposed by (Yang et al., 2018)the axle load is alienated to the carbody and the bogie with the proportion of 16.5:1. The division of the axle loads to the carbody and bogie can be found in the table 7-1.

Table 7-1 Division of the axle loads to the carbody and bogie

Trains	Axle Load	Load on each wheel	Carbody	Bogie
Intercity	22 tons	11 tons	10.350 tons	0.650 tons
Sprinter	18 tons	9 tons	8.5 tons	0.5 tons

Since the carbody is modeled using the 8 mass nodes, the mass of 1294kg and1063kg are assigned to each node for the intercity and sprinter trains respectively. Besides, the bogie contains 4 mass nodes, so the mass of each node is 162kg and 125kg for intercity and sprinter trains.

Similar to the previous chapters, the specific representation pattern is implemented to let the readers understand the properties of proposed submodels which is shown in figure 7-3.

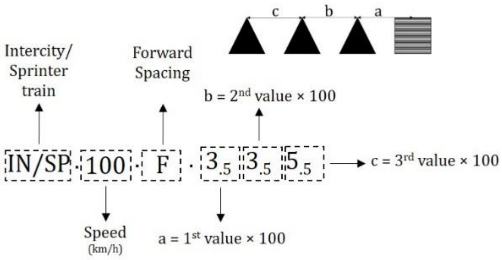

Figure 7-3 Representation pattern for submodels

The list of submodels can be found in table 7-2.

Table 7-2 List of the submodels

Model Nr.	Submodel	Model Nr.	Submodel
1	$IN.100.F.6_{.0}6_{.0}6_{.0}$	5	$SP.100.F.6_{.0}6_{.0}6_{.0}$
2	$IN.100.F.4_{.5}4_{.5}3_{.0}$	6	$SP.100.F.4_{.5}4_{.5}3_{.0}$
3	$IN.120.F.6_{.0}6_{.0}6_{.0}$	7	$SP.120.F.6_{.0}6_{.0}6_{.0}$
4	$IN.120.F.4_{.5}3_{.0}4_{.5}$	8	$SP.120.F.4_{.5}3_{.0}4_{.5}$

7.3 Results and Interpretation

7.3.1 Impact Force

The figures 7-4 (a) and (b) show the impact forces of the obtained optimized model from chapter 6 and the original model with the identical speed and uniform sleeper spacing of 600mm. The figure 7-4 (a) illustrate the results for intercity train while figure 7-4 (b) shows the obtained data for the sprinter train.

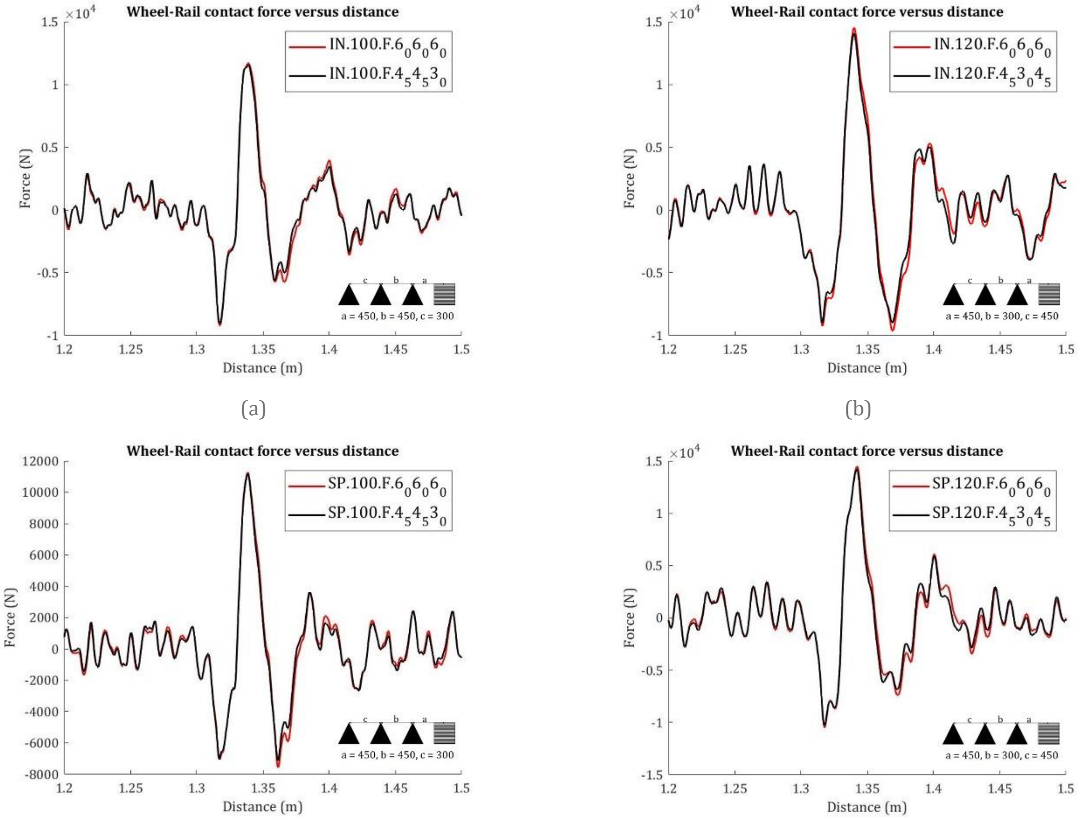

(a) (b)

(c) (d)

Figure 7-4 The impact force of proposed optimized models and original models (upper row: Intercity train; lower row: Sprinter train)

The amplitude and the variation of the impact force of the proposed optimized models with respect to the original models are shown i figure 7-5 (a) and (b). The original models are defined as the model with identical speed and mass but with different sleeper spacing pattern compare to the proposed optimized models which were obtained in the chapter 6.

According to figure 7-5 (a), the models with the assigned mass of the sprinter train have lower impact force compare to the intercity trains except the submodel SP.120.$4_{.5}3_{.0}4_{.5}$. Based on figure 7-5 (b) application of non-uniform sleeper spacing has higher effects on the impact force when the intercity train is considered. Subsequently, the comparison between figure (a) and (b) for the speed of 120km/h and sleeper spacing of 450, 300 and 450mm shows that higher reduction of the impact force in intercity trains result in lower impact force compare to the sprinter train with the same track and speed properties.

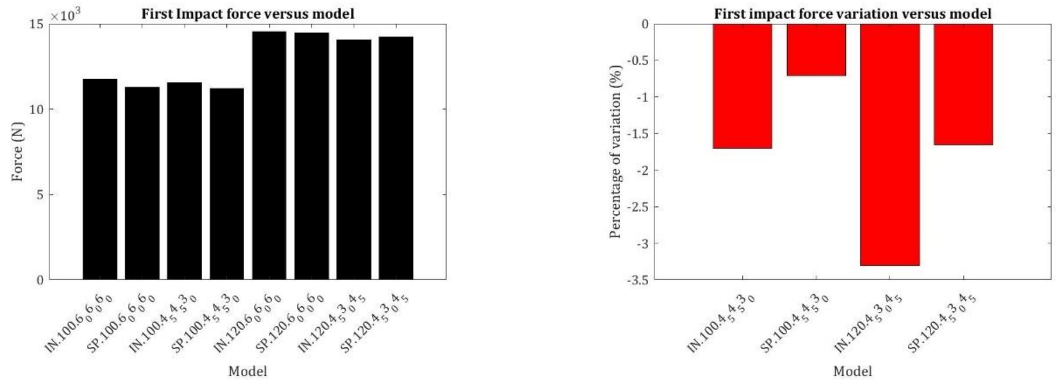

(a) (b)

Figure 7-5 First impact force - intercity and sprinter trains (a) First impact force value; (b) Variation w.r.t original model

7.3.2 Vertical Vibration

The magnitude of the impact vibration of each submodel and the original models with identical speed but uniform spacing of 600mm for 1st, 2nd and 3rd sleeper spacing is shown in figure 7-6 (a) and (b).

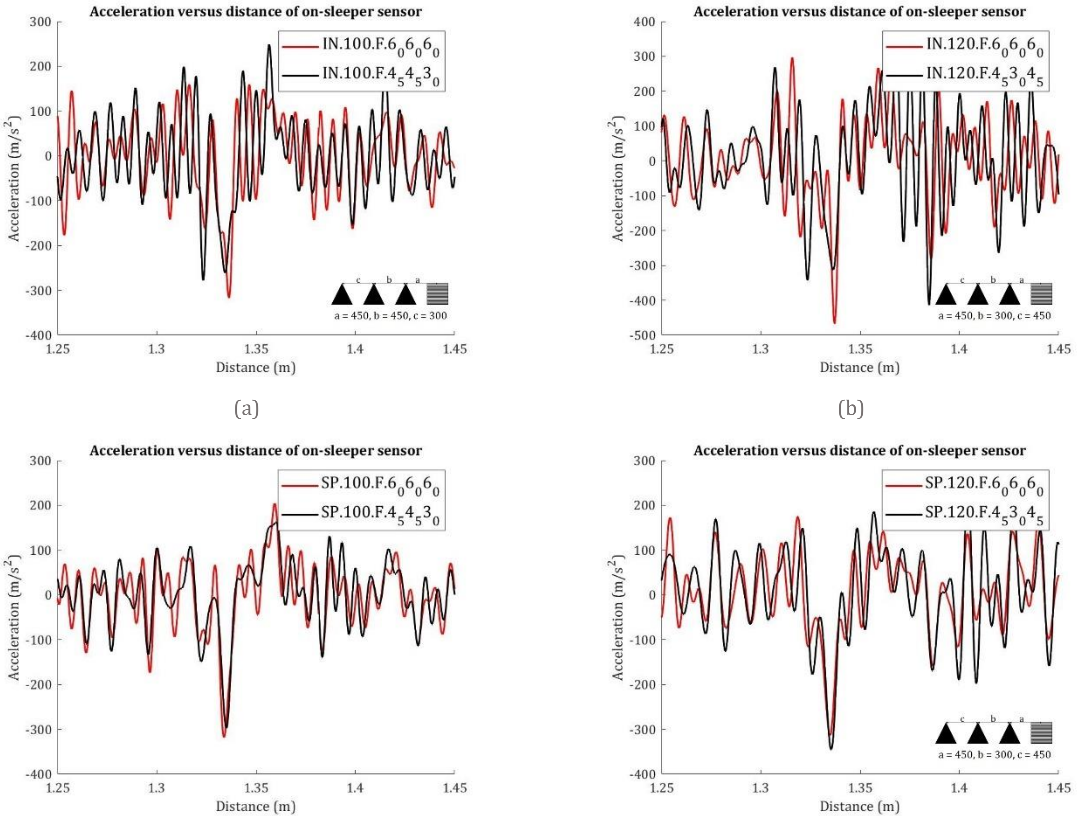

(a) (b)

(c) (d)

Figure 7-6 The impact vibration of proposed optimized models and original models (upper row: Intercity train; lower row: Sprinter train)

The amplitude and the variation of the low-frequency vibration of the proposed optimized models with respect to the original models are shown in figure 7-7 (a) and (b). According to figure 7-7 (a), the low-frequency vibration under the sprinter train is lower than when intercity train is implemented except in the submodel SP.100.$4_{.5}4_{.5}3_{.0}$. This is believed to be due to the prominent reduction of the impact vibration through the application of the non-uniform sleeper spacing. Moreover, figure 7-7 (b) demonstrate that the reduction of the impact vibration is more prominent in the case of intercity trains while the increment of the impact vibration is more when the sprinter train is utilized.

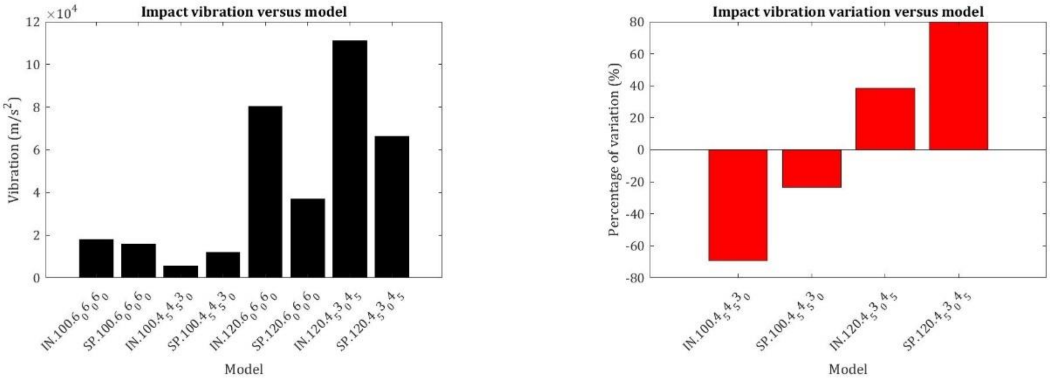

(a) (b)

Figure 7-7 Impact vibration - intercity and sprinter trains (a) Vibration value; (b) Variation w.r.t original model

The WPS of the impact vibration of submodels and the original model that is recorded using the part 18 can be seen in figure 7-8 (a) – (h). The unit of the color bar is m/s^2.

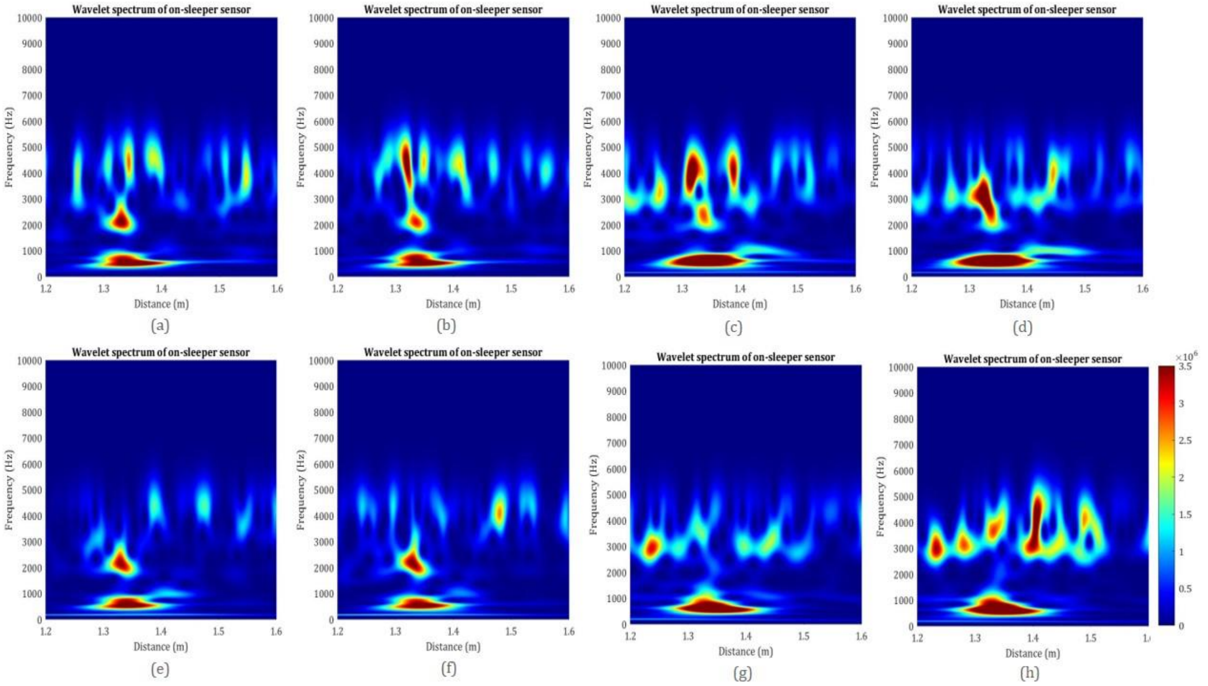

(a) (b) (c) (d)

(e) (f) (g) (h)

Figure 7-8 WPSs of the submodel and original impact vibration (first row: (a) IN.100.F.$6_{.0}6_{.0}6_{.0}$, (b) IN.100.F.$4_{.5}4_{.5}3_{.0}$, (c) IN.120.F.$6_{.0}6_{.0}6_{.0}$, (d) IN.120.F.$4_{.5}3_{.0}4_{.5}$; second row: (e) SP.100.F.$6_{.0}6_{.0}6_{.0}$, (f) SP.100.F.$4_{.5}4_{.5}3_{.0}$, (g) SP.120.F.$6_{.0}6_{.0}6_{.0}$, (h) SP.120.F.$4_{.5}3_{.0}4_{.5}$)

Based on the comparison between the impact vibration in figure 7-8 (a) and (e), the low and high frequency energy concentration is lower in the case of sprinter train. By comparing figure 7-8 (a) and (b), it can be deduced that the application of non-uniform sleeper spacing resulted in the increment of high-frequency energy concentration in intercity train while this parameter is not influenced in the SP.100.F.$4_{.5}4_{.5}3_{.0}$ where the sprinter train is considered. According to figure 7-8 (c) and (d), the prominent energy concentration in broadband between 4kHz to 5kHz is shifted to 2kHz – 3kHz when the non-uniform sleeper spacing of 450, 300 and 450mm is implemented under the intercity train that moves with the speed of 120km/h. The implementation of similar sleeper spacing resulted in significant increment of high-frequency vibration when sprinter train with the speed of 120km/h is considered.

The summation of variation of impact force and low-frequency vibration of the proposed submodels with respect to the original models with identical speed and mass is presented in figure 7-9.

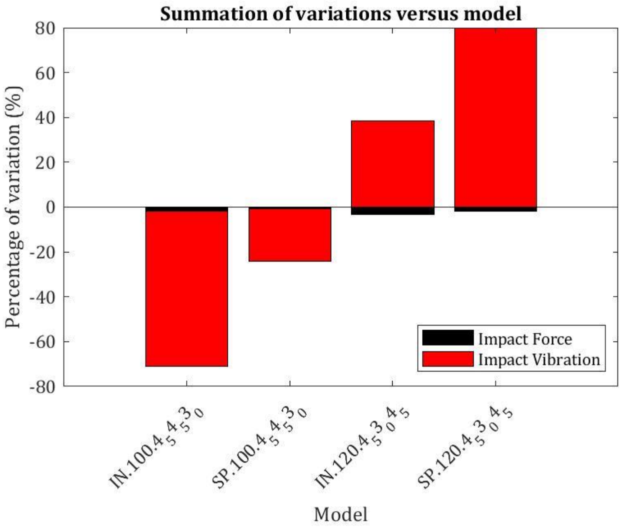

Figure 7-9 Summation of variation of outputs w.r.t original model

According to figure 7-9, a prominent improvement in reduction of the low-frequency vibrations can be clearly seen when the proposed optimized model in chapter 7 is implemented for intercity trains. Besides, a minor improvement in reduction of the impact force can be seen. Although plausible improvements in reduction of vibration can be seen in sprinter trains, the enhancement of the impact force is not noticed. On the other hand, it was shown that the 120.F.$4_{.5}3_{.0}4_{.5}$ introduced a significant increment of the impact vibration in the previous chapter. Similarly, an amplification of the low-frequency vibration can be clearly seen when intercity train is utilized. Moreover, this submodel perform worse when the sprinter train is implemented. Accordingly, an 80% increase of the amplitude of the low-frequency vibrations can be seen.

7.4 Conclusion

The two typical trains that are operated on the Dutch railway network are utilized to assess the performance of the proposed optimized model in chapter 7 under different loading conditions. Accordingly, the intercity and sprinter trains are utilized for this purpose. Moreover, the worst model which introduced an ultimate increment of the low-frequency vibration in the previous chapter was used to assess its performance under intercity and sprinter trains.

As a conclusion, the application of proposed optimized model resulted in reduction of the impact force and impact vibration when intercity train is considered. This reduction is more prominent when the comparison with the sprinter train is conducted. Although sprinter train possess lower axle loads, the implementation of worst model under both loading conditions showed that the impact vibration experienced a higher amplification when this type of train is considered.

Similarly, the comparison between the WPS of the impact vibration shows that implementation of the worst scenario (120.F.$4_{.5}3_{.0}4_{.5}$) resulted in prominent high-frequency energy concentration. On the other hand, the application of non-uniform sleeper spacing in the optimized model resulted in identical high-frequency vibrations compare to the original model with uniform sleeper spacing when the sprinter train is considered. Whereas, the broadband of the high-frequency vibration is migrated to a lower value when intercity train is applied.

8

Conclusions and Recommendations

In the final chapter, the conclusions and findings in this research is presented. The recommendations for further researches are also described in this chapter.

8.1 Conclusion

This M.Sc. thesis performed an explicit finite element analysis to evaluate the performance of the railway track considering the variation of sleeper spacing as well as different traffic speed and load conditions. A typical statistical approach, Design of Experiment (DOE) was implemented to determine the most optimized combination of sleeper spacing and traffic speed which enhances the performance of the railway track by reducing the impact force as well as the low and high-frequency vibrations.

The application of non-uniform sleeper spacing after the IRJ resulted in the reductions of the impact force as well as the low-frequency vibration. The reduction of vibration in dominant frequencies of 600Hz and 1kHz is in line with prior researches where the reduction of the resonance of the rail resonance and pinned-pinned resonance of the track were observed. However, the non-uniform sleeper spacing increases the high-frequency impact vibration from 3 to 5kHz. The vibration in low frequency is reduced by the reduction of the wheel-rail impact force excitation and the amplitude of the low-frequency track resonance. While the high-frequency vibration is believed to be increased by the amplitude of the high-frequency track resonances.

This study shows that, in general, increasing the traffic speed results in increase of the impact force as well as the impact vibration. Accordingly, the significant increment of the amplitude of the high-frequency impact force excitations resulted in a noticeable upsurge of the response in the broadband between 3kHz and 5kHz. Besides, the less significant incrementation of the response relative to the low-frequency excitation was observed.

In order to reduce the maintenance costs and noise generation as well as to improve the passenger comfort, impact force and vibration of the track in the low and high frequencies are desired to be minimized respectively. In this research, a typical statistical approach was utilized to obtain the most optimized train-track model which provides the optimal performance within the mentioned criteria. Although the proposed models resulted in incrementation of the high-frequency vibrations, prominent improvements in the reduction of impact force and low-frequency vibrations were observed. Accordingly, it was recommended to apply a distinct approach in the selection of the optimized model considering the three criteria: impact force, low-frequency vibration and high-frequency vibration.

The impact force and low-frequency vibrations showed a noticeable sensitivity to the distance of the 1st sleeper spacing after IRJ while the prominent dependency of the impact vibration on traffic speed was observed. The implementation of the proposed optimized model under two load condition: intercity and sprinter trains, showed possible improvements in both conditions. Besides, the application of such model resulted in more prominent improvements when the heavier train, i.e. intercity train is used.

8.2 Recommendation

The finite element model utilized in this research can be developed to provide more realistic results related to the wheel-rail dynamic interaction. Accordingly, the utilization of the nominal geometries of insulation layer, end post and bolts as well as a realistic representation of the rail pads may result in an improved fit between the model and the measurements.

In addition, due to the variation of different parameters in this research, the calibration and validation of the model against the measurements in each stage may introduce a more reliable train-track model.

Evaluation of the contact force between the joint bar and rail may provide a better insight on degradation of each component individually. Besides, the evaluation of the stress distribution of various insulation materials may provide the opportunity to improve the life span of the insulation materials.

The explicit FEM solver utilized in this research requires notable computational time to analyze the wheel-rail dynamic interaction. The computational time is expected to be reduced by reducing the excessive conditional statements in the explicit FE program.

The measures to reduce the high-frequency vibration caused by the wheel-rail interaction can be investigated in future researches.

References

ANSYS Mechanical APDL Element Reference. (n.d.).

Augmented Lagrangian Methods. (n.d.). Retrieved May 12, 2020, from https://neos-guide.org/content/augmented-lagrangian-methods

Boeing Frontiers Online. (n.d.). Retrieved May 12, 2020, from https://www.boeing.com/news/frontiers/archive/2003/october/i_tt.html

Boyd, P., Mandal, N. K., Mandal, N., Bandula, T., Zong, N., & Dhanasekar, M. (2012). *Experimental investigation into the failure behaviour of insulated rail joints*. https://www.researchgate.net/publication/259240841

Cai, W., Wen, Z., Jin, X., & Zhai, W. (2007). Dynamic stress analysis of rail joint with height difference defect using finite element method. *Engineering Failure Analysis*, *14*(8), 1488–1499. https://doi.org/https://doi.org/10.1016/j.engfailanal.2007.01.007

Chen, Y. C., & Kuang, J. H. (n.d.). *Contact stress variations near the insulated rail joints*.

COMBI165. (n.d.). Retrieved March 28, 2020, from http://www.mm.bme.hu/~gyebro/files/ans_help_v182/ans_elem/Hlp_E_COMBI165.html

Curve and Surface Fitting - MATLAB & Simulink. (n.d.). Retrieved May 20, 2020, from https://www.mathworks.com/help/curvefit/command-line-curve-and-surface-fitting.html

Davis, D. D., Akhtar, M., & Kohake, E. (n.d.). *Effects of heavy axle loads on bonded insulated joint performance*.

de man, A. P. (2002). *A survey of dynamic railway track properties and their quality*.

Dean, J. (n.d.). *Introduction to the Finite Element Method (FEM)*.

Design of Experiments - A Primer. (n.d.). Retrieved May 22, 2020, from https://www.isixsigma.com/tools-templates/design-of-experiments-doe/design-experiments-%E2%90%93-primer/

Elshukri, F. A. (2016). *An Experimental Investigation and Improvement of Insulated Rail Joints (IRJs) End Post Performance*.

Experimental Design (DOE) economically maximizes information. (n.d.). Retrieved May 12, 2020, from https://www.itl.nist.gov/div898/handbook/pri/section1/pri11.htm

Feng, H. (2011). *3D-models of Railway Track for Dynamic Analysis*.

Finite Element Method - Introduction. (n.d.). Retrieved May 22, 2020, from https://www.doitpoms.ac.uk/tlplib/fem/intro.php

Finite element method - Wikipedia. (n.d.). Retrieved May 12, 2020, from https://en.wikipedia.org/wiki/Finite_element_method

Funiculars, Funiculaires, Funicolare, DFB (Michel Azéma) reszug01. (n.d.). Retrieved March 6, 2020, from http://www.funimag.com/funimag10/RESZUG01.HTM

Gallou, M., Temple, B., Hardwick, C., Frost, M., & El-Hamalawi, A. (2018). Potential for external reinforcement of insulated rail joints. *Proceedings of the Institution of Mechanical Engineers, Part F: Journal of Rail and Rapid Transit*, *232*(3), 697–708. https://doi.org/10.1177/0954409716684278

Grassie, S. L., Gregory, R. W., Harrison, D., & Johnson, K. L. (1982). The Dynamic Response of Railway Track to High Frequency Vertical Excitation. *Journal of Mechanical Engineering Science*, *24*(2), 77–90. https://doi.org/10.1243/JMES_JOUR_1982_024_016_02

Hither Green rail crash - Wikipedia. (n.d.). Retrieved March 9, 2020, from https://en.wikipedia.org/wiki/Hither_Green_rail_crash

Implicit vs Explicit FEM. (n.d.). Retrieved May 12, 2020, from https://www.simscale.com/blog/2019/01/implicit-vs-explicit-fem/

Initial condition - Wikipedia. (n.d.). Retrieved April 9, 2020, from https://en.wikipedia.org/wiki/Initial_condition

Kabo, E., Nielsen, J. C. O., & Ekberg, A. (2006). Prediction of dynamic train-track interaction and subsequent material deterioration in the presence of insulated rail joints. *Vehicle System Dynamics*, *44*(SUPPL. 1), 718–729. https://doi.org/10.1080/00423110600885715

Koro, K., Abe, K., Ishida, M., & Suzuki, T. (2004). Timoshenko beam finite element for vehicle—track vibration analysis and its application to jointed railway track. *Proceedings of the Institution of Mechanical Engineers, Part F: Journal of Rail and Rapid Transit*, *218*(2), 159–172. https://doi.org/10.1243/0954409041319687

Kumar Mandal, N., & Peach, B. (2010). An Engineering Analysis of Insulated Rail Joints: A General Perspective. *International Journal of Engineering Science and Technology*, *2*(8), 3964–3988. https://www.researchgate.net/publication/50346113

Mandal, N. K. (2016). Finite element analysis of the mechanical behaviour of insulated rail joints due to impact loadings. *Proceedings of the Institution of Mechanical Engineers, Part F: Journal of Rail and Rapid Transit*, *230*(3), 759–773. https://doi.org/10.1177/0954409714561708

Molodova, M., Li, Z., Núñez, A., & Dollevoet, R. (2014). Validation of a finite element model for axle box acceleration at squats in the high frequency range. *Computers and Structures*, *141*, 84–93. https://doi.org/10.1016/j.compstruc.2014.05.005

Molodova, M., Oregui, M., Núñez, A., Li, Z., & Dollevoet, R. (2016). Health condition monitoring of insulated joints based on axle box acceleration measurements. *Engineering Structures*, *123*, 225–235. https://doi.org/10.1016/j.engstruct.2016.05.018

Müller, A. L. H., de Oliveira, J. A., Prestes, O. D., Adaime, M. B., & Zanella, R. (2019). Design of experiments and method development. In *Solid-Phase Extraction* (pp. 589–608). Elsevier. https://doi.org/10.1016/B978-0-12-816906-3.00022-4

Nicoli, E., Dillard, D. A., Campbell, J., Dillard, J., Turner, M. A., Davis, D. D., & Akhtar, M. (n.d.). *Characterizing and Improving Insulated Joints Performance*.

Oregui, M., Molodova, M., Núñez, A., Dollevoet, R., & Li, Z. (2015). Experimental Investigation Into the Condition of Insulated Rail Joints by Impact Excitation. *Experimental Mechanics*, *55*(9), 1597–1612. https://doi.org/10.1007/s11340-015-0048-7

Pang, T., & Dhanasekar, M. (n.d.). *Dynamic finite element analysis of the wheel-rail interaction adjacent to the insulated rail joints*.

Papaioannou, I. (2018). *Experimental and numerical study on the optimisation of insulated rail joint dynamic behaviour*. http://repository.tudelft.nl/.

Pioltello train derailment - Wikipedia. (n.d.). Retrieved March 9, 2020, from https://en.wikipedia.org/wiki/Pioltello_train_derailment

Pradhan, S., Samantaray, A. K., & Bhattacharyya, R. (2017). Evaluation of ride comfort in a railway passenger vehicle with integrated vehicle and human body bond graph model. *ASME International Mechanical Engineering Congress and Exposition, Proceedings (IMECE)*, *12*. https://doi.org/10.1115/IMECE2017-71288

Rail transport - Wikipedia. (n.d.). Retrieved March 6, 2020, from https://en.wikipedia.org/wiki/Rail_transport

Rail transport in the Netherlands - Wikipedia. (n.d.). Retrieved March 7, 2020, from https://en.wikipedia.org/wiki/Rail_transport_in_the_Netherlands

Railway Map The Netherlands - Wikipedia. (n.d.). Retrieved March 7, 2020, from https://en.wikipedia.org/wiki/File:Railway_Map_The_Netherlands.svg

Review of Trackside Monitoring Solutions. (n.d.). Retrieved March 7, 2020, from https://www.mdpi.com/1424-8220/15/8/20115/htm

Road-way vs. railway safety- Wikipedia. (n.d.). Retrieved March 6, 2020, from https://en.wikipedia.org/wiki/File:Road-way_vs._railway_safety.png

Sadri, M., & Steenbergen, M. (2018). Effects of railway track design on the expected degradation: Parametric study on energy dissipation. *Journal of Sound and Vibration*, *419*, 281–301. https://doi.org/10.1016/j.jsv.2018.01.029

Sensitivity Analysis Definition. (n.d.). Retrieved May 13, 2020, from https://www.investopedia.com/terms/s/sensitivityanalysis.asp

Sheikh, W., Awachat, P. N., & Sheikh, S. M. (2014). Failure and Stresses Develop in Insulated Rail Joints: General Perspective. *International Journal of Innovative Science and Modern Engineering*, *2*(9).

Spiroiu, M. A. (2016). Wheel-rail dynamic forces induced by random vertical track irregularities. *IOP Conference Series: Materials Science and Engineering*, *147*(1). https://doi.org/10.1088/1757-899X/147/1/012117

Suzuki, T., Ishida, M., Abe, K., & Koro, K. (n.d.). *Measurement on Dynamic Behaviour of Track near Rail Joints and Prediction of Track Settlement*.

Thompson, D. (2009). Track Vibration. In *Railway Noise and Vibration* (pp. 29–95). Elsevier. https://doi.org/10.1016/b978-0-08-045147-3.00003-7

Thompson, D., Wu, T., & Armstrong, T. (n.d.). *WHEEL/RAIL ROLLING NOISE-THE EFFECTS OF NON-LINEARITIES IN THE CONTACT ZONE*.

Track circuit - Wikiwand. (n.d.). Retrieved March 7, 2020, from https://www.wikiwand.com/en/Track_circuit

Types of Rail Joints. (n.d.). Retrieved March 8, 2020, from http://www.eng.dieselloc.ru/railway-engineering/types-of-rail-joints.html

Wang, K. Y., Liu, P. F., Zhai, W. M., Huang, C., Chen, Z. G., & Gao, J. M. (2014). Wheel/rail dynamic interaction due to excitation of rail corrugation in high-speed railway. *Science China Technological Sciences*, *58*(2), 226–235. https://doi.org/10.1007/s11431-014-5633-y

Wen, Z., Jin, X., & Jiang, Y. (2005). Elastic-Plastic Finite Element Analysis of Nonsteady State Partial Slip Wheel-Rail Rolling Contact. *Journal of Tribology-Transactions of The Asme - J TRIBOL-TRANS ASME*, *127*. https://doi.org/10.1115/1.2033898

What are the differences between implicit and explicit? (n.d.). Retrieved May 12, 2020, from https://www.dynasupport.com/faq/general/what-are-the-differences-between-implicit-and-explicit

World railway network - Wikipedia. (n.d.). Retrieved March 6, 2020, from https://en.wikipedia.org/wiki/File:World_railway_network.png

Xin, T., Wang, P., & Ding, Y. (2019). Effect of Long-Wavelength Track Irregularities on Vehicle Dynamic Responses. *Shock and Vibration*, *2019*, 4178065. https://doi.org/10.1155/2019/4178065

Yang, Z. (2018). Numerical Modelling of Wheel-rail Dynamic Interactions with an Explicit Finite Element Method. In *Citation (APA) Yang, Z.* https://doi.org/10.4233/uuid:8acb9b48-bf77-45b2-a0d6-1cf6658f749e

Yang, Z., Boogaard, A., Chen, R., Dollevoet, R., & Li, Z. (2018). Numerical and experimental study of wheel-rail impact vibration and noise generated at an insulated rail joint. *International Journal of Impact Engineering*, *113*, 29–39. https://doi.org/10.1016/j.ijimpeng.2017.11.008

Zakeri, J. A., & Xia, H. (2008). Sensitivity analysis of track parameters on train-track dynamic interaction. *Journal of Mechanical Science and Technology*, *22*(7), 1299–1304. https://doi.org/10.1007/s12206-008-0316-x

Zong, N. (2013). *Development of optimal designs of insulated rail joints*.